

ORBITAL EVOLUTION, ACTIVITY, AND MASS LOSS OF COMET C/1995 O1 (HALE-BOPP).
I. CLOSE ENCOUNTER WITH JUPITER IN THIRD MILLENNIUM BCE AND EFFECTS
OF OUTGASSING ON THE COMET'S MOTION AND PHYSICAL PROPERTIES

ZDENEK SEKANINA¹ & RAINER KRACHT²

¹Jet Propulsion Laboratory, California Institute of Technology, 4800 Oak Grove Drive, Pasadena, CA 91109, U.S.A.

²Ostlandring 53, D-25335 Elmshorn, Schleswig-Holstein, Germany

Version March 6, 2017

ABSTRACT

This comprehensive study of comet C/1995 O1 focuses first on investigating its orbital motion over a period of 17.6 yr (1993–2010). The comet is suggested to have approached Jupiter to 0.005 AU on –2251 November 7, in general conformity with Marsden's (1999) proposal of a Jovian encounter nearly 4300 yr ago. The variations of sizable nongravitational effects with heliocentric distance correlate with the evolution of outgassing, asymmetric relative to perihelion. The future orbital period will shorten to ~1000 yr because of orbital-cascade resonance effects. We find that the sublimation curves of parent molecules are fitted with the type of a law used for the nongravitational acceleration, determine their orbit-integrated mass loss, and conclude that the share of water ice was at most 57%, and possibly less than 50%, of the total outgassed mass. Even though organic parent molecules (many still unidentified) had very low abundances relative to water individually, their high molar mass and sheer number made them, summarily, important potential mass contributors to the total production of gas. The mass loss of dust per orbit exceeded that of water ice by a factor of ~12, a dust loading high enough to imply a major role for heavy organic molecules of low volatility in accelerating the minuscule dust particles in the expanding halos to terminal velocities as high as 0.7 km s⁻¹. In Part II, the comet's nucleus will be modeled as a compact cluster of massive fragments to conform to the integrated nongravitational effect.

Subject headings: comets: individual (C/1995 O1) — methods: data analysis

1. INTRODUCTION: MAKING CASE FOR A CLOSE
ENCOUNTER WITH JUPITER

The celebrated comet C/1995 O1 (Hale-Bopp) was exceptional in a number of ways, one of which was its enormous intrinsic brightness. This trait rendered it possible to discover and observe the comet at very large heliocentric distance and to collect astrometric observations over a long period of time. Discovered visually on 1995 July 23, more than 600 days before perihelion, as an object of mag 10.5–10.8 (Hale & Bopp 1995), the comet was subsequently recognized at mag 18 on a plate taken on 1993 April 27 with the 124-cm UK Schmidt telescope of the Siding Spring Observatory near Coonabarabran, N.S.W., Australia (McNaught 1995), 3.9 yr before perihelion and 13.0 AU from the Sun. With the latest astrometrically measured images from 2010 December 4 (when 30.7 AU from the Sun!), taken with the 220-cm f/8.0 Ritchey-Chrétien reflector of the European Southern Observatory's Station at La Silla, Chile (Sarneczky et al. 2011), the observed orbital arc covers a period of 17.6 yr, with 13.7 yr of post-perihelion astrometry — an unprecedented feat for a single-apparition comet.

No less astonishing is the orbital history of the comet (Marsden 1999). Soon after its discovery, the orbit could substantially be improved thanks to the Siding Spring pre-discovery observation. Although Marsden eventually determined that the near-perihelion osculating orbital period equalled about 2530 yr, he noticed that this was due in part to the perturbations by Jupiter during the comet's approach to within 0.8 AU of the planet about

one year before the 1997 perihelion and that the orbit had originally been more elongated, with a period of slightly longer than 4200 yr. Obviously, the object did not arrive from the Oort Cloud; its previous perihelion passage had occurred in the course of the 23rd century BCE.

As described by Marsden, this was only a minor part of the story. Because the comet's ascending node places it practically on Jupiter's orbit, extremely close encounters with the planet are possible, and Marsden (1999) argued that this was precisely what happened 42 centuries ago on the comet's approach to perihelion. He even ventured to propose that the comet had been captured by Jupiter's gravity from its original Oort-Cloud-type, highly elongated orbit.

In his investigation, Marsden (1999) was handicapped by a relatively short interval of time that the comet's observations then spanned. The last observation he employed was dated 1998 February 8, so that the observed orbital arc was only 4.8 yr long, not much more than a quarter of the interval of time available nowadays.

The fascinating problem of the long-term orbital evolution of C/1995 O1 and the related issues warrant a new investigation, given in particular that the much greater span of astrometric observations currently available allows us to conduct a considerably more profound examination of the orbital scenario and its potential implications than it was possible a dozen or more years ago [for some later efforts similar to Marsden's (1999), see, e.g., Szutowicz et al. (2002) or Królikowska (2004)]. We further propose to confront our approach and results with evidence from the comet's physical observations made in the course of the 1997 apparition and to draw conclusions from this data interaction.

2. DATA, TOOLS, AND METHOD OF APPROACH

We began by collecting 3581 astrometric observations of comet C/1995 O1 from the database maintained by the *Minor Planet Center*.¹ This is a complete list of the comet’s currently available astrometric data in equinox J2000. Besides the single pre-discovery observation in 1993 (McNaught 1995), the data set contains 830 observations from the year 1995, 1458 from 1996, 653 from 1997, 295 from 1998, 198 from 1999, 50 from 2000, 51 from 2001, 9 from 2002, 14 from 2003, 14 from 2005 (of which 6 from January–February and 8 from July–August), 5 observations from 2007 October, and 3 from 2010 December 4.²

The primary objective of the first phase of our orbit-determination effort was to subject the collected set of astrometric observations to tests in order to extract a subset of high-accuracy observations. To ensure that this has indeed been achieved requires an introduction of a cutoff or threshold of choice for removing from the collection all individual observations whose (observed minus computed) residuals in right ascension, $(O-C)_{\text{RA}}$, or declination, $(O-C)_{\text{Decl}}$, exceed the limit. In practice, the task is made difficult by the fact that a residual exceeding the limit does so for one of two fundamentally different reasons: either because the astrometric position is of poor quality or because the comet’s motion is modeled inadequately. The aim of the procedure is to reject the data points with large residuals that are of the first category but not of the second category; to discriminate between the two categories requires an incorporation of an efficient filter. Typically, the category into which an observation with a large residual belongs is revealed by comparing, with one another, observations over a limited orbital arc: if all or most of them exhibit systematic residuals, the problem is in the comet’s modeled motion; if one or a few stand out in reference to the majority, it is the poor quality of the individual observations. Obviously, this filter fails when there is only one or a very few observations available widely scattered over a long orbital arc (Section 4).

Since we did not define what we meant by inadequate modeling of the comet’s motion at the start of the orbit-determination process, we used two tools to filter out the observations of poor quality and at the same time to ensure that no observation of required accuracy was removed. One tool was a stepwise approach, beginning with a cutoff at $10''$ (Section 3) and tightening it up; the other tool was to divide the whole observed orbital arc into a number of segments of approximately equal and short enough length, fitting an osculating gravitational solution through each of the segments.

In addition, throughout this work we consistently applied a self-sustaining test of cutoff enforcement. When a particular cutoff was introduced as a limit for rejecting inaccurate observations, minor differences between

two consecutive solutions — before and after elimination of the poor-quality data — could cause that some data points with the residuals slightly exceeding the limit in the first solution (and therefore removed from the set of used observations) just satisfied the limit in the second solution (and were to be incorporated back into the set); while other data points with the residuals just satisfying the limit in the first solution (and therefore kept in the set) slightly exceeded the limit in the second solution (and were now to be removed from the set). In order to comply with the cutoff rule, it was necessary to iterate the process until the number of astrometric observations that passed the test fully stabilized.

As described in Section 3 below, the single observation of 1993 is known to be accurate to about $1''$, while nearly a half of the observations from 2005 and all from 2007–2010 were made with large telescopes; the more advanced solutions (Sections 6.2–6.3) showed a posteriori that these data points satisfied the tight limit and were not subjected to the aforementioned test.

With these basic rules in mind, we applied an orbit-determination code *EXORB7*, written by A. Vitagliano, both in its gravitational and nongravitational modes. Using the JPL DE421 ephemeris, the code accounts for the perturbations by the eight planets, by Pluto, and by the three most massive asteroids, as well as for the relativistic effect. The nongravitational accelerations are incorporated directly into the equations of motion (Section 4). The code employs a least-squares optimization method to derive the resulting elements and other parameters.

3. PAST WORK AND PURELY GRAVITATIONAL SOLUTIONS

The comet’s pre-discovery image from 1993, measured by McNaught (1995), is of major significance, because it extends the observed orbital arc by 27 months. Marsden (1999) commented on his (and other authors’) difficulties with linking this data point to the post-discovery, preperihelion observations and he emphasized the magnitude of the problem at the time by pointing to the possibility of “a significant unmodeled perturbation [that] must have been operative over a relatively short time interval,” in a reference to D. K. Yeomans. The situation was not alleviated by McNaught’s remeasurement of the comet’s 1993 image, which showed that its astrometric position was accurate to within $1''$. Also, McNaught’s positional verification of a known asteroid on the same plate confirmed the correct time. The problem was solved (temporarily) by assigning a greater weight to the 1993 data point. New difficulties arose in an effort to link the preperihelion observations with the post-perihelion observations near the end of 1997, and the nongravitational terms had to be introduced into the equations of motion. At the time of his paper’s submission (1998 early February), the 1993 observation (assigned a unit weight) was noted by Marsden (1999) to leave a residual of $1''.8$ in right ascension even with the nongravitational terms included.

Interestingly, Marsden’s (2007) last published orbit³ was gravitational, but the 1993 pre-discovery position was left out and 2817 observations were linked from only 1995 July 24 through 2007 October 22; the mean resid-

¹ See http://www.minorplanetcenter.net/db_search/.

² On a website <https://groups.yahoo.com/neo/groups/comets-ml/conversations/messages/19755/> D. Herald, Murrumbateman, Australia, reported a detection of C/1995 O1 on CCD images of a total exposure time of 144 minutes taken on 2012 August 7 with a 40-cm Schmidt-Cassegrain telescope. However, in response to our more recent inquiry, Mr. Herald stated in an e-mail message dated 2014 August 30 that he had been unable to independently confirm the detection. For additional information, see the Appendix A.

³ This set of elements is also listed in Marsden & Williams’ (2008) most recent edition of their catalog of cometary orbits.

Table 1

Our Purely Gravitational (PG) and Standard Nongravitational (SN) Orbital Solutions for Comet C/1995 O1 Compared with Three Previously Published Orbits (* Identifies Solutions with Stabilized Number of Used Observations)

Purely Gravitational Solutions					Standard Nongravitational Solutions				
Solution	No. of Used Observations	Mean Residual	Residual Cutoff	Time of Previous Perihelion (TT)	Solution	No. of Used Observations	Mean Residual	Residual Cutoff	Time of Previous Perihelion (TT)
PG I	2735	$\pm 0''.86$	$2''$	−2270 Feb 8	SN I	2870	$\pm 0''.75$	$2''$	−2202 Aug 5
PG II	2660	± 0.82	2	−2269 Apr 7	SN II	2899	± 0.75	2	−2206 Jan 20
PG III	2662	± 0.82	2	−2269 Nov 8	SN III*	2900	± 0.75	2	−2209 Dec 5
PG IV*	2648	± 0.81	2	−2268 Jan 20	SN IV	2465	± 0.63	1.5	−2208 Feb 12
Marsden ^a	2817	± 0.9	...	(−2272 Apr) ^c	SN VI*	2456	± 0.62	1.5	−2210 Sept 21
Williams ^b	2737	± 0.88	...	(−2264 Aug) ^c	Marsden ^d	2551	± 0.8	...	−2214 July 7

Notes.

^a Marsden (2007): derived from the orbital arc 1995 Jul 24 through 2007 Oct 22.

^b Williams (2011): derived from the orbital arc 1993 Apr 27 through 2010 Dec 4.

^c Estimated from the barycentric original semimajor axis; formal error of a few months.

^d Marsden (1999): derived from the orbital arc 1993 Apr 27 through 1998 Feb 8; parameter $A_3 = 0$.

ual equaled $\pm 0''.9$. On the other hand, the most recently published orbit, by Williams (2011), is based on gravitationally linking 2737 observations from the entire period 1993–2010, leaving a mean residual of $\pm 0''.88$; no details are available on the quality of fit.

The lesson learned from the obstacles encountered by Marsden (and others) in trying to fit a 57-month-long arc of the comet’s orbit leaves no hope that a solution based on the gravitational law alone could adequately represent a 211-month-long arc, nearly four times as long. We also suspected that the small number of observations available from the period of time after 2003 — not to mention the single 1993 pre-discovery observation — would eventually require their heavy weighting in comparison with the data from the interval of 1995–2003.

Given this history of orbit determination of C/1995 O1 and also in view of the need of a reference standard for our further computations, we first set to derive the best achievable purely gravitational solution. To begin with, we assigned a unit weight to each of the 3581 observations and computed an initial gravitational orbit. This step was necessary because of the lack of a priori information on the quality of the individual data points. This solution, whose mean (rms) residual came out to be $\pm 1''.56$, served to obtain a complete set of initial residuals. We noticed the presence of a few residuals exceeding $10''$ and a large number of residuals substantially exceeding $2''$; there were strong systematic trends in right ascension, with the residuals exceeding $4''$ in 2010. The 1993 pre-discovery observation left a residual exceeding $3''$ in declination.

Retaining an equal weight for all observations, these results prompted us to set a residual cutoff at $2''$ in either coordinate and to iterate the gravitational least-squares fitting to the observations until their employable number stabilized. The left-hand side of Table 1 shows that this task required four iterations to determine that the total number of observations satisfying this condition settled down — in the solution PG IV — on 2648 and the mean residual on $\pm 0''.81$. This solution places the comet’s previous passage through perihelion early in the year −2268. Comparison with the orbits by Marsden (2007) and by Williams (2011) shows that this perihelion time is close to an average of the two. On the other hand, it differs

by more than 50 yr from the perihelion time predicted by Marsden’s (1999) nongravitational solution.

The residuals $O-C$ from the solution PG IV are plotted in Figure 1. The fit can by no means be considered satisfactory, so the predicted perihelion passage in −2268 cannot be correct. In right ascension the observation of 1993 leaves an acceptable residual, but a distinctly systematic trend starts in 1998 from which time on the solution shows a progressive tendency toward negative residuals, reaching $-3''$ in 2010. In declination, the pre-discovery observation leaves a residual greater in absolute value than $2''$. Less prominent, short-term systematic trends are also seen at other times in both coordinates. Each residual that exceeds $2''$ is legitimate, as it does so because of an imperfect model.

4. STANDARD NONGRAVITATIONAL SOLUTIONS

Having confirmed that gravitational solutions are unacceptable, we next turned to solutions based on the standard nongravitational formalism, proposed by Marsden et al. (1973), in which the nongravitational terms were incorporated directly into the equations of motion and the magnitude of the nongravitational acceleration, as a function of heliocentric distance r , was expressed by an empirical formula $g_{ice}(r; r_0)$, designed to mimic the law of momentum transfer driven by the sublimation of water ice,

$$g_{ice}(r; r_0) = \psi \Lambda^{-m} (1 + \Lambda^n)^{-k}, \quad (1)$$

where $\Lambda = r/r_0$, r_0 is the scaling distance for water ice, exponents m , n , and k are constants, and ψ is a normalization coefficient, such that $g_{ice}(1 \text{ AU}; r_0) = 1$. Marsden et al.’s (1973) formalism employs a so-called isothermal model, which averages the Sun’s incident radiation over a spherical nucleus’ surface of constant temperature, assuming an albedo of 0.1 in both the optical and thermal spectral passbands. For this model, the parameters are $r_0 = 2.808 \text{ AU}$, $m = 2.15$, $n = 5.093$, $nk = 23.5$, and $\psi = 0.1113$. Even though the temperature of a cometary nucleus is known to vary greatly over the surface, for the orbit-determination purposes the employed simple model has served admirably over more than four decades and the formalism is still used today.

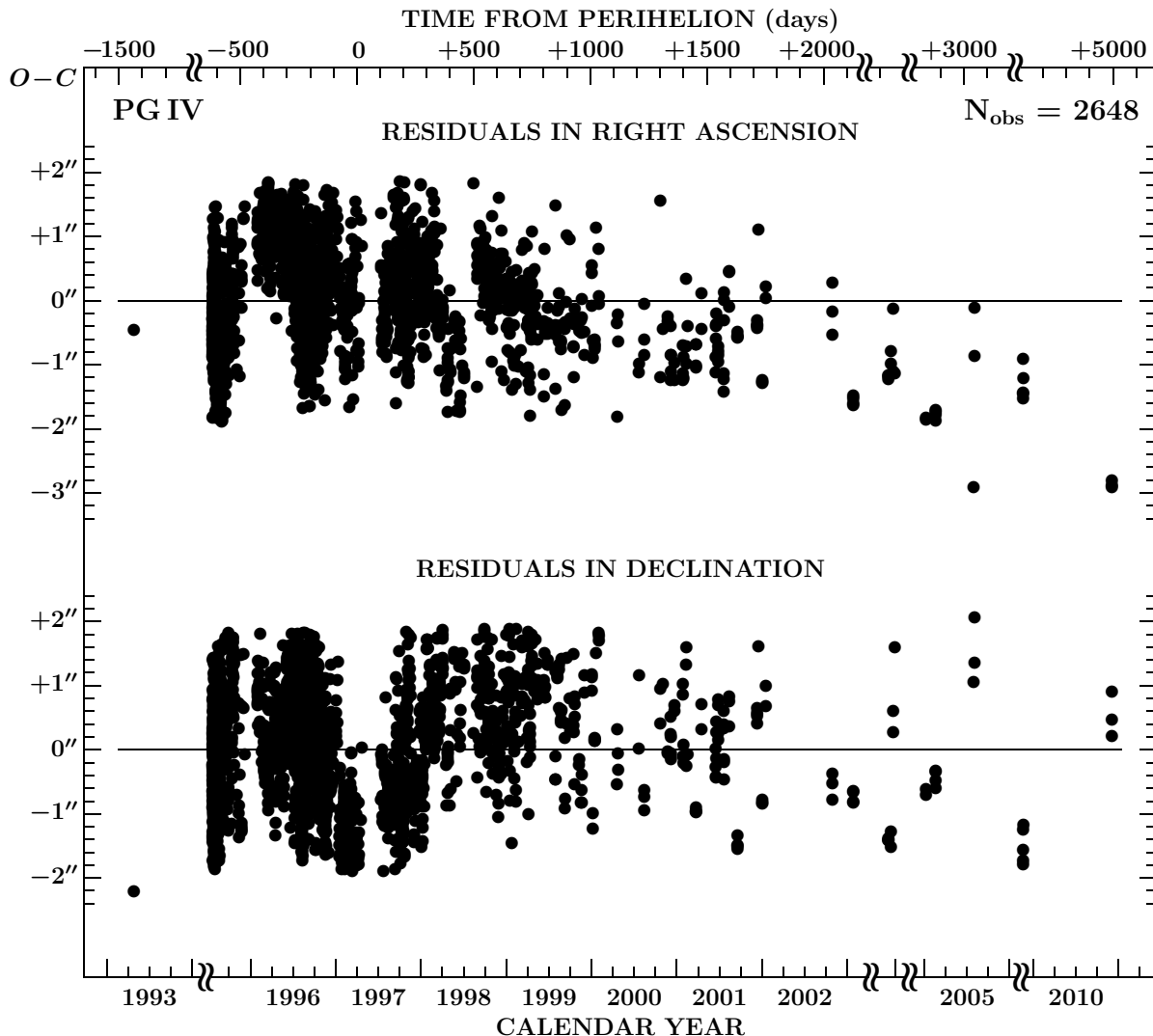


Figure 1. Temporal distribution of residuals $O-C$ (observed minus computed) in right ascension (top) and declination (bottom) from the gravitational solution PG IV to 2648 accurate observations of comet C/1995 O1 between 1993 and 2010. The axis of abscissae is interrupted in the years 1994–1995, 2003, 2004, 2006–2007, and 2007–2009 over periods of time with no observations. A strong systematic trend is apparent in right ascension starting in mid-1998 and reaching $3''$ by 2010. The pre-discovery observation leaves a residual exceeding $2''$ in declination. Less prominent systematic trends are apparent from 1995 to mid-1996 in right ascension and during much of 1997 and 1998 through part of 1999 in declination. All observations were given a unit weight.

Tested countless times in the past, this standard formalism stipulates a constant orientation of the momentum-transfer vector in an **RTN** right-handed rotating Cartesian coordinate system. Its cardinal directions, referred to the comet’s orbital plane, are the radial **R** (away from the Sun), transverse **T**, and normal **N** components. The components $j_{\mathbf{C}}(t)$ ($\mathbf{C} = \mathbf{R}, \mathbf{T}, \mathbf{N}$) of the nongravitational acceleration, to which the comet’s nucleus is subjected, are, at time t (when the heliocentric distance is r), equal to

$$\begin{bmatrix} j_{\mathbf{R}}(t) \\ j_{\mathbf{T}}(t) \\ j_{\mathbf{N}}(t) \end{bmatrix} = \begin{bmatrix} A_1 \\ A_2 \\ A_3 \end{bmatrix} \cdot g_{\text{ice}}(r; r_0), \quad (2)$$

where A_1 , A_2 , and A_3 are the magnitudes of the nongravitational acceleration’s components in, respectively, the radial, transverse, and normal directions at 1 AU from the Sun; they are the additional parameters that are, to-

gether with the orbital elements, determined from the employed observations in the process of orbit determination by applying a least-squares optimization procedure.

Retaining again an equal weight for all observations and a residual cutoff at $2''$, we iterated the standard nongravitational least-squares fitting to the observations until their number satisfying the conditions stabilized. Limited experimentation showed that the incorporation of the normal component of the nongravitational acceleration in addition to the usually included radial and transverse components improved the fit to a degree. The right-hand side of Table 1 indicates that after three iterations the number of employable observations leveled off at 2900, with the mean residual of $\pm 0''.75$ in the solution SN III. Thus, with somewhat higher accuracy than the solution PG IV, it accommodates ~ 250 more observations, suggesting that the incorporation of the nongravitational terms into the equations of motion definitely had beneficial effects.

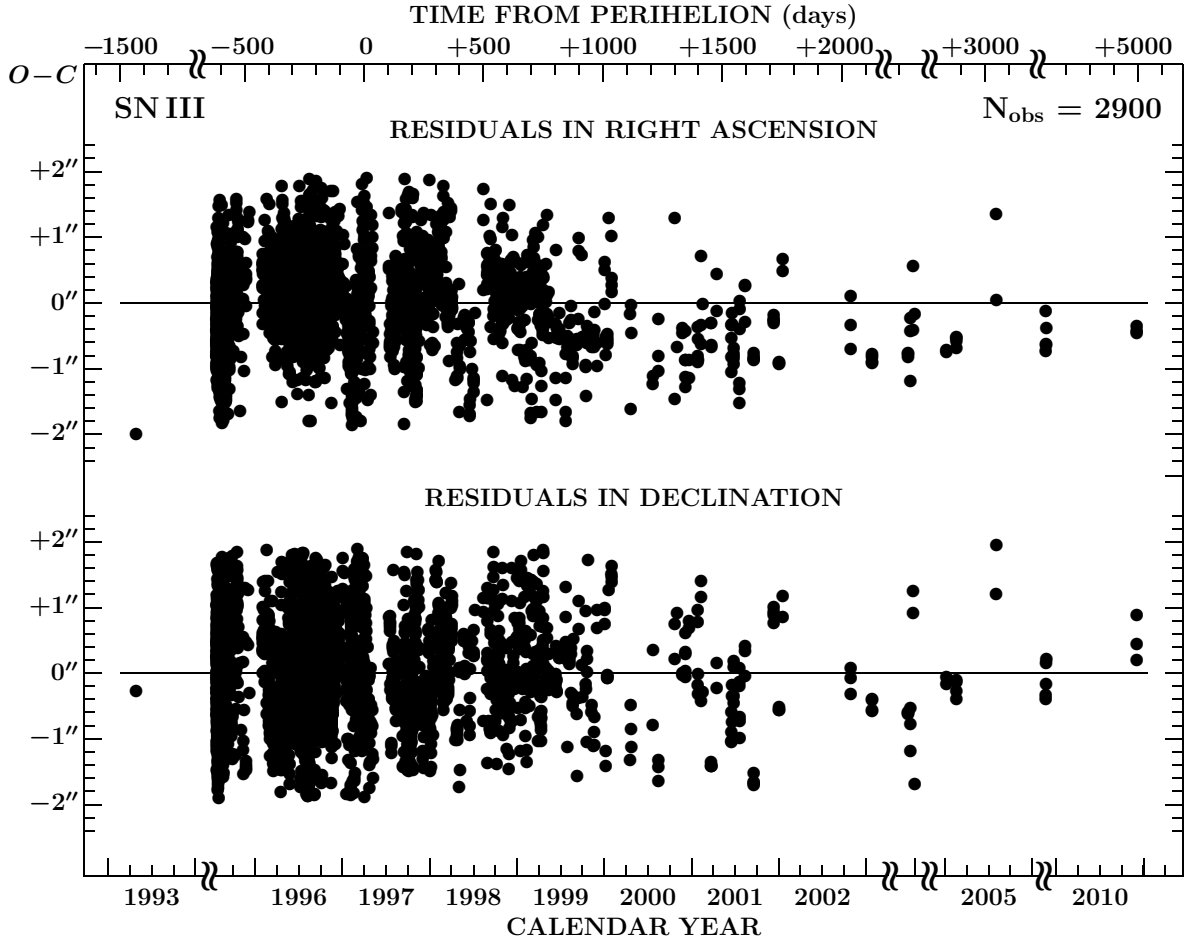


Figure 2. Temporal distribution of residuals $O-C$ (observed minus computed) in right ascension (top) and declination (bottom) from the standard nongravitational solution SN III to 2900 accurate observations of comet C/1995 O1 between 1993 and 2010. For more description, see the caption to Figure 1. The fit is now much better, but not quite acceptable. The pre-discovery observation leaves a residual of $2''$ in right ascension. A slight systematic trend in right ascension is seen between 1999 and 2010. Only in declination is the fit fairly satisfactory.

The solution SN III puts the comet's previous perihelion passage late in the year -2209 , within 6 yr of the time computed by Marsden (1999). It thus appears that, in terms of the previous perihelion time, there is a fair mutual agreement among the various gravitational orbits on the one hand and among the standard nongravitational orbits on the other hand, but that there is a systematic difference of some 50–60 yr between the two types of orbital solutions, the gravitational solutions predicting an earlier perihelion time.

The residuals $O-C$ from the solution SN III are plotted in Figure 2. The 1993 pre-discovery observation is now fitted satisfactorily in declination, but it leaves a residual of $2''$ in right ascension. The residuals from the years 1999–2010 are also fairly satisfactory in declination, but they have a tendency to be negative in right ascension. We conclude that the standard nongravitational law, although improving the match significantly, still fails to offer a perfect fit and leaves thus room for further improvement. In terms of the predicted perihelion time at the previous return to the Sun, the solution SN III does not necessarily offer a better estimate than the purely gravitational solution PG IV. This question also raises doubt about whether the comet did indeed return to perihelion in the year -2214 .

5. TIGHTENING THE CUTOFF FOR RESIDUALS

Before searching for a qualitatively superior approach in our quest for as perfect a distribution of residuals as possible, we considered it appropriate to further tighten the residual cutoff for the observations from the years 1995–2003 and possibly even 2005. We felt that the cutoff should not be tighter than, or competitive with, the reported accuracy of $\lesssim 1''$ of the pre-discovery observation (Marsden 1999), which we were determined to keep in the database under any circumstances. We eventually adopted a cutoff of $1''.5$.

To check the effect of the tightened cutoff on the sample size, the predicted previous perihelion time, and the nongravitational parameters under otherwise identical conditions, we continued the investigation by means of the standard nongravitational law. We found that, with the new cutoff, three iterations were needed to stabilize the number of employable observations; the runs were SN IV, SN V, and SN VI, the total numbers of used data points were, respectively, 2465, 2459, and 2456. The first and last of these solutions are presented in Table 1. As expected, the distribution of residuals from SN VI was, except for the drop in their range, very similar to that from SN III and, therefore, not entirely satisfactory.

Table 2
Parameters A_1 , A_2 , and A_3 from Nongravitational Solutions

Solution	Nongravitational Parameter (10^{-8} AU day $^{-2}$)		
	A_1	A_2	A_3
SN III	$+1.340 \pm 0.023$	$+0.0894 \pm 0.0036$	-0.0499 ± 0.0092
SN VI	$+1.270 \pm 0.021$	$+0.0918 \pm 0.0033$	-0.0797 ± 0.0085
Marsden ^a	$+1.04 \pm 0.03$	$+0.1759 \pm 0.0093$

Note.

^a The nongravitational solution from Table 1 (Marsden 1999).

Table 1 indicates that the number of employable observations in the solution SN VI dropped by only about 15 percent compared with SN III, a result that is a tribute to good work by the astrometrists. The predicted passage through perihelion moved back in time to September of -2210 , by less than 15 months and still closer to Marsden’s (1999) prediction. However, comparison of the nongravitational parameters, in Table 2, suggests that the cutoff’s tightening made important differences: the discrepancy between SN VI and SN III in the radial component’s and the normal component’s parameters, A_1 and A_3 , slightly exceeded 3σ , whereas the transverse component’s parameters, A_2 , of the two solutions agreed to within 1σ . The discrepancies between SN VI and Marsden’s (1999) orbit, computed with an assumed A_3 equal to zero, are rather startling, reaching $\sim 10\sigma$ in A_1 and $\gg 10\sigma$ in A_2 .

6. MODIFIED NONGRAVITATIONAL SOLUTIONS

In one of the previous papers (Sekanina & Kracht 2015), we introduced a generic *modified nongravitational law*, $g_{\text{mod}}(r; r_0)$, and applied it to considerable advantage in our investigation of the dwarf Kreutz sungrazing comets, discovered in enormous numbers with the coronagraphs onboard the *Solar and Heliospheric Observatory (SOHO)*; Brueckner et al. 1995) and, to a lesser degree, also with the coronagraphs onboard the two spacecraft of the *Solar Terrestrial Relations Observatory (STEREO)*; Howard et al. 2008).

The modified nongravitational (MN) law retains the values of the exponents m , n , and k of the standard law (1), but varies the scaling distance r_0 and the constant ψ . This intervention is fully justified on account of Marsden et al.’s (1973) finding that the shapes of the normalized sublimation-rate curves against heliocentric distance for a variety of species are fairly similar in a log-log plot except for major horizontal shifts, which means that they are relatively insensitive to the exponents m , n , and k , but critically dependent on the scaling distance r_0 . For a given absorptivity and emissivity of the nuclear surface, r_0 measures essentially an effective latent heat of sublimation, L_{sub} , of the observed mix of outgassing species, varying to a first approximation inversely as the square of L_{sub} ,

$$r_0 \simeq \left(\frac{\text{const}}{L_{\text{sub}}} \right)^2, \quad (3)$$

where a calibration by water-ice gives for the constant a value of $19\,100 \text{ AU}^{\frac{1}{2}} \text{ cal mol}^{-1}$ in the case of an isothermal model.

For the dwarf comets of the Kreutz sungrazing system the application of this modified version of the nongravitational law was instrumental because the species that were sublimating profusely from their disintegrating nuclei in close proximity of the Sun were *much less* volatile than water ice (Sekanina & Kracht 2015); these refractory materials have $r_0 \ll 2.8$ AU. For C/1995 O1, on the other hand, the modified law is necessary because a large body of data (e.g., Crovisier et al. 1996, 1997; Jewitt et al. 1996; Biver et al. 1997, 1999; Bockelée-Morvan & Rickman 1999; Crovisier 1999; Despois 1999; DiSanti et al. 1999) provides undisputable evidence for abundant release of species *much more* volatile than water ice; for these ices, in particular for carbon monoxide and carbon dioxide, $r_0 \gg 2.8$ AU.

6.1. Assigning Greater Weights to Critical Observations

A number of initial orbital runs based on the modified nongravitational law consistently showed that the fit to the observations could not be improved significantly and the systematic trends in the residuals at the ends of the orbital arc removed, unless these first and last observations — that we hereafter call *critical* — were assigned substantially greater weights than the observations near the arc’s middle. We first allotted weight 40 to the pre-discovery observation in 1993, weight 20 to each of the three observations on 2010 December 4, and weight 10 to each of the five observations on 2007 October 20–22, so that we had at that point a total of 9 critical observations. All other employed observations, from the years 1995–2005, were allotted a unit weight.

We searched for orbital solutions based on a set of the observations weighted this way assuming several scaling distances r_0 and compared the mean residual left by all the observations used with the mean residual left only by the critical observations. In the subsequent runs we changed the weight assignment and included the 2005 observations among the critical ones. Some of the solutions obtained as we tried to stabilize the number of observations satisfying the residual cutoff of $1''.5$ (similarly to the solutions PG I through PG IV and SN I through SN III in Table 1), are presented in Table 3. They show the assigned weights and a dramatic impact of the stabilization process on the number of retained observations.

These results provide an answer to the stubborn problem that Marsden (1999) was struggling with in his effort to accommodate the pre-discovery observation. The bottom line is that this could readily be done (with a residual of $< 0''.5$) by weighting the observation heavily enough; however, the resulting orbital solutions demanded rejection of almost one half of all observations that we started with (~ 2900), because their residuals failed to satisfy the tight cutoff. We investigated the temporal distribution of the rejected observations and found that nearly 500 (or one third) of them came from the period of time between mid-March 1997 and early March 1998 (two weeks before perihelion to 11 months after perihelion) and that only very few acceptable observations from this time remained in the set. A vast majority of the rejected observations left residuals that were positive in right ascension and negative in declination. For example, the 69 rejected observations during 1997 April left an average residual of $+3''.0 \pm 1''.4$ in right ascension and $-4''.4 \pm 1''.9$ in declination; similarly, the average residuals amounted, for

Table 3
Some Modified Nongravitational Solutions with Weighted Observations, and Offset of Pre-Discovery Observation

Solution	Assigned Weights ^a	Number of Used/Critical Observations	Scaling Distance r_0 (AU)	Mean Residual		Offset from Pre-Discovery Observation	Time of Previous Perihelion (TT)
				All Obs.	Crit. Obs.		
MN VII	40; 1;10;20	2452/9	0.5	$\pm 0''.77$	$\pm 0''.44$	0''.86	-2232 Mar 4
MN IX	40;10;20;40	2189/16	0.5	± 0.76	± 0.39	0.79	-2237 Sept 28
MN XI	40;10;20;40	2189/16	6.0	± 0.86	± 0.38	0.80	-2244 Dec 16
MN XII	40;10;20;40	1928/16	6.0	± 0.83	± 0.38	0.80	-2247 Oct 20
MN XIII	40;10;20;40	1771/16	6.0	± 0.76	± 0.38	0.57	-2251 Nov 2
MN XIV	40;10;20;40	1606/16	6.0	± 0.71	± 0.38	0.42	-2255 July 8
MN XV	40;10;20;40	1532/16	6.0	± 0.68	± 0.38	0.34	-2258 Dec 11
MN XVI	40; 5;10;20	1531/15	6.0	± 0.669	± 0.228	0.29	-2257 Oct 5
MN XVII	40; 5;10;20	1523/15	6.0	± 0.663	± 0.225	0.27	-2257 July 2
MN XVIII	40; 5;10;20	1540/15	6.0	± 0.667	± 0.224	0.27	-2257 Oct 9
MN XIX	40; 5;10;20	1540/15	3.0	± 0.660	± 0.233	0.27	-2249 Jan 31

Note.

^a The four weights refer to all observations (called critical) used, respectively, from the years 1993, 2005, 2007, and 2010; all other retained observations are assigned a unit weight.

example, to $+2''.5 \pm 1''.2$ and $-2''.3 \pm 1''.3$, respectively, from the 88 rejected observations during 1997 October, and to $+2''.2 \pm 0''.9$ and $-1''.2 \pm 0''.5$, respectively, from the 40 rejected observations during 1998 February. These offsets do not correlate with any cardinal direction, such as the antisolar direction. From Table 3 we note the lack of correlation between the mean residual from all the used observations and the mean residual from the critical observations. For example, comparison of the solutions MN IX and MN XI suggests that the fit with a scaling distance r_0 of 0.5 AU is clearly better than the fit with $r_0 = 6$ AU in terms of all the employed observations, but slightly worse in terms of the critical observations. The solutions MN XI through MN XV indicate, on the other hand, that for a given scaling distance the quality of fit does not change among the critical observations, but it improves among all the used observations as their number drops dramatically. The highly weighted 1993 pre-discovery observation is nonetheless fitted the better the smaller is the mean residual from all the used observations. We further note from Table 3 that, as the number of retained observations drops, the previous perihelion passage moves systematically by many years to earlier times; the perihelion time predicted from the solution MN XV is within 11 years of the time predicted in Table 1 from the gravitational solution PG IV!

The last four entries of Table 3, whose weights for the critical data — 40 (1993), 5 (2005), 10 (2007), 20 (2010) — are hereafter called the *Weight System I*, are the most important ones. The last observation of 2005 was now rejected, leaving just 15 critical observations, with the total number of observations eventually stabilized at 1540. MN XVIII and MN XIX, which fit the data points essentially equally well, are the basis for deriving the optimum solution, the final step in our orbit-determination effort; it is dealt with in the next subsection.

Before addressing that issue, we should comment on the properties and the implications of the most important solutions in Table 3, MN XVI through MN XIX. These solutions require, similarly to MN XV, that nearly all the observations between mid-March 1997 and early March 1998 be rejected. The nongravitational parameters from MN XVI through MN XIX, listed in Table 4, reveal some

interesting features. The most surprising is that by far the highest acceleration is in the direction normal to the orbital plane, A_3 . We will return to this result in the section in which we confront orbital evidence with information on the nuclear rotation of the comet. Table 4 also shows that the ratio of $|A_3|/A_1$ varies strongly with the scaling distance r_0 , dropping from near 10 at $r_0 = 6$ AU to a little over 2 at $r_0 = 3$ AU, when the transverse component A_2 is very small and poorly defined.

Comparison with the solutions SN III and SN VI from Table 2 also offers some rather unexpected conclusions. The total magnitude of the nongravitational acceleration, $\sqrt{A_1^2 + A_2^2 + A_3^2}$, is now lower by a factor of ~ 2 . For the solutions MN XVI through MN XVIII this could be understood as an effect of the scaling distance (which of course equaled 2.8 AU for the SN solutions), because a greater scaling distance means a greater contribution to the integrated effect from larger heliocentric distances. However, this does not explain the factor of 2 between the SN solutions and MN XIX, whose r_0 was nearly the same. The incompatibility of the SN and MN results is also underscored by the opposite signs of the transverse component. It thus appears that assigning weights to the critical observations and relaxing the scaling distance had a major effect on the results.

6.2. Weight System I: Final Optimization of Orbit

Table 3 shows that the uncertainty in the scaling distance r_0 implies an uncertainty of at least several years in the time of perihelion passage in the 23 century BCE. Because of this indeterminacy, it could never be proven

Table 4
Parameters A_1 , A_2 , and A_3 from Solutions MN XVI–MN XIX

Solution	Nongravitational Parameter (10^{-8} AU day $^{-2}$)		
	A_1	A_2	A_3
MN XVI	$+0.068 \pm 0.035$	-0.0144 ± 0.0027	-0.635 ± 0.021
MN XVII	$+0.063 \pm 0.036$	-0.0166 ± 0.0028	-0.691 ± 0.022
MN XVIII	$+0.074 \pm 0.036$	-0.0169 ± 0.0029	-0.719 ± 0.023
MN XIX	$+0.270 \pm 0.030$	-0.0042 ± 0.0030	-0.634 ± 0.020

Table 5

Orbital Elements and Encounter Parameters for Nominal Solution of C/1995 O1 with Weight System I (Equinox J2000)

Orbit at Apparition 1993–2010		
Epoch of osculation (1997 TT)	Mar 13.0	
Time of perihelion (1997 TT)	Apr 1.13747 ± 0.00006	
Argument of perihelion	130°.587433 ± 0°.000071	
Longitude of ascending node	282°.469632 ± 0°.000006	
Orbit inclination	89°.429219 ± 0°.000016	
Perihelion distance (AU)	0.9141709 ± 0.0000013	
Orbit eccentricity	0.99511278 ± 0.00000061	
Orbital period (yr)	{ original ^a	4249.0
	{ osculating	2558.3 ± 1.1
	{ future ^a	2397.7
Longitude of perihelion	101°.8034	
Latitude of perihelion	+49°.4092	
Nongravitational parameters:		
Law applied	modified	
Scaling distance r_0 (AU)	3.070	
Normalization constant Ψ	0.09105	
A_1 [radial] (10^{-8} AU day $^{-2}$)	+0.266 ± 0.031	
A_2 [transverse] (10^{-8} AU day $^{-2}$)	−0.0045 ± 0.0031	
A_3 [normal] (10^{-8} AU day $^{-2}$)	−0.635 ± 0.020	
Solution parameters:		
Mean residual	±0".66	
Time period covered	1993 Apr 27–2010 Dec 4	
Orbital arc (days)	6429.54	
Total observations used	1540	
Critical observations used	15 ^b	
Post-Encounter Orbit in 23rd Century BCE		
Epoch of osculation (−2250 TT)	Dec 8.0	
Time of perihelion (−2250 TT)	Dec 8.0659	
Argument of perihelion	130°.4076	
Longitude of ascending node	282°.3700	
Orbit inclination	89°.0530	
Perihelion distance (AU)	0.907236	
Orbit eccentricity	0.996749	
Orbital period (yr)	{ osculating	4661
	{ future ^a	4249
Longitude of perihelion	101°.26	
Latitude of perihelion	+49°.58	
Pre-Encounter Orbit in 23rd Century BCE		
Epoch of osculation (−2255 TT)	Jan 1.0	
Time of perihelion (−2250 TT)	Oct 10.8350	
Argument of perihelion	340°.4131	
Longitude of ascending node	102°.3538	
Orbit inclination	92°.2032	
Perihelion distance (AU)	0.151986	
Orbit eccentricity	0.999986	
Orbital period (yr)	{ original ^a	~3 200 000
	{ osculating	1 090 000
Longitude of perihelion	103°.14	
Latitude of perihelion	−19°.57	
Encounter Parameters		
Time of perijove (−2251 TT)	Nov 7.34399	
Jovicentric distance at perijove (R_J) ^c	10.78	
Angle Sun–Jupiter–comet at perijove	82°.0	
Jovicentric velocity at perijove (km s $^{-1}$)	28.72	

Notes.^a Derived from the original (or future) semimajor axis referred to the barycenter of the Solar System.^b Of these, one in 1993, six in 2005, five in 2007, and three in 2010.^c $R_J = 71\,492$ km is adopted equatorial radius of Jupiter.

that C/1995 O1 did in fact experience a close encounter with Jupiter. However, pursuing Marsden’s (1999) suggestion that “*it is not entirely improbable that [the comet underwent] a recent dramatic approach*” to the planet, we exploited the tabulated dependence of the previous perihelion time on the scaling distance. By slightly adjusting r_0 , we were able to determine the time of perijove and the corresponding Jovicentric distance that were compatible with plausible pre-encounter orbital constraints. We found that the comet had to pass through perihelion in early December of −2250 in order to approach closely Jupiter. This was the planet’s only revolution that was consistent with the close-encounter requirement.

To achieve a similarly favorable configuration during the previous Jovian revolution, the comet would have to have passed through perihelion in late January of −2261. However, this time requires $r_0 \approx 8$ AU, for which the radial parameter $A_1 < 0$, in contradiction to the physical model of nongravitational forces.

On the other hand, a favorable configuration one Jovian revolution later would require that the comet’s perihelion occurred in mid-October of −2238. A set of computer runs showed that, unfortunately, there was no solution with a perihelion time later than near the end of −2247, and even that implied an unrealistically small scaling distance of $r_0 < 1$ AU.

A fine tuning of the orbital elements, starting with the set MN XIX in Table 3 and based, as described below, on the constraint that C/1995 O1 was in the previous return a dynamically new comet, resulted in a nominal solution with Weight System I, which is presented in full detail in Table 5. The perihelion time on −2250 December 8 suggests that Marsden’s (1999) choice for the encounter time was three Jovian revolutions much too late.

Table 6 provides insight into the optimization procedure that was employed to select the solution in Table 5. The time of perijove, t_J , correlates tightly with both the

Table 6

Correlations Between Time at Perijove, Jovicentric Distance, and Pre-Encounter Original Orbit (Weight System I)

At Perijove on −2251 Nov 7		Pre-Encounter Original Orbit	
Time, t_J (TT)	Jovicentric Distance, ^a $\Delta_J (R_J)$	Reciprocal Semimajor Axis, ^b $(1/a)_{\text{orig}} (\text{AU}^{-1})$	Orbital Period, $P_{\text{orig}} (\text{yr})$
5:11:56	10.612	−0.049219
7:30:35	10.700	−0.011969
8:11:56	10.777	−0.000850
8:14:22	10.782	−0.000201
8:15:40	10.784	+0.000146	567 000
8:17:19	10.788	+0.000585	70 700
8:17:38	10.789	+0.000668	57 900
8:19:15	10.793	+0.001100	27 400
8:23:50	10.803	+0.002318	8960
8:49:59	10.868	+0.009306	1130
9:03:21	10.905	+0.012682	700
10:08:46	11.122	+0.029100	201
11:27:38	11.461	+0.045925	102
17:12:06	13.830	+0.101475	30.9

Notes.^a $R_J = 71\,492$ km is adopted equatorial radius of Jupiter.^b Referred to the barycenter of the Solar System.

Jovicentric distance at the time, $\Delta_J(t_J)$, and with the pre-encounter orbit's original semimajor axis, $(1/a)_{\text{orig}}$ (referred to the barycenter of the Solar System), or the equivalent original orbital period, P_{orig} . The interval of t_J in Table 6, covering 12 hours on November 7 of the year -2251 , corresponds to an interval of 0.001 AU in the scaling distance r_0 and shows that the minimum perijove distance Δ_J was attained certainly before 7:00. Although we will estimate the exact time below, it is outside the range of interest because the comet would then have arrived along a strongly hyperbolic orbit, an unacceptable scenario.

Realistically, the comet should have passed through perijove after 8:15:11, when its pre-encounter barycentric orbit was elliptical. If C/1995 O1 was a dynamically new comet arriving from the “core” region of the Oort Cloud — for which we adopt with Marsden et al. (1978) a heliocentric distance of $\sim 43\,000$ AU) — it would have arrived at perijove just 10 seconds later, at 8:15:21. The comet's original orbital period would have then amounted to some 3 200 000 yr, its Jovicentric distance at perijove would have been near $10.8 R_J$, and its Jovicentric velocity about 29 km s^{-1} , as the nominal solution in Table 5 indicates.

Of course, C/1995 O1 may have been a long-period comet before the encounter, but not dynamically new. If so, it would have arrived later still, perhaps as late as 8:30 or even 9:00. Its perijove distance would then have been only slightly greater. For two related reasons it is, however, less likely that the comet had moved in an orbit of a relatively short period before the encounter: (i) it would have had a high probability of approaching Jupiter on a number of occasions at times before this encounter and (ii) having made many revolutions about the Sun with a very small perihelion distance, it would long ago have gotten depleted of highly volatile species, in conflict with the observations (Section 9).

The steep dependence of the original barycentric semimajor axis, $(1/a)_{\text{orig}}$, on the time of perijove, t_J , during the day of -2251 November 7 is illustrated in Figure 3. Although the relationship is more complex over wider intervals of time, a straight-line approximation is satisfactory over intervals shorter in t_J than about 2 hr. A least-squares fit to the data points between $\sim 7:30$ and $\sim 9:00$, which was used above to pinpoint the time of perijove for C/1995 O1 as an Oort Cloud comet, can be expressed as follows:

$$(1/a)_{\text{orig}} = -0.004009 + 0.015850 (t_J - 8^{\text{h}}), \quad \pm 0.000011 \pm 0.000024 \quad (4)$$

where $(1/a)_{\text{orig}}$ is in $(\text{AU})^{-1}$ and t_J in hr.

Similarly, the relationship between the time of perijove and the perijove distance, Δ_J , is over the entire interval of time from 5:10 to 11:30 approximated by a least-squares polynomial

$$\Delta_J = 10.751826 + 0.1191931(t_J - 8^{\text{h}}) + 0.024733(t_J - 8^{\text{h}})^2, \quad \pm 0.000006 \pm 0.0000002 \quad \pm 0.000001 \quad (5)$$

where Δ_J is expressed in units of the Jovian equatorial radius R_J ($1 R_J = 71\,492 \text{ km}$) and t_J is again in hr. A search for a minimum provides $(\Delta_J)_{\text{min}} = 10.608 R_J$ at $(t_J)_{\text{min}} = 5:35:25$ or $2:39:56$ before the perijove time for C/1995 O1 as an Oort Cloud comet.

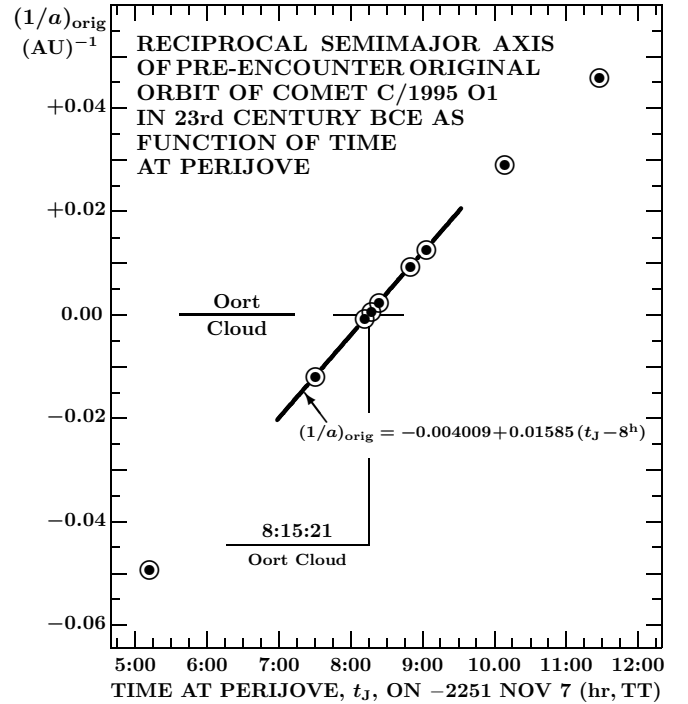


Figure 3. Plot of the reciprocal semimajor axis of the comet's pre-encounter original barycentric orbit, $(1/a)_{\text{orig}}$, against the time at perijove, t_J , on -2251 November 7. To prevent overcrowding, only some of the 14 entries from Table 6 are displayed. They all are distributed along a curve that over intervals shorter than 2 hr can with high accuracy be approximated with a straight line, as shown. An arrival from the Oort Cloud is depicted with a horizontal line at $(1/a)_{\text{orig}} = +0.000046 (\text{AU})^{-1}$ and described with a corresponding perijove time of 8:15:21 TT.

The orbit in Table 5, referred to the osculation epoch of 1997 Mar 13, is generally in accord with the published gravitational orbits. For example, it agrees with Marsden's (2007) orbit to better than 90 seconds in the perihelion time, to better than $4''$ in the angular elements, to better than 1000 km in the perihelion distance, and to better than 20 yr in the osculating orbital period. However, with the exception of the argument of perihelion, our formal errors are smaller than the differences, in some of the elements by two orders of magnitude. The original values of the orbital period derived by us and by Marsden deviate by 20 yr, the future period by 8 yr. Our result predicts for the previous perihelion time the year -2252 , Marsden's orbit the year -2272 (cf. Table 1).

A more recent gravitational orbit, by Williams (2011), differs from our nominal solution by 45 seconds in the perihelion time, by $0''.1$ in the argument of perihelion, by $3''.6$ in the longitude of the node, by $3''.0$ in the inclination, by 450 km in the perihelion distance, and by 12 yr in the osculation orbital period. It predicts that the previous perihelion time occurred in the year -2264 (cf. Table 1). In general, Marsden's (2007) and Williams' (2011) orbits agree with each other better than either of them with our orbit. We suspect that this is so in part because of our incorporation of the nongravitational terms in the equations of motion, although the weighting of the critical observations may also have an effect. As already noted in Sections 4 and 6.1, the normal component of the nongravitational acceleration — which has hardly

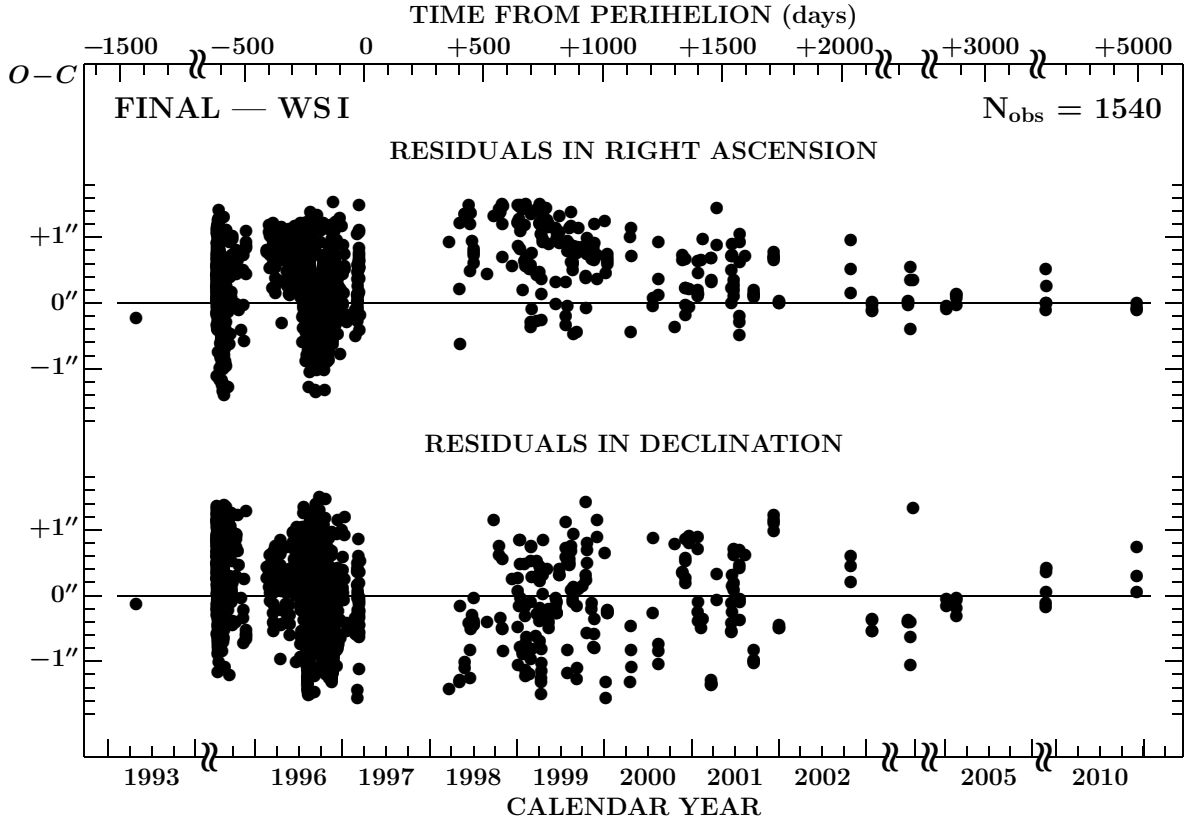


Figure 4. Temporal distribution of residuals $O-C$ (observed minus computed) in right ascension (top) and declination (bottom) from the nominal nongravitational solution listed in Table 5, based on 1540 accurate observations of comet C/1995 O1 between 1993 and 2010, which left residuals not exceeding $1''.5$ in either coordinate. The fit is judged perfect in declination, but many observations from 1998–2000 still leave mostly positive residuals.

ever been employed in orbital computations of comets — not only improves the fit, but turns out to be the most prominent component, more than twice the magnitude of the radial component. On the other hand, the transverse component is very small and poorly defined. The overall magnitude of the nongravitational acceleration at 1 AU from the Sun is 0.69 ± 0.02 AU day $^{-2}$, or about one half the acceleration that resulted from the standard nongravitational solutions (Table 2). This is noteworthy because the magnitude of the nongravitational acceleration derived earlier was judged to be too high to be compatible with the presumably large nucleus of the comet (Marsden 1999, Sosa & Fernández 2011).

The scaling distance r_0 of the nongravitational law in the nominal solution in Table 5 is only slightly greater than the scaling distance for water ice in Equation (1). This result can be interpreted to mean that the nongravitational effect was due largely to water ice, with only relatively minor contributions from more volatile species. We return to this issue in Section 9.

Somewhat surprising is the very small perihelion distance, of only about 0.15 AU, of the pre-encounter orbit. Two other prominent dynamically new comets approached the Sun to a similar distance, C/1973 E1 (Kohoutek) and C/2006 P1 (McNaught), but in terms of the inclination the pre-encounter orbit of C/1995 O1 is much more similar to the latter of the two comets. And while the orbital plane’s nodal line and inclination were affected very little by the Jovian encounter (by $1'$ and a lit-

tle more than 3° , respectively), the line of apsides moved by 69° (*sic!*), the nodes got interchanged, and the perihelion distance increased by a factor of six. C/1995 O1 passed through perihelion two months later than it would have in its pre-encounter orbit.

The distribution of residuals from the nominal solution in Table 5 left by the 1540 retained observations is displayed in Figure 4. The distribution is satisfactory in declination, but there is a significant excess of positive residuals in right ascension in the course of 1998 and 1999. This is a tail of the set of much more strongly positive residuals left by the observations made between mid-March 1997 and early March 1998, all of which had to be discarded from the nominal solution. There are two clusters of residuals in R.A. in Figure 4 in the 1998–1999 time slot — an upper dense one and a lower sparse one — separated by a tilted strait with no data points. The lower, lightly populated cluster contains observations that are more consistent with the solution in Table 5.

To investigate this peculiar double-cluster distribution in greater detail, we present in Table 7 a dozen observations from either cluster, made in the period of time from early May 1998 through early May 1999. Each observation with the residuals is identified by the observing site code and the reference to a *Minor Planet Circular* (MPC), in which it was published. From the list of observing sites that always precedes the list of reported observations in the MPCs, we extracted the information on each instrument’s aperture and the f ratio and converted

Table 7

Systematic Residuals in Right Ascension, from Nominal Orbit with Weight System I, of Sample Observations from May 1998–May 1999

Sparse Cluster (Residuals Not Exceeding $0''.7$ in R.A.)						Dense Cluster (Residuals Exceeding $1''.2$ in R.A.)					
Time of Observation (UT)	Residual $O-C$		Obs. Site Code	Image Scale (mm^{-1})	Reference MPC	Time of Observation (UT)	Residual $O-C$		Obs. Site Code	Image Scale (mm^{-1})	Reference MPC
	R.A.	Decl.					R.A.	Decl.			
1998 May 8.96560	$-0''.63$	$-0''.16$	834	$131''$	32 129	1998 May 6.96538	$+1''.22$	$-1''.29$	844	$90''$	31 853
July 4.82718	-0.04	$+0.60$	422	201	32 129	28.39198	$+1.36$	-1.10	422	201	31 853
Aug 29.35072	$+0.45$	-0.40	834	131	32 379	June 14.35473	$+1.49$	-0.42	422	201	32 129
Nov 1.14909	$+0.70$	$+0.55$	844	90	32 821	21.91409	$+1.37$	-0.51	834	131	32 129
Dec 12.30799	$+0.56$	$+0.25$	808	55	33 415	Sept 26.24039	$+1.32$	$+1.15$	844	90	32 821
1999 Jan 26.03839	$+0.20$	-0.89	834	131	34 676	Nov 4.28320	$+1.48$	-0.84	834	131	33 415
Feb 1.12505	$+0.64$	$+0.49$	834	131	34 676	1999 Jan 4.49222	$+1.49$	$+0.07$	422	201	33 415
4.03494	$+0.64$	-0.31	834	131	34 676	15.44743	$+1.45$	$+0.85$	422	201	33 616
28.11036	-0.30	-0.10	834	131	35 767	Feb 8.07250	$+1.50$	-0.72	834	131	35 767
Mar 5.02648	-0.09	$+0.29$	834	131	35 767	Mar 22.06831	$+1.41$	-0.62	834	131	35 767
26.08788	-0.28	$+0.53$	844	90	34 092	Apr 7.08498	$+1.50$	$+0.22$	844	90	34 387
Apr 13.97924	$+0.14$	-0.82	834	131	35 767	May 3.40045	$+1.44$	-0.27	426	208	34 387

it into the image scale presented in column 5 of Table 7. The aim was to check whether there was any systematic difference between the image scales (CCD pixel sizes were unfortunately unavailable) of the instruments employed to make the seemingly more accurate observations on the left and the image scales of the instruments used to make the observations leaving systematic residuals in R.A. on the right. As seen from the table, it turned out that the same instrument sometimes provided acceptable residuals, while at other times it did not. The average image scale for the observations on the left is better than that on the right, but only by a small margin of $124'' \text{mm}^{-1}$ vs $151'' \text{mm}^{-1}$. This result means that the problem with the residuals in R.A. either lies elsewhere or the cutoff of $\pm 1''.5$ is tighter than the level of accuracy achievable by the category of telescopes (with apertures of, generally, 25–50 cm) used by most observers at the times the comet was bright enough to be within their reach. We note that on the one hand, the systematic trend in R.A. is limited to the time interval of high activity (associated with a complex coma morphology), but it fails to correlate with the comet’s orientation relative to the Sun, so that the offsets cannot readily be attributed to sunward or antisunward condensations.

6.3. Introduction of New Weight System

The distribution of residuals might be sensitive to the weight assigned to the pre-discovery observation of 1993. It is recalled that it indeed was this observation’s residual in R.A. that caused problems when attempts were made in 1998 to link it with the post-discovery observations (Marsden 1999). The weight system applied in Section 6.2, which assigned the 1993 observation weight 40, resulted in an excellent fit to this data point by the nominal solution in Table 5, leaving a residual of $-0''.23$ in R.A. and $-0''.14$ in decl. (Figure 4). Given the position’s uncertainty “within 1 arcsec” (Marsden 1999) — the 124 cm UK Schmidt telescope, with which the observation was made, has an image scale of $\sim 67'' \text{mm}^{-1}$ — one should allow these residuals to become quite a bit greater and still consistent with the stated astrometric error. The implication is that the weight assigned to the

1993 observation was unnecessarily high and that a lower weight might be more appropriate.

The weight assignment to the critical observations, not only to the pre-discovery observation, also has broader ramifications in terms of the orbital results and predictions of the comet’s motion in the previous return to the Sun. It is therefore desirable to address this issue in greater detail. To examine the impact, we chose a set of different weights, called hereafter Weight System II, as follows: the observation of 1993 was assigned weight 20 (instead of 40), the 2010 observations weight 15 (instead of 20), while the weights of the 2005 and 2007 observations were left unchanged at 5 and 10, respectively.

We then proceeded in a way similar to that in Section 6.1, with the nominal solution in Table 5 used as a starting set of elements in the iterative procedure of stabilizing the number of retained observations. However, unlike before (Table 3), at each step of the process we optimized the scaling distance r_0 of the modified nongravitational law to fit the encounter time. Accordingly, we were successively deriving the solutions MN XXI to MN XXVII listed in Table 8.

The results, which again allow a close approach only in the year -2251 but not in -2262 or -2239 , are rather striking. The first iteration with Weight System II immediately indicated that 180 more observations, whose residuals exceeded the cutoff of $\pm 1''.5$ before, would now fit. Simultaneously the scaling distance increased dramatically by almost 5 AU, while the offset of the 1993 pre-discovery observation grew to about twice the offset of the nominal solution in Table 5 (Figure 4), still well within the reported uncertainty. The first solution was far from stabilizing the number of retained observations, and the trend continued: 121 additional observations were accommodated by the second iteration, which required a scaling distance greater by a yet another 2 AU, while the offset of the pre-discovery observation now increased to more than $0''.8$ and was slowly approaching the limit of the measured error. After five more iterations, the number of retained observations finally stabilized at 1950, an increase by more than 500 relative to the solution in Table 5. Interestingly, in spite of these

Table 8
Modified Nongravitational Solutions Using Weight System II, and Offset of Pre-Discovery Observation

Solution	Number of Used/Critical Observations	Scaling Distance r_0 (AU)	Mean Residual		Offset from Pre-Discovery Observation	Time of Previous Perihelion (TT)
			All Obs.	Crit. Obs.		
MN XXI	1720/15	7.78	$\pm 0''.629$	$\pm 0''.256$	0''.61	-2250 Dec 8.0
MN XXII	1841/15	9.76	± 0.636	± 0.266	0.84	-2250 Dec 8.8
MN XXIII	1889/15	11.29	± 0.638	± 0.271	0.93	-2250 Dec 8.7
MN XXIV	1915/15	12.72	± 0.638	± 0.276	0.98	-2250 Dec 8.9
MN XXV	1931/15	13.74	± 0.639	± 0.278	1.01	-2250 Dec 8.7
MN XXVI	1943/15	14.80	± 0.639	± 0.280	1.02	-2250 Dec 8.0
MN XXVII	1950/15	15.36	± 0.639	± 0.281	1.03	-2250 Dec 8.5

additional accommodated data points the mean residual dropped slightly in comparison with the nominal solution in Table 5. However, the mean residual of the 15 critical observations increased a little, unquestionably owing to the greatly increased offset of the pre-discovery observation. This offset was now at the limit of uncertainty, with the residuals, in the sense “observed minus computed”, amounting to $-0''.86$ in right ascension and $-0''.57$ in declination.

The nongravitational parameters derived from the solutions MN XXI through MN XXVII likewise differ significantly from those for the nominal orbit in Table 5, as illustrated by comparing Table 9 with Table 4. While the total magnitude is approximately the same, it is now the radial component of the nongravitational acceleration whose magnitude dominates that of the normal component, while the magnitude of the transverse component is again insignificant and poorly defined.

In summary, there is evidence that the strong systematic trends in the residuals in R.A., which necessitated rejection of all observations made between mid-March 1997 and early March 1998 and showed rather prominently in the residuals of the retained observations throughout May 1999, were caused by an excess weight assigned to the 1993 pre-discovery observation. When the weight was reduced by a factor of two, the orbital solution accommodated more than 400 observations that had to be rejected before, increased the scaling distance of the modified nongravitational law by a factor of five, and decreased the magnitude of the normal component of the nongravitational acceleration, so that the radial component now dominates; all this at the expense of a fit to the pre-discovery position, with the total residual increasing from less than $0''.3$ to $\sim 1''$, the estimated uncertainty of the astrometric measurement.

Table 9

Parameters A_1 , A_2 , and A_3 from Solutions MN XXI–MN XXVII

Solution	Nongravitational Parameter (10^{-8} AU day $^{-2}$)		
	A_1	A_2	A_3
MN XXI	$+0.423 \pm 0.043$	-0.0068 ± 0.0032	-0.447 ± 0.023
MN XXII	$+0.470 \pm 0.045$	-0.0064 ± 0.0030	-0.519 ± 0.021
MN XXIII	$+0.498 \pm 0.045$	-0.0056 ± 0.0029	-0.486 ± 0.020
MN XXIV	$+0.520 \pm 0.045$	-0.0047 ± 0.0029	-0.459 ± 0.020
MN XXV	$+0.530 \pm 0.047$	-0.0038 ± 0.0028	-0.445 ± 0.019
MN XXVI	$+0.549 \pm 0.048$	-0.0036 ± 0.0028	-0.443 ± 0.019
MN XXVII	$+0.560 \pm 0.048$	-0.0035 ± 0.0028	-0.423 ± 0.019

6.4. Weight System II: Final Optimization of Orbit

To determine the comet’s nominal orbit and its arrival time from the Oort Cloud under the constraints of Weight System II, we fine-tuned the solution MN XXVII in Table 8. The results are listed in detail as a nominal solution in Table 10, whose format is identical with that of Table 5 to allow direct comparison with the nominal solution with Weight System I. The agreement between the two sets of orbital elements is excellent, but there are major differences in the nongravitational parameters that will be addressed in Section 9. As for the encounter parameters, the time of perijove is now predicted 24 minutes earlier and the Jovicentric distance at perijove is merely 0.05 Jupiter’s equatorial radius, or 3600 km, smaller. An earlier time for the encounter is consistent with a greater scaling distance and a higher value of A_1 , both of which mean that under Weight System II the orbital motion was subjected to higher integrated nongravitational effects, so the temporal gap between the perijove in the year -2251 and the perihelion in 1997 must be slightly longer.

The expressions for the reciprocal semimajor axis of the pre-encounter, original barycentric orbit, $(1/a)_{\text{orig}}$ (or the orbital period P_{orig}), and for the Jovicentric distance at perijove, Δ_J , are similar to Equations (4) and (5), respectively. A dozen solutions, spanning more than 10 hr in the perijove time t_J and listed in Table 11, illustrate the relationships. A least-squares fit to the data points covering less than one hour of the relevant range of t_J provides the following relation:

$$(1/a)_{\text{orig}} = +0.002658 + 0.016180 (t_J - 8^{\text{h}}), \\ \pm 0.000003 \pm 0.000012 \quad (6)$$

where $(1/a)_{\text{orig}}$ and t_J are again in $(\text{AU})^{-1}$ and hr, respectively. We do not show its plot, because it looks very much like Figure 3: the slope is only 2% steeper and the fitted straight line is shifted, as already pointed out, to an earlier time by 25 minutes.

From a wider interval of t_J , spanning about 7.5 hr, the perijove distance (in units of Jupiter’s equatorial radius) is given by an expression:

$$\Delta_J = 10.74861 + 0.139837 (t_J - 8^{\text{h}}) + 0.024681 (t_J - 8^{\text{h}})^2, \\ \pm 0.00004 \pm 0.000021 \quad \pm 0.000006 \quad (7)$$

The minimum perijove distance of 10.551 Jupiter’s equatorial radii took place at 5:10:02, or 160 minutes before the perijove time of C/1995 O1 as an Oort Cloud comet (Table 10).

Table 10

Orbital Elements and Encounter Parameters for Nominal Solution of C/1995 O1 with Weight System II (Equinox J2000)

Orbit at Apparition 1993–2010		
Epoch of osculation (1997 TT)	Mar 13.0	
Time of perihelion (1997 TT)	Apr 1.13785 ± 0.00034	
Argument of perihelion	130°.587793 ± 0°.000070	
Longitude of ascending node	282°.469751 ± 0°.000010	
Orbit inclination	89°.428854 ± 0°.000017	
Perihelion distance (AU)	0.9141677 ± 0.0000019	
Orbit eccentricity	0.99509242 ± 0.00000055	
Orbital period (yr)	{ original ^a	4249.0
	{ osculating	2542.4 ± 1.0
	{ future ^a	2397.8
Longitude of perihelion	101°.8031	
Latitude of perihelion	+49°.4089	
Nongravitational parameters:		
Law applied	modified	
Scaling distance r_0 (AU)	15.363	
Normalization constant Ψ	0.002812	
A_1 [radial] (10^{-8} AU day $^{-2}$)	+0.566 ± 0.047	
A_2 [transverse] (10^{-8} AU day $^{-2}$)	−0.0035 ± 0.0028	
A_3 [normal] (10^{-8} AU day $^{-2}$)	−0.423 ± 0.019	
Solution parameters:		
Mean residual	±0".64	
Time period covered	1993 Apr 27–2010 Dec 4	
Orbital arc (days)	6429.54	
Total observations used	1950	
Critical observations used	15 ^b	
Post-Encounter Orbit in 23rd Century BCE		
Epoch of osculation (−2250 TT)	Dec 8.0	
Time of perihelion (−2250 TT)	Dec 8.0154	
Argument of perihelion	130°.4081	
Longitude of ascending node	282°.3687	
Orbit inclination	89°.0539	
Perihelion distance (AU)	0.907234	
Orbit eccentricity	0.996727	
Orbital period (yr)	{ osculating	4615
	{ future ^a	4249
Longitude of perihelion	101°.26	
Latitude of perihelion	+49°.58	
Pre-Encounter Orbit in 23rd Century BCE		
Epoch of osculation (−2255 TT)	Jan 1.0	
Time of perihelion (−2250 TT)	Oct 11.2060	
Argument of perihelion	340°.1217	
Longitude of ascending node	102°.3535	
Orbit inclination	92°.1802	
Perihelion distance (AU)	0.156469	
Orbit eccentricity	0.999985	
Orbital period (yr)	{ original ^a	~3 200 000
	{ osculating	1 090 000
Longitude of perihelion	103°.14	
Latitude of perihelion	−19°.86	
Encounter Parameters		
Time of perijove (−2251 TT)	Nov 7.32661	
Jovicentric distance at perijove (R_J) ^c	10.73	
Angle Sun–Jupiter–comet at perijove	82°.2	
Jovicentric velocity at perijove (km s $^{-1}$)	28.75	

Notes.^a Derived from the original (or future) semimajor axis referred to the barycenter of the Solar System.^b Of these, one in 1993, six in 2005, five in 2007, and three in 2010.^c $R_J = 71\,492$ km is adopted equatorial radius of Jupiter.

The distribution of residuals from the nominal orbit in Table 10, left by the 1950 observations, is presented in Figure 5. It depicts the ~ 400 reinstated data points between mid-March 1997 and early March 1998 that replace the prominent gap in Figure 4. A residual gap of a few months centered on mid-June 1997 has to do with the comet's persistently small elongations from the Sun (with a minimum of $21^\circ.5$ on June 10), which was responsible for no astrometric data (with one exception) between May 12 and July 14 and made the observations over a few adhering months difficult, less frequent, and of lower quality. The tail of systematically positive residuals (in excess of $1''$) in R.A. in 1998–1999 has likewise disappeared. The strong systematic effect in R.A. in Figure 4 may be slightly overcorrected in Figure 5, but there is no truly worrisome effect of the kind. A greatly improved fit in R.A. to the observations from the denser 1997–1998 cluster, which is apparent by comparing Table 12 with Table 7, corroborates a superior match to the observations by the solution from Table 10. In declination, the distribution of residuals is considered rather satisfactory, with no prominent long-term systematic trends.

Concluding this section, we note that the nominal orbit with Weight System II offers — in terms of orbital quality — a solution superior to the nominal orbit with Weight System I: it accommodates 410 more observations to within $1''.5$, while still fitting the 1993 pre-discovery observation to $\sim 1''$. Both scenarios (Tables 5 and 10) allow for an approach of C/1995 O1 to less than 11 equatorial radii of Jupiter on −2251 November 7, 396 days before perihelion, and, if the comet originated in the Oort Cloud, for its arrival at perijove at times that agree to within one half hour. Moreover, the perijove in both scenarios depends only weakly on the pre-encounter orbit; with Weight System II, for the original orbital periods of 100 000 yr, 10 000 yr, and 1000 yr, the time of perijove would shift forward by merely 1.6, 7.8, and 36.9 minutes and the perijove distance would increase by 0.003, 0.018, and 0.090 Jupiter's equatorial radii, respectively.

Table 11

Correlations Between Time at Perijove, Jovicentric Distance, and Pre-Encounter Original Orbit (Weight System II)

At Perijove on −2251 Nov 7		Pre-Encounter Original Orbit	
Time, t_J (TT)	Jovicentric Distance, ^a $\Delta_J (R_J)$	Reciprocal Semimajor Axis, ^b ($1/a$) _{orig} (AU $^{-1}$)	Orbital Period, P_{orig} (yr)
4:29:23	10.561	−0.054164
5:17:47	10.551	−0.041335
6:25:19	10.589	−0.022999
7:34:51	10.694	−0.004112
7:48:13	10.722	−0.000505
7:49:34	10.725	−0.000139
7:51:04	10.728	+0.000263	235 000
7:55:10	10.738	+0.001365	19 800
8:25:52	10.814	+0.009525	1080
10:44:40	11.322	+0.043756	109
12:49:46	12.000	+0.069360	54.7
14:37:52	12.739	+0.086912	39.0

Notes.^a $R_J = 71\,492$ km is adopted equatorial radius of Jupiter.^b Referred to the barycenter of the Solar System.

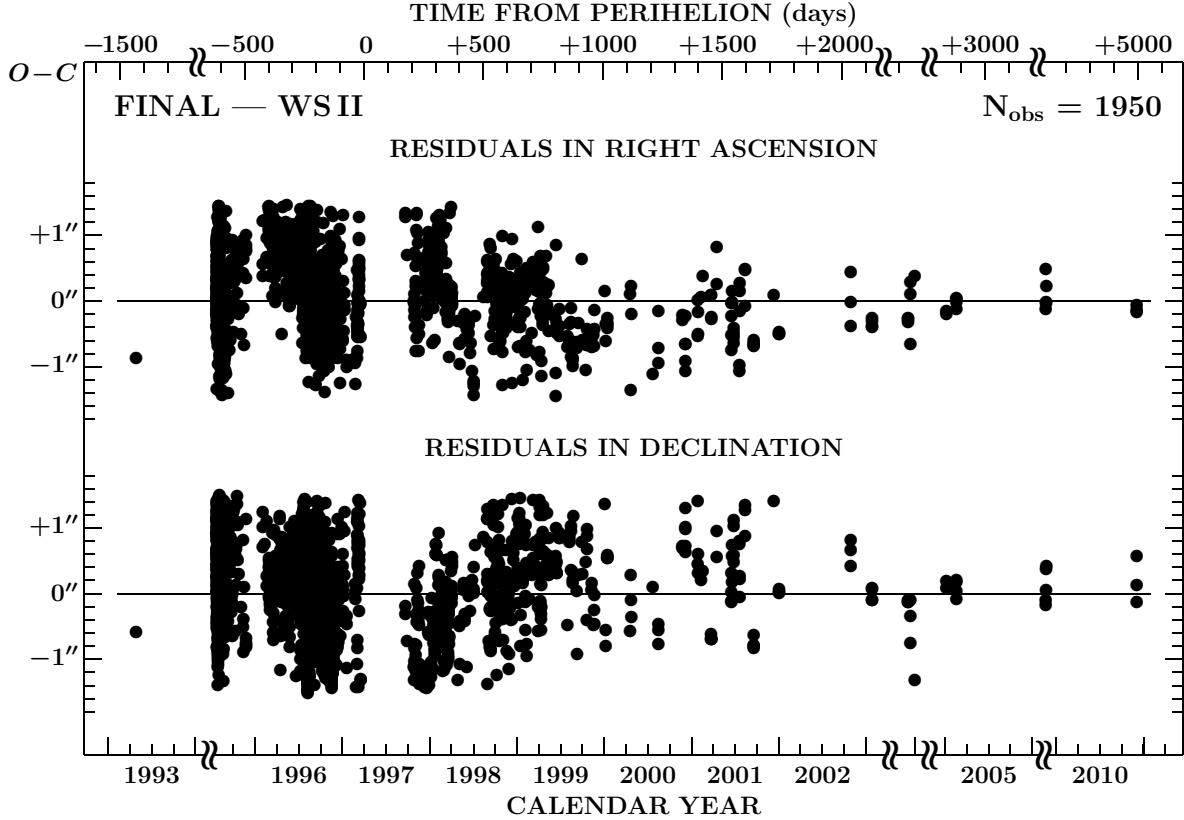


Figure 5. Temporal distribution of residuals $O-C$ (observed minus computed) in right ascension (top) and declination (bottom) from the nominal nongravitational solution listed in Table 10, based on 1950 accurate observations of comet C/1995 O1 between 1993 and 2010, which left residuals not exceeding $1''.5$ in either coordinate. The fit is overall judged to be quite satisfactory, implying for the 1993 pre-discovery observation residuals that reach the limit of its estimated uncertainty.

Table 12

Residuals, from Nominal Orbit with Weight System II, of Sample Observations from Table 7 (Sparse Cluster vs Dense Cluster) for Comparison with Residuals from Nominal Orbit with Weight System I

Time of Observation ^a (UT)	Residual $O-C$		Obs. Site Code	Image Scale (mm^{-1})	Reference MPC	Time of Observation (UT)	Residual $O-C$		Obs. Site Code	Image Scale (mm^{-1})	Reference MPC
	R.A.	Decl.					R.A.	Decl.			
1998 May 8.96560*	-2''.48	+0''.67	834	131''	32 129	1998 May 6.96538	-0''.63	-0''.44	844	90''	31 853
July 4.82718	-1.40	+0.40	422	201	32 129	28.39198	-0.56	-0.41	422	201	31 853
Aug 29.35072*	-1.59	-0.27	834	131	32 379	June 14.35473	-0.47	+0.15	422	201	32 129
Nov 1.14909	-1.25	+0.66	844	90	32 821	21.91409	-0.61	+0.01	834	131	32 129
Dec 12.30799	-1.22	+0.79	808	55	33 415	Sept 26.24039	-0.69	+1.20	844	90	32 821
1999 Jan 26.03839	-1.19	+0.14	834	131	34 676	Nov 4.28320	-0.46	-0.71	834	131	33 415
Feb 1.12505*	-0.71	+1.54	834	131	34 676	1999 Jan 4.49222	-0.08	+0.92	422	201	33 415
4.03494	-0.68	+0.76	834	131	34 676	15.44743*	-0.02	+1.81	422	201	33 616
28.11036*	-1.53	+0.98	834	131	35 767	Feb 8.07250	+0.20	+0.36	834	131	35 767
Mar 5.02648	-1.32	+1.36	834	131	35 767	Mar 22.06831	+0.19	+0.41	834	131	35 767
26.08788*	-1.50	+1.53	844	90	34 092	Apr 7.08498	+0.26	+1.18	844	90	34 387
Apr 13.97924	-1.12	+0.11	834	131	35 767	May 3.40045	+0.14	+0.55	426	208	34 387

Note.

^a Observations marked with asterisks were rejected because a residual in at least one coordinate exceeds the rejection cutoff of $1''.5$.

As illustrated in Figure 6, the comet was approaching Jupiter from above the ecliptic plane and was diverted by the planet's gravity back above the ecliptic plane in a trajectory that was strongly hyperbolic relative to Jupiter, with an eccentricity of 4.0. The comet was launched toward the Sun along a new, very different orbit, whose plane though agreed with the original one to 3° . At the time of encounter the comet's position was at close proximity of the descending node of the original orbit and the

ascending node of the new orbit. After reaching perihelion about two months later and at a distance from the Sun six times greater than it would have in the absence of the encounter, the comet began to recede from the Sun, once again approaching the ecliptical plane. Some 35 days after perihelion it crossed the descending node (now on the other side of the Sun) for the second time and continued its journey to aphelion, diving almost perpendicularly to the ecliptic.

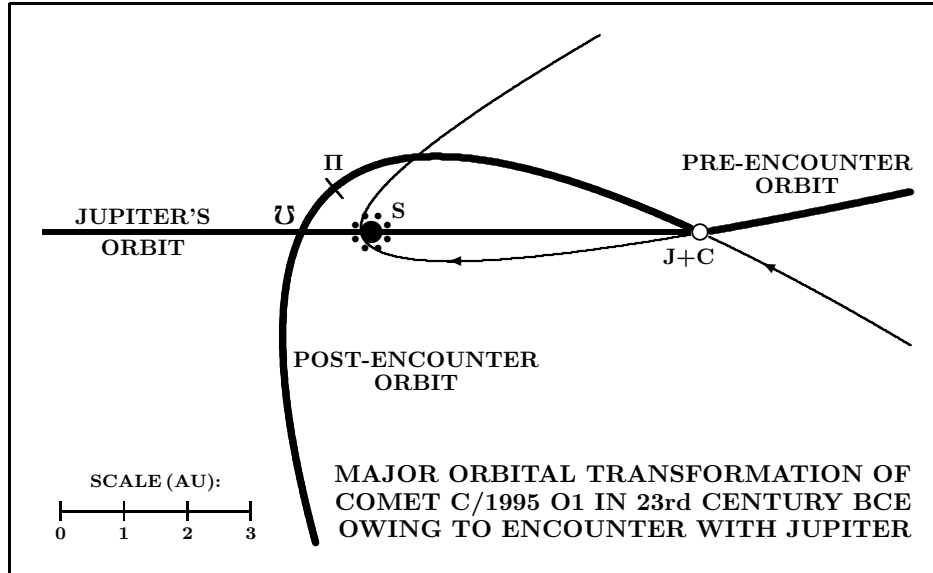


Figure 6. Major orbital transformation of C/1995 O1 on –2251 November 7, at the time of its close encounter with Jupiter, in projection onto the comet’s orbital plane, which was nearly exactly perpendicular to Jupiter’s orbital plane. The comet’s actual path is depicted by the thin curve, the extrapolated portions of the pre-encounter and post-encounter orbits by the thick curve, with the scale and direction of motion indicated. The Sun is marked by S, Jupiter and the comet at the time of encounter by J+C, the comet’s perihelion point by II, and its second descending node, on the post-encounter orbit, by U. The first descending node, on the pre-encounter orbit, and the ascending node on the post-encounter orbit coincide on the scale of the plot with the comet’s and Jupiter’s position at the time of encounter.

7. PREDICTED APPEARANCE OF COMET C/1995 O1 IN THE 23RD CENTURY BCE AND SEARCH FOR POSSIBLE HISTORICAL RECORDS

Searching for historical records would be pointless, if the comet’s appearance was affected by unfavorable observing geometry. While the viewing conditions for a comet moving in an orbit perpendicular to the plane of the ecliptic cannot remain inferior for long, we are primarily concerned with a short orbital arc near perihelion, when the comet is intrinsically the brightest. Given the perihelion distance near 0.9 AU and the argument of perihelion at 130° , the comet would at perihelion project to the terrestrial observer at an angular distance of less than 24° from the Sun (at a geocentric distance of more than 1.7 AU), if the Earth should then be crossing the comet’s orbital plane on the side of the ascending node. On the other hand, at the descending node, at a heliocentric distance of 1.1 AU, the comet would be, under the most favorable conditions, at opposition with the Sun and only 0.1 AU from the Earth.

An ephemeris, based on the post-encounter orbital elements from the 23rd century BCE in Table 10, shows that the viewing circumstances in this configuration were rather favorable. In Figure 7 we present the comet’s predicted path in the sky over a period of 4 months, from –2250 October 23 (46 days before perihelion, position 1) through –2249 February 20 (74 days after perihelion, position 13). This time interval was dictated by the comet’s predicted brightness. Assuming, conservatively, that in the 23rd century BCE the comet was as bright intrinsically as in the 1997 apparition, we calculated its apparent brightness from the light-curve fits published by Kidger (1999). Over the orbital arc in Figure 7 the comet was predicted to have remained brighter than apparent magnitude +2, reaching a peak magnitude of –1.9, rivaling Jupiter, near position 7, about two weeks past perihelion

and shortly after entering the constellation Andromeda. As seen with the naked eye near perihelion, the coma was predicted to have amounted to $32'$ in diameter, practically the angular size of the Moon.⁴

The predicted viewing geometry is described in a self-explanatory Table 13. A minimum geocentric distance of 0.644 AU was found to have taken place on –2250 December 23, while the elongation reached a minimum of $41^\circ.2$ on –2250 October 16 and a maximum of $71^\circ.8$ on –2249 January 9. The phase angle reached a peak of $74^\circ.5$ on –2250 December 19, so no forward-scattering effect could be expected. The comet was predicted to have stayed brighter than magnitude 0 for 67 days and brighter than magnitude –1 for 40 days.

We conclude that in this scenario the comet must have been a spectacular object quite favorably placed in the sky to the northern-hemisphere observer for a long enough period of time that it could not have been overlooked. Nonetheless, the probability that the comet’s apparition was recorded is low, because historical records of comets from this very distant past are extremely fragmentary. Even if it was, we probably would not be able to recognize it because of uncertainties in dating the celestial phenomena at these times.

It is accepted that reliably determined times of events in Chinese historical records extend to only about –840. Information from earlier times is vague and sporadic, because there are no contemporaneous sources; all known events from the early period were compiled from sources dated after –770 (such as *Chūnqiū* or *Ch’un-ch’iu*, the *Spring and Autumn Annals*; e.g., Liu et al. 2003).

⁴ This prediction is based on 433 naked-eye estimates of the coma diameter of C/1995 O1 made in 1997 between 10 days before and 10 days after perihelion, and reported to the *International Comet Quarterly* (Green 1997, 1998, 1999). The data average, a diameter of 1 150 000 km, was equivalent to $19'.6$ at the 1997 perihelion.

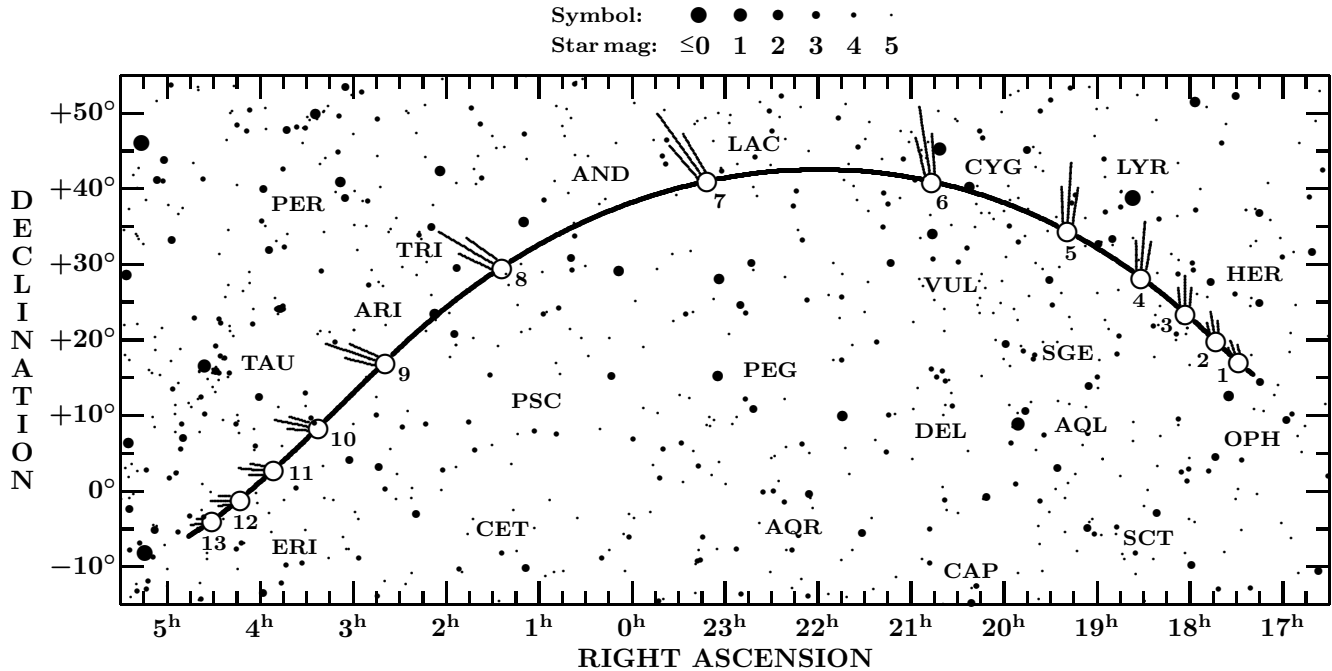


Figure 7. Predicted path of comet C/1995 O1 over the sky during its arrival from the Oort Cloud in the year -2250 . The 13 positions are for times between -2250 October 23 and -2249 February 20, spaced at 10 days intervals. The numbers 1–13 refer to the entries in Table 13. The tail’s orientation shows the antisolar direction, while its length measures approximately the comet’s apparent brightness, which varied from $+1.8$ at position 1 to -1.9 at position 7, back to $+2.0$ at position 13. The equinox is J2000.

Equally or more uncertain are the time assignments for events in other ancient civilizations. In particular, the currently accepted chronology of the Egyptian history, introduced less than two decades ago (Shaw 2000), differs in the 3rd millennium BCE from a previous chronology (Breasted 1906) by almost 300 yr. It thus comes as no surprise that most modern catalogs of historical records of comets, summarizing information collected from the ancient sources, do not reach the 3rd millennium BCE, and they especially do not list the orbital elements. Indeed, Williams (1871) begins in the year -610 , Galle (1894) in -371 , Baldet & de Obaldia (1952) and Vsekhsyatsky (1958) in -466 (presumably 1P/Halley), Porter (1961) and Marsden & Williams (2008) in -239 (undoubtedly 1P/Halley), Ho (1962) in the 14th century BCE, and Kronk (1999) in -674 . Only Baldet’s (1950) *liste générale* and Pingré’s (1783) *cométographie* (one of Baldet’s sources) start, respectively, in the 24th and 23rd centuries BCE. Pingré’s, Williams’, Baldet’s, and Ho’s lists and many additional sources were incorporated by Hasegawa (1980) into his catalogue of ancient and naked-eye comets, but with some notes and comments left out.

A reference to C/1995 O1 in -2250 could potentially be one of the first six entries common to Baldet’s (1950) and Hasegawa’s (1980) lists: -2315 , -2296 (or -2284), -2287 , -2254 , -2241 (or -2269 or $-2226/5$), and -2191 (or -2024). The origin of the first five is Chinese, while the last record is from Egypt. The objects from the years -2315 , -2287 , and -2254 are listed by Baldet in reference to Stratton (1928), whose subject was the records of novae. However, our inspection of Stratton’s paper fails to confirm Baldet’s objects of -2315 and -2287 in the constellation Crater. Stratton does indeed point at the encyclopedia *T’u shu chi ch’-êng* as the source of the

earliest record of a bright object in the sky, but the year is identified as -2678 , not -2315 . Furthermore, we note Stratton’s remark on the star of -2254 in Scorpius, but also his reference to a yellow star in -2237 , which Baldet omits. Stratton regards both objects as likely novae.

The events of -2296 (etc.), -2241 (etc.), and -2191 (etc.) were copied by both Baldet (1950) and Hasegawa (1980) from Pingré (1783), who provides a fair amount of detail. He explains that the first of the three events was related to the birth of Emperor Yu the Great, the first ruler of the Xia Dynasty. But Yu’s historical existence

Table 13
Circumstances at Arrival of C/1995 O1 to Perihelion in -2250

Entry No.	Date (TT)	From Perih. ^a (days)	Distance (AU)		Phase Angle	Elon-gation	App. Vis. Mag
			Earth	Sun			
1	-2250 Oct 23.0	-46.0	1.757	1.214	$32^{\circ}9$	$41^{\circ}7$	1.8
2	Nov 2.0	-36.0	1.585	1.109	37.8	43.8	1.2
3	12.0	-26.0	1.385	1.019	45.1	47.3	0.2
4	22.0	-16.0	1.164	0.952	54.2	51.8	-0.5
5	Dec 2.0	-6.0	0.939	0.914	64.1	56.7	-1.2
6	12.0	$+4.0$	0.745	0.910	72.2	61.7	-1.7
7	22.0	$+14.0$	0.646	0.941	74.2	66.7	-1.9
8	-2249 Jan 1.0	$+24.0$	0.696	1.003	68.4	70.7	-1.6
9	11.0	$+34.0$	0.868	1.089	59.6	71.4	-0.8
10	21.0	$+44.0$	1.095	1.191	51.3	69.4	0.0
11	31.0	$+54.0$	1.340	1.305	44.3	66.0	0.8
12	Feb 10.0	$+64.0$	1.584	1.425	38.4	62.2	1.4
13	20.0	$+74.0$	1.821	1.549	33.4	58.3	2.0

Note.

^a Time from perihelion: minus sign means before perihelion, plus sign after perihelion.

has been a matter of controversy, because the time of his presumed reign preceded the oldest known written documents by about a millennium. Doubts have also persisted on the subject of an elaborate irrigation system that Yu as the ruler is believed to have overseen to control floods that for generations had inundated the vast plains of the country along the Yellow River. Pingré (1783) adopted that the reign of Yu began in -2223 and that he died at the age of 100 in -2196 or -2184 . Then the star, which is said to have appeared as an omen of good fortune during his mother’s pregnancy, would have lit up in the sky in -2296 or -2284 . The modern interpretation of the historical records places the beginning of the Xia Dynasty to about -2070 ,⁵ which would mean that the date listed by Pingré is too early by some 150 yr.⁶ Moreover, Pang & Yau (1996) argue that a statement in the *Bamboo Annals* that during Yu’s reign “... the Sun disappeared by day and reappeared at night ...” is a reference to a “double sunset” eclipse of the Sun on -1911 September 24. This timing is in excellent agreement with the result from a very recent discovery by Wu et al. (2016) of a catastrophic-flood event that was caused by breaching a natural dam created by an earthquake-driven landslide, all of which has by radiocarbon dating been pegged to around -1920 , the time that is expected to correlate with the beginning of Yu’s reign. It is thus likely that Pingré’s time for the bright star associated with Yu’s birth was at least 300 yr too early and could not refer to C/1995 O1.

The event of -2241 (etc.) happened during the reign of Emperor Shun, who was Yu’s predecessor. Referring to Father Couplet (see footnote 6), Pingré says that a new star, equaling a half Moon, was seen in -2241 , the 16th year of Shun’s reign. However, based on independent sources for the date of Shun’s ascension to the throne, Pingré also finds as possible the years -2269 or $-2226/5$. Given the shift of Pingré’s time frame, the event probably occurred in the 20th century BCE and, likewise, could not be considered a reference to C/1995 O1.

There is hardly any point in commenting on the event of -2191 (or -2024), not only because it is even more recent, but also because Pingré expresses so much skepticism about this case that one wonders why he bothered to include it in his cometography in the first place.

The only remaining object that as yet has not been discredited, is Stratton’s (1928) yellow star of -2237 . There appears to be no additional information available, but the time-frame contraction mentioned above is probably also applicable in this case, even if Stratton should be incorrect in his belief that this was a nova. The inevitable conclusion is that any effort to identify a historical record with C/1995 O1 is doomed to failure.

⁵ This date for the beginning of the Xia Dynasty was fixed by the *Xia-Shang-Zhou Chronology Project*, a multi-disciplinary project commissioned by the People’s Republic of China in 1996 to determine with accuracy the location and time frame of the Xia, Shang, and Zhou Dynasties. This Project provides dates that are generally later than given by the numerous variations of the traditional historiography, based mainly on the work by Sima Qian (died -85), the legendary historian of the Han Dynasty; for more details, see e.g. https://en.wikipedia.org/wiki/Xia-Shang-Zhou_Chronology_Project.

⁶ To set a frame for dating records of comets, Pingré often refers to major historical events (e.g., the death of emperors), for whose timing he usually relies on information from secondary sources, such as the works of the French Jesuits A. Gaubil (1689-1759) or J.-A.-M. de Moyriac de Mailla (1669-1748), or the Belgian Jesuit P. Couplet (1623-1693), all of whom were missionaries to China.

8. PREDICTED MOTION OF C/1995 O1 OVER SEVERAL FUTURE REVOLUTIONS ABOUT THE SUN

The constraint that C/1995 O1 had a close encounter with Jupiter and was a dynamically new comet in the previous return to the Sun fixes the comet’s motion over more than one full revolution about the Sun. With this wide enough base as an initial condition, it is plausible to investigate the comet’s expected orbital evolution over a limited number of future returns to perihelion. This limit is determined by the rate of error propagation in the orbital elements, which is in this case a function of the semimajor axis of the comet’s pre-encounter, original barycentric orbit. By prescribing an (unknown) error to the value of $(1/a)_{\text{orig}}$, we can estimate the propagated errors in the elements, which, as shown below, increase in general with time (or with the number of returns) exponentially. The most sensitive element is by far the perihelion time, to which we pay particular attention.

For the purpose of determining the rate of error propagation, we began the orbit integration forward in time from the osculating orbit in 1997 listed in Table 10, which was assumed to be independent of the error in $(1/a)_{\text{orig}}$. [It should be the comet’s post-encounter orbit in -2250 as well as the time and distance at perijove that would change slightly, if $(1/a)_{\text{orig}}$ differed from the adopted value of $+0.000046 \text{ AU}^{-1}$ (Section 6.2).] The results of the computations are shown in Figure 8, which suggests

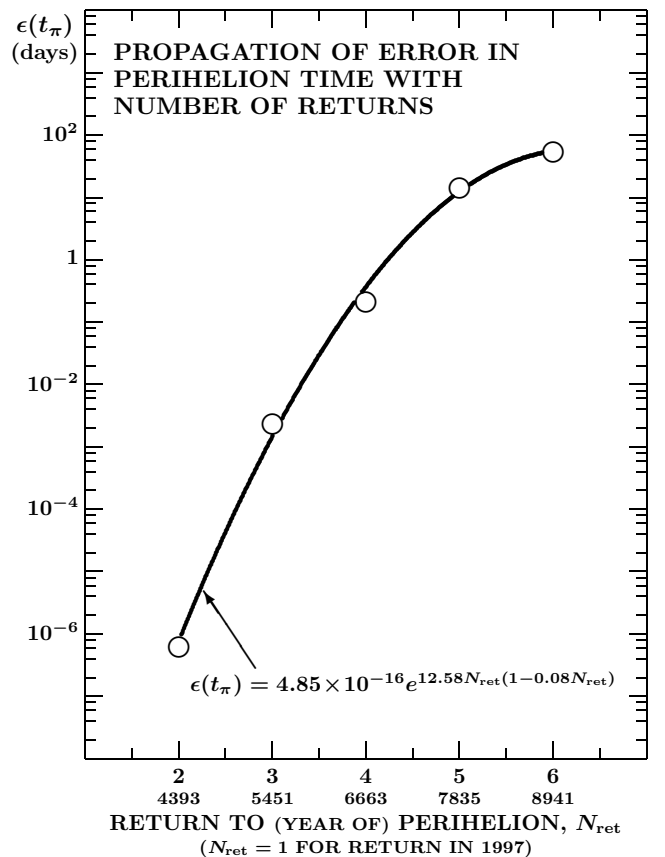


Figure 8. Propagation of the error in the perihelion time, equivalent to an error of 0.000001 AU^{-1} , as a function of time, expressed in terms of a number returns to perihelion, N_{ret} , since -2250 . The empirical fit is the best we were able to achieve in the given range of returns and is not to be extrapolated outside this range.

Table 14
 Predicted Long-Term Orbital Evolution of Comet C/1995 O1 with Weight System II (Equinox J2000)

Orbital/Encounter Parameter	Initial Arrival	1st Return	2nd Return	3rd Return	4th Return
Epoch of osculation (TT)	−2250 Dec 8.0	1997 Mar 13.0	4393 Aug 6.0	5451 May 27.0	6663 July 26.0
Time of perihelion (TT)	−2250 Dec 8.0154	1997 Apr 1.1379	4393 Aug 6.7981	5451 May 27.0043	6663 July 26.0621
Argument of perihelion	130°.4081	130°.5878	131°.0061	130°.8987	130°.8571
Longitude of ascending node	282°.3687	282°.4698	282°.4963	282°.5688	282°.7443
Orbit inclination	89°.0539	89°.4289	90°.4537	90°.2601	90°.3011
Perihelion distance (AU)	0.907234	0.914168	0.915306	0.919657	0.918314
Orbit eccentricity	0.996727	0.995092	0.991429	0.992210	0.992211
Orbital period (yr)	4615	2542	1104	1283	1280
Longitude of perihelion	101°.26	101°.80	103°.02	102°.87	103°.09
Latitude of perihelion	+49°.58	+49°.41	+48°.99	+49°.10	+49°.14
Encounter Parameters:					
Time of perijove (TT)	−2251 Nov 7.327	1996 Apr 5.064	4392 Jul 21.123	5449 May 30.70 ^a	6663 Oct 3.33 ^b
Jovicentric distance at perijove (AU)	0.00513	0.771	0.428	4.54	3.85
Jovicentric velocity at perijove (km s ^{−1})	28.75	23.90	23.04	14.54	36.90

Notes.

^a There was another distant approach to Jupiter, to 4.84 AU, shortly after perihelion.

^b This was a post-perihelion approach; there was no pre-perihelion approach to Jupiter within 9 AU.

that an error of 0.000001 AU^{-1} transforms to a negligibly small error of 0.05 second in the perihelion time at the next return, to which we assign $N_{\text{ret}} = 2$. However, at the following return ($N_{\text{ret}} = 3$), the propagated error already increases to 3.4 minutes and at the subsequent returns to, respectively, 0.21 day ($N_{\text{ret}} = 4$), 14.4 days ($N_{\text{ret}} = 5$), and 53.1 days ($N_{\text{ret}} = 6$). We terminated the computations at this point, because given that a realistic uncertainty of $(1/a)_{\text{orig}}$ of C/1995 O1, even if it was a dynamically new comet, should be at least 0.000010 AU^{-1} and perhaps still greater, the corresponding uncertainty of the perihelion time at the subsequent returns could become comparable with Jupiter’s orbital period, rendering the comet’s encounters with the planet (and the resulting orbital transformations) unpredictable.

The complete sets of orbital elements with Weight System II, including the initial arrival and the current return (both from Table 10) are presented in Table 14, in which the future returns are terminated in the 7th millennium. To our surprise, the table shows that as long as the comet experienced the very close approach to Jupiter in −2251, it undergoes encounters to less than 1 AU from the planet at *three consecutive* apparitions: a moderate approach in 1996 will be followed by a yet another preperihelion encounter at the next return, in the year 4392!

For the scenario based on Weight System I, the results are rather similar for the expected return in 4393, the perihelion time taking place about 24 days earlier and the Jovicentric distance at perijove amounting to 0.58 AU, but the predictions by the two scenarios of the next perihelion time, in the 6th millennium, already differ by more than 200 yr. Yet, the fundamental features of the orbital evolution, especially the triple Jovian encounter at three consecutive returns, are common to both scenarios and thus independent of the weight system for the critical observations.

In a recent paper (Sekanina & Kracht 2016), we called attention to the fact that Jovian perturbations exerted on a comet in the course of recurring close or moderate encounters, especially when they take place at several consecutive returns (in a scenario that we described as a

high-order orbital-cascade resonance), can provoke rapid inward drifting of the comet’s aphelion. In magnitude, these effects rival those triggered by a single extremely close encounter. When we wrote that 2016 paper, we did not expect that C/1995 O1 — then the next object of our interest — would provide us with such a nice example of the process of orbital-cascade resonance, ending up with an aphelion distance of ~ 200 AU after only three revolutions about the Sun.

Table 15 presents the details of this remarkable orbital evolution: from the perihelion times in column 2 we determined the anomalistic orbital periods in column 3, which between −2250 and 1997 and between 1997 and 4393 turned out to be, as column 4 shows, practically commensurable with the sidereal orbital period of Jupiter (as the minor deviations in column 5 confirm); column 6 converts the orbital periods from column 3 into the reciprocal values, $1/a$, of the semimajor axis, while the last column lists the differences between the neighboring values of $1/a$, that is, the perturbations integrated over one revolution about the Sun. The table shows that in merely three revolutions about the Sun, by 5451, the comet will reduce its orbital period from some 3 million yr to only slightly more than 1000 yr. An equally surprising result

Table 15
 Rapid Inward Drifting of Aphelion of C/1995 O1 Driven by High-Order Orbital Resonance (Weight System II)

Re- turn	Time of Perihelion Passage (TT)	Anom. Orbital Period (yr)	High- Order Reso- nance	Devi- ation	Reciprocal Semimajor Axis (AU ^{−1})	Integrated Pertur- bation (AU ^{−1})
...	(Oort Cloud)					
0	−2250 Dec 8	(3.2×10^6)	+0.000046	+0.003768
1	1997 Apr 1	4246.313	1:358	−0.018	+0.003814	+0.001770
2	4393 Aug 6	2396.350	1:202	+0.022	+0.005584	+0.004048
3	5451 May 27	1057.803	1:89	+0.177	+0.009632	−0.000836
4	6663 July 26	1212.165	1:102	+0.191	+0.008796	+0.000201
5	7835 June 1	1171.850	1:99	−0.208	+0.008997	+0.000353
6	8941 June 6	1106.013	1:93	+0.242	+0.009350	

is that the peak integrated perturbation is not the one associated with the close approach of 0.005 AU to the planet in -2251 , but with an encounter to 0.43 AU in 4392! The effect of the Jovian encounters is illustrated by an average integrated perturbation of $1/a$: between -2250 and 5451 it amounts to about $0.0032 \text{ AU}^{-1}\text{rev}^{-1}$, being very systematic and always positive; whereas during the three revolutions after 5451 it equals, in absolute value, only $0.00046 \text{ AU}^{-1}\text{rev}^{-1}$ and is random.

9. CORRELATION AMONG NONGRAVITATIONAL LAW, ORBITAL HISTORY, AND ACTIVITY OF COMET C/1995 O1

In Section 6.4 we expressed our preference for the orbital solution in Table 10 (Weight System II) over the solution from Table 5 (Weight System I) solely on the grounds of orbital quality (the distribution of residuals) and the number of accommodated observations. We noticed that by far the most striking distinction between the parameters of the two solutions was the nongravitational law. The solution from Table 5 required a scaling distance of $r_0 = 3.07 \text{ AU}$, implying the prevalence of water ice in the effects of the nongravitational acceleration, and, unexpectedly, the dominance of the acceleration's normal component over the radial component. On the other hand, the preferred solution from Table 10 is in line with a scaling distance of more than 15 AU , suggesting that the contribution to the detected nongravitational acceleration by ices much more volatile than water ice was important. In addition, the radial component of the nongravitational acceleration exceeded the normal component, even though by a factor of $\sim 4/3$ only. The transverse component came out to be small and poorly determined from both solutions.

In Section 6 we already remarked on a sizable body of data that points to a large abundance of highly-volatile species sublimating from the nucleus of C/1995 O1. The question is to what extent is the nongravitational law, preferred for its orbital prerogatives, consistent with evidence based on the physical observations. Because of a record post-perihelion span of available data, extending to 32 AU from the Sun, it is this branch of the orbit that we examine first.

9.1. Nongravitational Law and Major Contributors to the Comet's Post-Perihelion Activity

Our aim is now twofold: (i) to compare the two applied versions of the nongravitational law (Weight Systems I and II) with the sublimation curves of common ices released from the nucleus and (ii) to examine the correlations between the laws and the observed production rates of these species. To proceed with the first task, we describe the sublimation curves of three major compounds: water ice, carbon dioxide, and carbon monoxide in the order of increasing volatility.

The isothermal approximation to the nongravitational (or sublimation) law for water ice, extensively tested on the orbital motions of a large number of comets, is taken from Marsden et al.'s (1973) standard Style II nongravitational model, as already mentioned in Section 4. For carbon dioxide the critical data on the saturated vapor pressure and the latent heat of sublimation were taken from Azreg-Aïnou (2005), whereas for carbon monoxide from an extensive compilation by Wylie (1958).

The parameters of an empirical fit, of the type expressed by Equation (1), to the normalized sublimation (or momentum-transfer) rates of the three species are listed in Table 16, together with the latent heat of sublimation and the ice temperature and sublimation rate at 1 AU from the Sun. These rates, per cm^2 per s, are, respectively for carbon monoxide and carbon dioxide, 8.5 times and 2.3 times greater than for water ice. Masswise the ratios are still higher: 13.2 for carbon monoxide and 5.6 for carbon dioxide. An approximation to the scaling distance given by Equation (3) provides the values of 114.5 AU for carbon monoxide and 8.9 AU for carbon dioxide, in reasonable agreement with the tabulated numbers obtained by fitting the sublimation rates derived directly from the relations for vapor pressure as a function of temperature.

To proceed with the second task, we next collected the data on the production rates of water, carbon dioxide, and carbon monoxide from the nucleus of C/1995 O1 after perihelion. For water ice the production rates were determined by Dello Ruso et al. (2000) directly from the ground-based high-resolution $2\text{--}5 \mu\text{m}$ infrared spectroscopic observations and by Crovisier et al. (1999) from observations with two instruments on board the *Infrared Space Observatory* (ISO); and, furthermore, by Combi et al. (2000) from the images of the hydrogen Lyman-alpha coma taken with the SWAN all-sky camera on board the SOHO spacecraft; by Weaver et al. (1999b) via OH production rates from ultraviolet observations with the Hubble Space Telescope (HST); by Stern et al. (1999) and Harris et al. (2002), both groups using in principle the same technique to analyze their observations taken, respectively, with a mid-UV/visible imager on board the Space Shuttle and with a wide-field ground-based instrument; and by Biver et al. (1999, 2002) and Colom et al. (1999), who employed a radio telescope to obtain measurements of the 18-cm emission of OH.

Since the radiation from carbon dioxide cannot be observed from the ground (e.g., Crovisier 1999), the only existing post-perihelion data on its production rate were derived from the ISO observations of the 4.25-micron band (Crovisier et al. 1999).

Table 16

Comparison of Isothermal Approximations to Sublimation Laws for Carbon Monoxide, Carbon Dioxide, and Water Ice^a

Parameter of Sublimation Law	Carbon Monoxide	Carbon Dioxide	Water Ice
Scaling distance r_0 (AU)	107.60	10.10	2.808
Exponent m	2.056	2.038	2.150
Exponent n	5.060	4.573	5.093
Product of exponents nk	24.764	25.828	23.5
Normalization coefficient Ψ	$10^{-4.177}$	$10^{-2.047}$	$10^{-0.954}$
Latent heat of sublimation (cal mol ⁻¹)	1785	6400 ^b	11 400
Temperature of ice at 1 AU from Sun (K)	39.4	111.1	194.7
Sublimation rate at 1 AU from Sun (cm ⁻² s ⁻¹)	$10^{18.42}$	$10^{17.85}$	$10^{17.49}$

Notes.

^a For assumed Bond albedo of 0.04 and unit emissivity.

^b Average over temperature range of 60 K to 160 K.

For carbon monoxide our primary source of information was the paper by Gunnarsson et al. (2003), specifically the sum of the production rates from their model of the nucleus’ subsolar and isotropic outgassing, with the data taken at a wavelength of 1.3 mm at ESO, La Silla. They cover a range of heliocentric distances from 2.87 AU to 10.75 AU. This set was supplemented with the results from the radio observations by Biver et al. (1999, 2002) at several discrete wavelengths between 0.65 mm and 2.6 mm; from the infrared observations by DiSanti et al. (1999); and from the ISO infrared observations by Crovisier et al. (1999). From the common data points by Gunnarsson et al. (2003) and Biver et al. (1999, 2002) we found that the latter required a minor correction of -0.05 in $\log(\text{production rate})$ to match the former on the average. In accordance with the conclusions by DiSanti et al. (1999) we plotted the “native” production rates at heliocentric distances smaller than 2 AU, but the “total” rates at larger distances.

The production of carbon monoxide was systematically monitored up to 14 AU from the Sun. The activity at still larger distances could only be assessed from the magnitudes of the dust present in the coma. As shown in Table 17, for the period from mid-1999 to late 2007 we derived these data from the total magnitudes reported to the *Minor Planet Center* (see footnote 1 in Section 2) by the observers from the selected sites; for the period from late 2007 on from the magnitudes published by Szabó et al. (2008, 2011, 2012). Each resulting magnitude $(H_{\Delta})_{\text{corr}}$ was obtained by normalizing the observed magnitude to a unit geocentric distance, by subtracting

the contribution from the nucleus, and by referring the residual brightness to a zero phase angle using the “compound” Henyey-Greenstein law, as modified by Marcus (2007). Table 17 indicates that in 2007 the comet, at 25.8 AU from the Sun, was definitely active (Szabó et al. 2008), but by 2009, at 28 AU from the Sun, the nucleus became inert (Szabó et al. 2012). This development is also supported by the Spitzer Space Telescope thermal-infrared observations made in 2005 and 2008 by Kramer et al. (2014). As the comet’s heliocentric distance between the two dates increased from 21.6 AU to 27.2 AU, the flux dropped much more steeply than required by an inverse square power law, with the dust in the coma having been substantially depleted over the period of the three years.

The collected data on the comet’s post-perihelion activity in Figure 9 show a number of important features. Comparison of the two modified nongravitational laws with the sublimation curves for water ice, carbon dioxide, and carbon monoxide — all normalized to 1 AU — suggests that, the law with Weight System I is, as expected, very close to the water-ice sublimation curve, while the law with Weight System II extends to larger heliocentric distances than the carbon-dioxide sublimation curve. Thus, no mix of H_2O and CO_2 could explain the law with Weight System II; a contribution from CO is necessary.

The water-production rates are consistent with the theoretical water-ice sublimation curve up to about 2.5 AU from the Sun. Beyond that point only two positive observations exist, which suggest that the rate decrease proceeded more slowly than predicted by the simple theory.

Only two measurements exist in the post-perihelion period of time for the production rate of carbon dioxide (obtained with the ISO); they are fairly compatible with an expected $\sim r^{-2}$ sublimation curve between 3.5 AU and 5 AU from the Sun. At 3.89 AU, the production rates of H_2O and CO_2 were comparable, about $3 \times 10^{28} \text{ s}^{-1}$, but masswise the rate of CO_2 was more than twice greater.

The production rate of carbon monoxide follows the approximately inverse-square power law from perihelion all the way to 14 AU. Among more than 40 collected measurements only one is strongly out of line; it is the second (and last) post-perihelion measurement obtained with the ISO on 1998 April 6 at 4.9 AU from the Sun. In Figure 9 this anomalous rate exceeds the level of the nucleus outgassing rate from 1998 March 18–19 (at 4.7 AU from the Sun), as determined by Gunnarsson et al. (2003), by a factor of 8. Crovisier et al. (1999) speculated on a possible outburst, but related that no simultaneous flare-up was reported in the light curve. We may add that no excessive production of CO_2 is seen in the plot to have accompanied the CO event either.

The normalized magnitudes $(H_{\Delta})_{\text{corr}}$ of the dust coma are drawn to overlap the CO production rates in Figure 9 in the range of heliocentric distances from 8.7 AU through ~ 14 AU. A satisfactory correlation between both appears from the plot, suggesting that $(H_{\Delta})_{\text{corr}} = 10$ is equivalent to $Q_{\text{CO}} \simeq 1.6 \times 10^{27} \text{ s}^{-1}$, even though a correspondence between magnitudes and any other activity index is only approximate because of the dust ejecta’s finite residence time in the coma. The magnitudes begin to progressively deviate from the inverse-square power

Table 17

Normalized Magnitudes for Dust Coma of C/1995 O1 Between Mid-1999 and 2011 ($r > 8.5$ AU post-perihelion)

Observation Time (UT)	Distance to Sun (AU)	Phase Angle	Magnitude $(H_{\Delta})_{\text{corr}}$	Code ^a or Reference
1999 June 28.3	8.750	6 ^o 7	7.83	467
Nov 10.5	9.763	5.8	8.39	474
12.7	9.778	5.7	8.18	474
2000 Mar 2.5	10.573	5.3	8.78	474
7.4	10.607	5.3	8.74	474
July 30.5	11.605	5.0	8.66	474
Nov 23.6	12.376	4.5	9.19	428
Dec 22.5	12.564	4.4	8.84	428
2001 July 22.8	13.907	4.2	11.64	474
Dec 17.5	14.806	3.7	10.10	428
2002 Jan 3.6	14.908	3.6	11.31	413
May 8.4	15.645	3.7	11.55	422
Oct 30.5	16.651	3.4	12.00	422
2003 Jan 27.1	17.148	3.2	12.94	809
Dec 25.5	18.955	2.8	13.28	422
2005 Jan 8.1	20.918	2.5	13.58	304
2007 Oct 20.7	25.766	2.2	13.51	413
21.2	25.769	2.2	13.73	Szabó ^b
2009 Mar 8	28.003	2.0	>19	Szabó ^{b,c}
2010 Dec 4.3	30.698	1.7	>17	Szabó ^b
2011 Oct 23.6	32.019	1.8	>18	Szabó ^b

Notes.

^a See <http://www.minorplanetcenter.net/iau/lists/ObsCodesF.html>.

^b Reference: Szabó et al. (2012).

^c In Table 1 of Szabó et al. (2012), the date 2009 Sep 08 for this entry should read 2009 Mar 08.

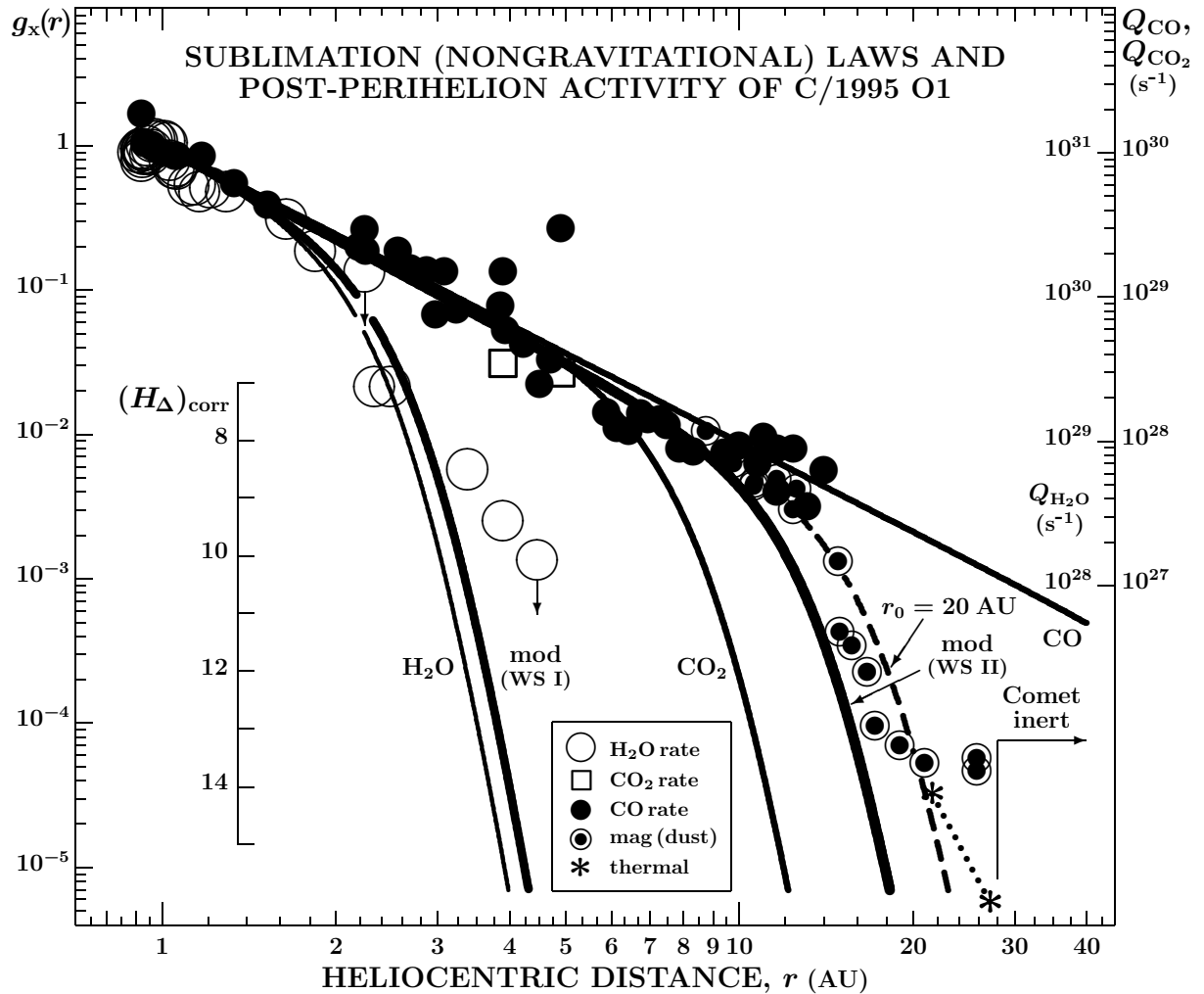


Figure 9. Post-perihelion activity of C/1995 O1 and comparison of the isothermal approximations to the nongravitational and sublimation laws, $g_{\text{mod}}(r; r_0)$. The preferred nongravitational law has a scaling distance $r_0 = 15.36$ AU (Weight System II or WSII), the other has $r_0 = 3.07$ AU (Weight System I or WS I). Also shown are the sublimation laws for water ice, carbon dioxide, and carbon monoxide. In addition, we plot the observed data collected from various sources (see the text): the production rates of water $Q_{\text{H}_2\text{O}}$ (large open circles; including two 3σ upper limits — circles with arrows), carbon dioxide Q_{CO_2} (squares), and carbon monoxide Q_{CO} (solid circles; the anomalously high rate is an ISO data point, Crovisier et al. 1999); the total magnitudes of the dust coma at heliocentric distances greater than 8 AU (the CCD data, obtained by a selected set of observers and extracted from the *Minor Planet Center's* Observations Database, corrected for the contribution from the nucleus, and normalized to a unit geocentric distance and zero phase, $(H_{\Delta})_{\text{corr}}$; circled dots); and, in relative units, the dust coma's thermal flux between 21.6 AU and 27.2 AU (connected asterisks), based on the Spitzer results by Kramer et al. (2014). A crude fit to the dust magnitude data far from the Sun by a $g_{\text{mod}}(r; r_0)$ law is depicted by a dashed line to show that they are approximated by $r_0 \approx 20$ AU. Szabó et al. (2012) argue that the comet became inactive beyond a heliocentric distance of ~ 28 AU.

law downward at about the time of termination of the CO production-rate data; the magnitudes follow, very approximately, a law similar to that with Weight System II, but with a greater scaling distance r_0 , estimated at ~ 20 AU. The last three data points from Table 17 are not plotted in Figure 9; they would be located way below the plot's foot line, referring, in conformity with Szabó et al.'s (2012) conclusion, to a vanishing dust coma.

Two important inferences on the post-perihelion activity of C/1995 O1 are (i) the production of carbon monoxide did not apparently follow an inverse-square power law beyond ~ 15 AU from the Sun, as it should (up to ~ 100 AU) if free CO were available on the nucleus surface, but a steep drop in the dust-coma brightness set in at ~ 15 AU and no dust could be detected in the coma from 28 AU on; and (ii) the dynamically determined non-

gravitational law of Weight System II approximates the comet's post-perihelion activity curve fairly successfully up to almost 20 AU from the Sun, but to achieve the best possible correspondence, the law's scaling distance needs to be increased by some 30%.

A peculiar post-perihelion evolution of the inner coma's brightness, observed extensively by Liller (2001), will be addressed in Part II of this investigation. At this point we are interested in a potential perihelion asymmetry of the comet's activity, for which purpose we now describe the developments along the incoming branch of the orbit.

9.2. The Comet's Preperihelion Activity

The procedure we now followed was the same as for the post-perihelion activity in Section 9.1. The data on the water production rate were assembled, as before, from

Table 18
Pre-Discovery and Averaged Normalized Magnitudes for Dust Coma of C/1995 O1 Between Discovery and 1996 March 20 ($r > 5$ AU preperihelion)

Effective time (UT)	Distance to Sun (AU)	Phase Angle	Magnitude (H_{Δ}) _{corr}	Interval, Number, and Type ^a of Observations	Observer(s)
1991 Sept 1 ^b	16.652	3°1	>15 ^c	Sept 1 (1, phot)	McNaught (?)
1993 Apr 27.8 ^d	13.034	4.2	12.5	Apr 27 (1, phot)	Cass
1995 May 29.4 ^d	7.599	5.0	7.5	May 29 (1, phot)	Dickinson
July 25.7 ^e	7.123	3.4	6.77	July 23–28 (6, vis)	Hale
28.6	7.099	3.8	6.32	July 26–31 (3, CCD)	Nakamura
Aug 1.5	7.066	4.3	6.76	July 30–Aug 3 (7, vis)	Bortle, Hale, Hornoch
10.0	6.994	5.4	6.35	Aug 3–16 (2, CCD)	Nakamura
17.6	6.930	6.3	6.53	Aug 12–21 (8, vis)	Bortle, Hale, Jones
27.7	6.843	7.3	6.49	Aug 23–Sept 1 (10, vis)	Bortle, Hale, Jones
Sept 9.9	6.729	8.2	6.09	Sept 1–18 (2, CCD)	Nakamura
17.4	6.665	8.6	6.16	Sept 12–22 (7, vis)	Bortle, Hale, Hornoch
27.1	6.581	8.8	6.29	Sept 24–30 (8, vis)	Bortle, Hale
Oct 15.4	6.420	8.5	6.04	Oct 13–17 (2, CCD)	Nakamura
19.1	6.388	8.4	6.20	Oct 11–27 (10, vis)	Bortle, Hale, Hornoch, Jones
Nov 13.6	6.162	6.6	5.99	Nov 9–18 (5, vis)	Hale, Jones
1996 Feb 27.6	5.178	8.1	5.35	Feb 23–Mar 2 (6, vis)	Hale, Jones
Mar 14.1	5.028	10.0	5.54	Mar 7–20 (5, vis)	Hale, Jones

Notes.

^a No color corrections applied.

^b Comet not found; estimate for the comet’s total brightness depends on the plate’s adopted limit of mag 21.

^c Conservative upper limit; the dust coma may have been fainter than mag 16 or 17, or absent altogether.

^d Pre-discovery observation.

^e Includes the discovery observation.

the works by Dello Russo et al. (2000), Crovisier et al. (1999), Combi et al. (2000), Weaver et al. (1997, 1999b), Harris et al. (2002), Biver et al. (1997, 1999), and Colom et al. (1999); in addition, we used Weaver et al.’s (1999a) result derived from a ground-based observation of the 4.65- μ m band.

For carbon dioxide, the preperihelion list has six entries, two ISO measurements by Crovisier et al. (1999) and four HST upper limits by Weaver et al. (1999b). On the average, the CO₂ production rate is about a factor of two or so lower than the CO production rate at the same heliocentric distance (between 2.7 and 4.6 AU). Relative to the production of water, the CO₂ production is lower by a factor of 4–5 at 2.9 AU, but they are comparable to one another at 4.6 AU.

The preperihelion production of carbon monoxide was monitored at millimeter and submillimeter wavelengths, starting soon after discovery, by Biver et al. (1997, 1999). It was also measured by Jewitt et al. (1996) in 1995, by Womack et al. (1997) in 1995–1996, by Crovisier et al. (1999) in 1996, by DiSanti et al. (1999) in 1996–1997, and by Weaver et al. (1999a) in 1997.

Normalized dust-coma magnitudes would provide little additional information on the comet’s preperihelion activity, if there were no pre-discovery observations. Because there were, these magnitudes do provide — their low accuracy notwithstanding — some fairly tight constraints. The 1993 observation with the UK Schmidt (McNaught 1995), made by C. P. Cass and already referred to, shows, when combined with the discovery observation, that the rate of brightening between 13 AU and 7 AU was much steeper than r^{-2} . The activity is further constrained by the failed effort by McNaught

(1995) to detect the comet on a plate obtained on 1991 September 1. Assuming with McNaught that the limiting magnitude of the UK Schmidt plate was 21, the nondetection of the comet in 1991 may indicate that its nucleus was nearly or completely inactive, because Szabó et al.’s (2012) results imply that the nucleus should have had a visual magnitude of about 22 at the time of the 1991 observation, equivalent to a normalized magnitude of about 16. The upper limit on the dust-coma magnitude in Table 18 is therefore very conservative. On the other hand, the estimated normalized magnitude of the nucleus at the time of the 1993 detection is about 15, so that the dust coma was then much brighter than the nucleus. Even McNaught’s (1995) estimate of 19 for the so-called nuclear magnitude was at least 1.5 mag brighter than the bare nucleus.

In response to the request by the *Central Bureau for Astronomical Telegrams* for fortuitous pre-discovery observations of the comet (Marsden 1995), another message — besides that by McNaught — was sent by George (1995), who reported an apparent image on a photograph taken with an 8.5-cm f/1.7 lens on a Kodak Royal Gold 400 film by T. Dickinson on 1995 May 29.40 UT, when the comet was of mag 11.7. Although this observation was made only some 8 weeks before discovery, it suggests that the comet was still brightening very rapidly.

Once the comet was discovered, the number of visual observations of its total brightness became overwhelming, and in Table 18 we list averages of estimates by four experienced observers, all of whom used reflectors with apertures between 31 cm and 41 cm: J. Bortle, A. Hale, K. Hornoch, and A. F. Jones. To allow a sufficient overlap in heliocentric distance with the observations of carbon

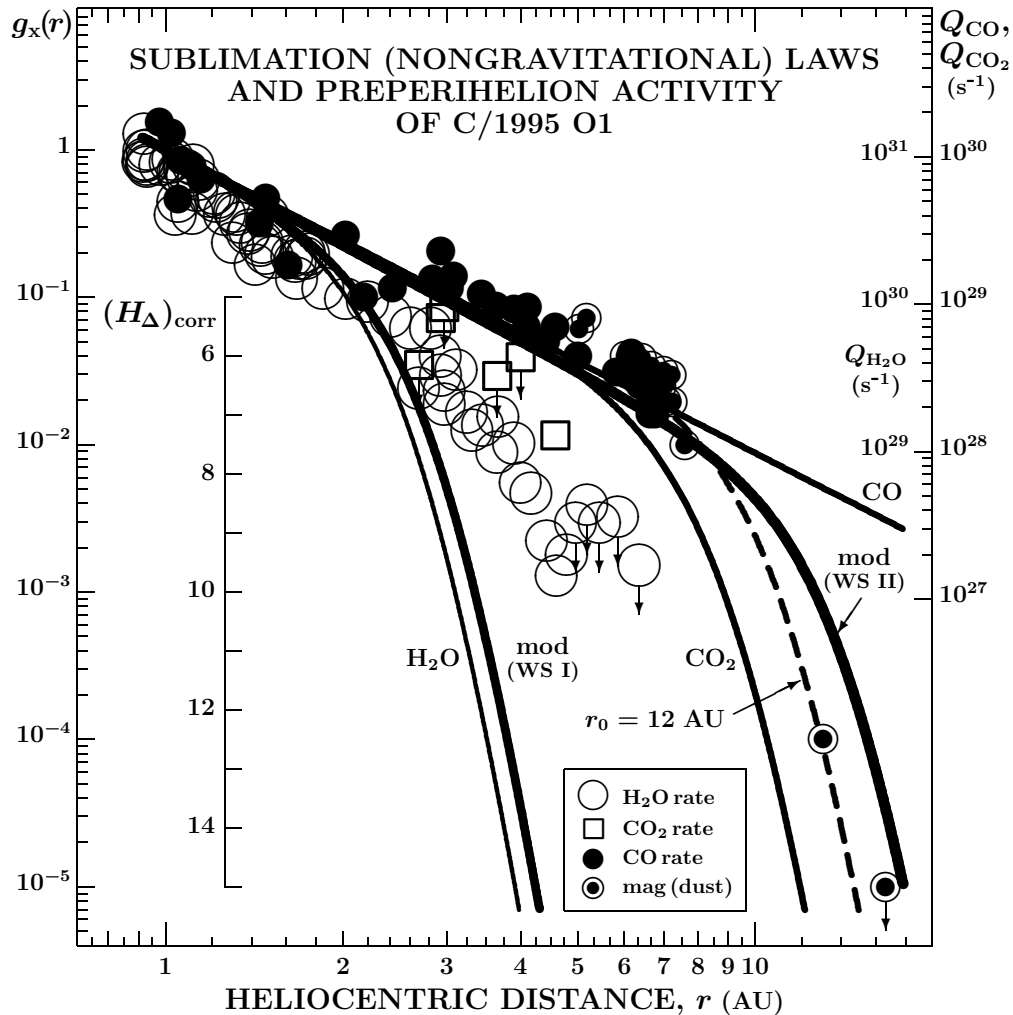


Figure 10. Preperihelion activity of C/1995 O1 and comparison of the isothermal approximations to the nongravitational and sublimation laws, $g_{\text{mod}}(r; r_0)$, which are normalized the same way as in the plot of post-perihelion activity in Figure 9. Similarly, the scales for the observed production rates of water, carbon monoxide, and carbon dioxide have not been changed. Note the increased scatter in the CO data below 3 AU from the Sun. The pre-discovery dust magnitude from 1993 is fitted by a $g_{\text{mod}}(r; r_0)$ law with $r_0 \approx 12$ AU. Comparison with Figure 9 suggests a striking asymmetry relative to perihelion. For a description of the symbols used, see the caption to Figure 9.

monoxide, we covered a wide enough period of time from discovery to 1996 March, during which the comet's heliocentric distance dropped from 7.1 AU to 5 AU. These visual brightness estimates are compared in Table 18 with a series of CCD magnitudes by A. Nakamura, who used a 60-cm f/6.0 Ritchey-Chrétien reflector. Both the visual and CCD data were taken from several issues of the *International Comet Quarterly* (Green 1995, 1996).

The collected information on the preperihelion activity of C/1995 O1 is presented in Figure 10. Although there are similarities between this plot and Figure 9 in general, differences are readily perceived in detail. The water production rates are higher than the post-perihelion ones farther from the Sun, but slightly lower near perihelion, so that the production of H_2O increases less steeply with decreasing heliocentric distance before perihelion than it decreases with increasing distance on the way out. The preperihelion variations in the water production rate can be fitted with a modified nongravitational law (see the beginning of Section 6) with a scaling distance of $r_0 \approx 5$ AU. This is not puzzling because a theoretical

water sublimation curve for a subsolar point requires $r_0 = 5.6$ AU; the observed production curve is therefore still compatible with a simple sublimation model.

The measured preperihelion production curve of carbon monoxide exhibits some inconsistencies. At heliocentric distances exceeding ~ 3 AU, the data by Biver et al. (1997, 1999), Jewitt et al. (1996), DiSanti et al. (1999), and Crovisier et al. (1999) are compatible, showing a systematic increase in the production at a rate slightly steeper than an inverse-square power of decreasing heliocentric distance, strongly resembling the post-perihelion behavior. On the other hand, the production rates by Womack et al. (1997) are for some reason systematically lower by a factor of several, and they are not plotted in Figure 9.

At smaller heliocentric distances the situation is still more precarious. The CO production curve published by Biver et al. (1997, 1999) is stalling or slightly dropping during the approach to the Sun between 3 AU and 2 AU, then grows steeply between 2 AU and perihelion. In contradiction, DiSanti et al.'s (1999) results suggest a

smooth, systematic increase in the production rate all the way to perihelion. This conflict obscures the merit of the points that Bockelée-Morvan & Rickman (1999) make in their comparing the degree of success achieved by three independent models of comet interior proposed, respectively, by Capria et al.’s (1997),⁷ by Prialnik (1997), and by Enzian et al. (1998).

The normalized preperihelion magnitudes $(H_{\Delta})_{\text{corr}}$ are linked with the CO production curve by assuming mag 10 to be equivalent to $1.1 \times 10^{27} \text{ s}^{-1}$, which differs slightly from the post-perihelion equivalent, apparently because of a somewhat different dust-to-CO mass ratio in the coma (Section 9.5). When comparing Figures 9 and 10, the most striking feature is a major *perihelion asymmetry* at heliocentric distances larger than ~ 7 AU, in the sense that the activity is systematically lower before than after perihelion: whereas the post-perihelion dust magnitudes crudely fit a $g_{\text{mod}}(r; r_0)$ law with $r_0 \approx 20$ AU, the 1993 pre-discovery magnitude and the 1991 upper limit are both consistent with $r_0 \approx 12$ AU. The dynamically determined scaling distance of ~ 15.4 AU appears to be a fair compromise, which — the asymmetry notwithstanding — implies a remarkable **correlation between the nongravitational acceleration exerted on the comet’s nucleus and its observed activity**.

9.3. Nongravitational Laws Incorporating Perihelion Asymmetry

The apparent detection of perihelion asymmetry in the activity of C/1995 O1 leads up to the issue of an asymmetric nongravitational law, which, unfortunately, the employed software package does not allow us to apply at present. This tool has over the past several decades been debated in the literature fairly extensively, even though the modern, sophisticated methods of accounting for a nongravitational acceleration, by incorporating it directly in the equations of motion, focused from the beginning on the symmetrical models (Marsden 1969). Tested on 2P/Encke’s comet, the early orbital solutions based on an asymmetric law failed (Marsden 1970) for reasons that have not been fully understood. Similarly, employing an empirical nongravitational law that was consistent with 1P/Halley’s asymmetric water production-rate curve, Yeomans (1984) was unable to improve upon the results obtained with a symmetrical law. Rickman & Froeschlé (1983) [see also Froeschlé & Rickman (1986) and Rickman & Froeschlé (1986)] calculated the expected nongravitational parameters for Halley’s comet from their thermal model of comets, but Landgraf (1986), applying them in his orbital solutions, concluded that, in spite of an improvement, a further refinement was desirable. Subsequently, Sitarski (1990) developed a hybrid model, employing the symmetrical nongravitational law by Marsden et al. (1973), to derive precessional parameters — inherently requiring perihelion asymmetry — for short-period comets.

Returning to the problem of 2P/Encke and motivated by a perception of major seasonal effects and nonrandom distribution of active regions on the nucleus surface as well as by the observed statistical correlation between the perihelion asymmetry of the light curves of comets

and the sense of the nongravitational effect, Sekanina (1988b) suggested that, at the risk of a potentially significant loss of generality, the form of an asymmetric law can be prescribed by applying the standard symmetrical law (Marsden et al. 1973), $g_{\text{ice}}(r; r_0)$ [see Equation (1)], in which the heliocentric distance r is taken not at the time of observation, t , but at a time $t - \tau$, hence $r(t - \tau)$, where τ is a constant “offset” time. The nongravitational acceleration then peaks at a time $t_{\pi} + \tau$ rather than at the time of perihelion, t_{π} ; that is, before perihelion if $\tau < 0$, or after perihelion if $\tau > 0$.

In orbital applications of this asymmetric law, the offset time τ is to be determined by optimizing an orbital solution that fits the astrometric observations of an examined comet. Yeomans & Chodas (1989) employed this paradigm to develop an orbit-determination procedure that allows one to establish the optimum offset time τ as the value used in a solution with a minimum rms residual. Applying this approach to eight short-period comets (including 1P/Halley but not 2P/Encke), they found that in a number of orbital runs this new law improved the fit to astrometric observations and indicated that the radial, rather than transverse, component of the nongravitational acceleration accounted for practically the whole effect (the normal component having been ignored); in most cases, the peak acceleration was offset from perihelion a few weeks in one direction or the other, both the magnitude and the sign of the offset time correlating with those of the offset of the outgassing peak (usually represented by the light curve) from perihelion.

Sitarski (1994a, 1994b) went even further in his application of this type of asymmetric law. He started from his hybrid model, improving it markedly by incorporating the offset time τ and its rate of variation directly into the least-squares procedure, which included all three components of the nongravitational acceleration. Under certain assumptions, he succeeded in fitting — in a single run — the orbital motion of comet 22/P Kopff over 13 returns to perihelion between 1906 and 1990 with an rms residual of $\pm 1''.56$; and by rigorous extrapolation in satisfying, to better than $\pm 1''$, the discovery positions of the comet at its next apparition.

While an asymmetric nongravitational law might improve a fit to the orbital motion of C/1995 O1 over the solution with Weight System II, the paradigm that is customized for applications to short-period comets should be modified. A constant offset time τ , which — based on Combi et al.’s (2000) extensive observations of near-perihelion water production rates — should equal about +19 days for this comet, could not explain the striking difference between the heliocentric distances of the very steep preperihelion increase of activity in Figure 10 (from 13 AU down to 8 AU) and its equally steep post-perihelion drop in Figure 9 (from 12 AU up to 28 AU). In terms of the scaling distance r_0 , the difference between the post-perihelion and preperihelion activity curves is $20 - 12 = 8$ AU, whereas a time difference of 19 days is equivalent to merely ~ 0.13 AU at 12 AU and just about 0.10 AU at 20 AU. Measuring the perihelion asymmetry at a level of, for example, $g_{\text{mod}} = 0.0001$ (see Figures 9 and 10), the preperihelion and post-perihelion heliocentric distances become, respectively, $r_{\text{pre}} = 12.56$ AU and $r_{\text{post}} = 19.37$ AU and the equivalent times from perihelion $t_{\text{pre}} - t_{\pi} = -1360$ days and $t_{\text{post}} - t_{\pi} = +2538$ days, so in

⁷ An updated fit to the observations of C/1995 O1 by this model appears in Capria et al. (2002).

absolute value their difference is 1178 days. For the g_{mod} law to peak at $t_{\pi} + 19$ days and at the same time satisfy $g_{\text{mod}}(12.56 \text{ AU}; 12 \text{ AU}) = g_{\text{mod}}(19.37 \text{ AU}; 20 \text{ AU})$, it must apply $r(t_{\text{pre}} - \tau_*) = r(t_{\text{post}} - \tau_*) = r(t_*)$ and, accordingly, $\tau_* = 589$ days, $t_* = t_{\pi} \mp 1949$ days, and $r_* = 16.14 \text{ AU}$. In order that $g_{\text{mod}}(r_*; r_0) = 0.0001$ at 16.14 AU, the scaling distance r_0 ought to equal

$$r_0 = \left\{ \frac{1 - r_*^{n+m/k} [g_{\text{mod}}(r_*; r_0)]^{1/k}}{r_*^{m/k} [g_{\text{mod}}(r_*; r_0)]^{1/k} - 1} \right\}^{1/n} = 16.10 \text{ AU}. \quad (8)$$

We note that the scaling distance of the law for Weight System II differs from this value by only 0.74 AU.

The offset times at peak outgassing and at $\sim 16 \text{ AU}$ from the Sun represent two critical check points of the asymmetric law $g_{\text{mod}}(r; 16.10 \text{ AU})$. Since the offset time at $\sim 16 \text{ AU}$ is considerably greater — by a factor of 31 — than the offset time near perihelion, the law $g_{\text{mod}}(r; \tau; r_0)$ with a constant offset time τ in the argument of heliocentric distance, $r(t - \tau)$, could not obviously fit the observed perihelion asymmetry of C/1995 O1. It is legitimate to seek a generalized form of τ , called now τ_* , as a product of the offset time at peak outgassing, τ , and a function $h[r_*]$ of heliocentric distance $r_* = r(t - \tau)$. This function should be increasing with r_* , rather than r ($dh/dr_* > 0$), and it should equal unity, $h = 1$, at the time of peak outgassing, t_{peak} [when $t_{\text{peak}} - \tau = t_{\pi}$ and $r_* = r(t_{\text{peak}} - \tau) = q$]:

$$r(t - \tau_*) = r_* = r(t - \tau h[r_*]). \quad (9)$$

We consider two general forms of $h[r_*]$: one is a power function, the other an exponential. In either case, it is necessary to make sure that $h[r]$ does not overcorrect the asymmetry near aphelion. The argument of r should then read either as

$$r_* = r(t - \min\{\tau[r_*/q]^{\nu}, \tau_{\text{max}}\}), \quad (10)$$

or as

$$r_* = r(t - \min\{\tau \exp[\mu(r_* - q)^{\kappa}], \tau_{\text{max}}\}), \quad (11)$$

where ν , μ , κ , and τ_{max} are constants. In practice, either equation is readily solved by successive, rapidly converging iterations, starting with $r_* = r$ in the expressions $(r_*/q)^{\nu}$ or $\exp[\mu(r_* - q)^{\kappa}]$. The two nongravitational laws should be referred to as, respectively, $g_{\text{mod}}(r; \tau, \nu; r_0)$ and $g_{\text{mod}}(r; \tau, \mu, \kappa; r_0)$, but when describing them, as well as $g_{\text{mod}}(r; \tau; r_0)$, summarily, we use the same notation as for the symmetrical law, $g_{\text{mod}}(r; r_0)$. We note that any of the asymmetric laws reduce to the symmetrical law when $\tau = 0$, regardless of the values of ν , μ , or κ . Similarly, the variable offset-time laws reduce to the constant offset-time law when $\nu = 0$ or $\mu = 0$.

For some comets, a better fit should be obtained with expression (10), for others with expression (11). The main difference between the functions (10) and (11) is that the former allows the asymmetry to increase more gradually. The exponential, on the other hand, fits the cases where the perihelion asymmetry increases only insignificantly at small to moderate heliocentric distances, but rather dramatically farther from the Sun. As a practical procedure, we suggest that the overall trend in the perihelion asymmetry of the gas production law between the two end points be employed to choose the type of the

function $h[r_*]$, whereas the magnitudes of the offset time at peak outgassing and far from the Sun be used to fix the function's constants.

Insight into the issue of selecting the function $h[r_*]$ is provided by determining the dependence of the difference in $\log g_{\text{mod}}(r; r_0)$ between a preperihelion and post-perihelion nongravitational effect (or a production rate), $\Delta_{\text{asym}} \log g_{\text{mod}}(r; r_0)$, on the offset time τ_* as a function of heliocentric distance. Differentiating the relation between the time from perihelion and heliocentric distance for parabolic motion (thus obtaining a tight upper limit on the derivative dr/dt) and equating the differential dt with τ_* , we find

$$\Delta_{\text{asym}} \log g_{\text{mod}}(r; r_0) = 0.02113 \frac{\sqrt{r_* - q}}{r_*^2} \left(m + \frac{nk\Lambda_*^n}{1 + \Lambda_*^n} \right) \tau_*, \quad (12)$$

where r_* and q are in AU, τ_* in days, and $\Lambda_* = r_*/r_0$. The difference $\Delta_{\text{asym}} \log g_{\text{mod}}(r; r_0)$ has the same sign as τ_* ; when positive, $g_{\text{mod}}(r; r_0)$ is greater after perihelion, and vice versa.

Comparing Figures 9 and 10 we note that the primary features of the perihelion asymmetry of C/1995 O1's activity could be fitted much better by the offset times that follow an exponential law rather than a power law. The asymmetry is distinctly apparent in close proximity of perihelion (particularly in the variations of the production rate of water) than it is between 3 AU and 7 AU from the Sun (in the CO production). At still larger distances, the differences between preperihelion and post-perihelion rates of outgassing increase dramatically. When $\kappa = 1$ in Equation (11), the two check points require that $\mu = 0.2255 \text{ AU}^{-1}$, so that $\tau_* = 75$ days at $r = 7 \text{ AU}$. When $\kappa = 2$, then one gets $\mu = 0.0148 \text{ AU}^{-2}$ and $\tau_* = 32.9$ days at $r = 7 \text{ AU}$. And when $\kappa = 3$, it follows that $\mu = 0.000973 \text{ AU}^{-3}$ and $\tau_* = 23.7$ days. On the other hand, with the power law from Equation (10), one finds $\nu = 1.20$, so that $\tau_* = 219$ days at $r = 7 \text{ AU}$. Inserting each of these values of τ_* into Equation (12), the perihelion asymmetry in the nongravitational law $g_{\text{mod}}(r; r_0)$ at $r = 7 \text{ AU}$ becomes $\Delta_{\text{asym}} \log g_{\text{mod}} = 0.198$, 0.087 , and 0.063 , respectively, for the three exponential cases, but 0.58 for the power-law case. The case with $\kappa = 3$ is especially satisfactory, as the asymmetry mimics day-to-day variations in the production rate of carbon monoxide, while the power-law case is rather unacceptable.

The superior quality of the exponential law is also apparent from the following figures, in which three asymmetric nongravitational laws are compared with a symmetrical one within 200 days of perihelion (Figure 11) and on another time scale, spanning 18 years (Figure 12). The constant-offset law displays nicely an asymmetry near perihelion, but gradually less so farther from the Sun; it grossly underrates the asymmetry, seen in Figures 9 and 10, at very large heliocentric distances, where it is virtually equivalent to the symmetrical law. The power law fits the large perihelion asymmetry very far from the Sun, but underrates the nongravitational effect before perihelion and overrates it after perihelion on a time scale of months from perihelion. A remarkable quality of the exponential law is that it mimics the behavior of the constant-offset law near perihelion, but of the power law far from the Sun.

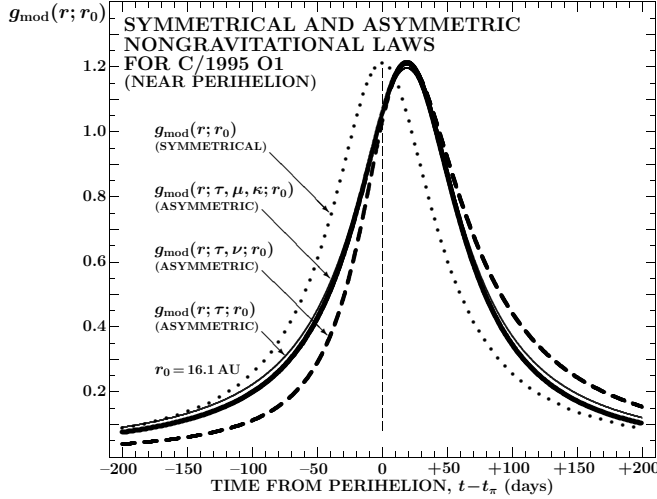


Figure 11. Comparison, within 200 days of perihelion, of four modified nongravitational laws, $g_{\text{mod}}(r; r_0)$, for comet C/1995 O1, all of them having the same scaling distance of $r_0 = 16.10$ AU: (i) $g_{\text{mod}}(r; r_0)$, a symmetrical law with respect to perihelion; (ii) $g_{\text{mod}}(r; \tau; r_0)$, an asymmetric, law with a constant offset time of $\tau = +19$ days; (iii) $g_{\text{mod}}(r; \tau, \nu; r_0)$, an asymmetric law with the offset time following a power function $\tau_* = \tau (r_*/q)^\nu$, where $\tau = +19$ days and $\nu = 1.20$; and (iv) $g_{\text{mod}}(r; \tau, \mu, \kappa; r_0)$, an asymmetric law with the offset time following an exponential function $\tau_* = \tau \exp[\mu (r_* - q)^\kappa]$, where $\tau = +19$ days, $\mu = 0.000973$ AU $^{-3}$, and $\kappa = 3$). Note that, within about 0.5 yr of perihelion, the curve presenting the exponential law — unlike that for the power law — nearly coincides with the curve with a constant offset time, and they both gradually approach the curve of the nongravitational law symmetrical with respect to perihelion.

The only purpose of τ_{max} is to prevent the offset time τ_* from reaching unphysically large values far from the Sun. This is generally not a problem with power laws (unless ν is very high), but is critically important for exponential laws. For example, for C/1995 O1 the exponential laws reach $\tau_* = 100$ yr(!) at $r_* = 34.4$ AU when $\kappa = 1$, at $r_* = 23.5$ AU when $\kappa = 2$, and at $r_* = 20.7$ AU when $\kappa = 3$, that is, at distances only slightly to moderately larger than the scaling distance r_0 . This means that at distances greater than 20–30 AU the integration of the comet’s motion is carried with a constant offset time. Of course, the computed nongravitational effect 30 AU from the Sun reaches merely a $\sim 10^{-10}$ th part of the effect at perihelion, so truncation of offset times far from the Sun has no influence on the accuracy of the computed orbit. Because of a potential for improving the fitting of the motions of comets, it is advisable that the perihelion-asymmetry option in the expression for the nongravitational law discussed above be in the future incorporated in the orbit-determination software.

9.4. Loss of Mass by Outgassing Integrated Over the Orbit. Trace Molecules

In Sections 9.1 and 9.2 we described the major contributors to the activity of C/1995 O1 after and before perihelion, respectively. Our account, based on an extensive list of referenced work, covered the production of water, carbon monoxide, and carbon dioxide. Before we complete the inventory of the volatile species, we note that in-depth investigations of bright comets lead, virtually universally, to two major conclusions: (i) the production

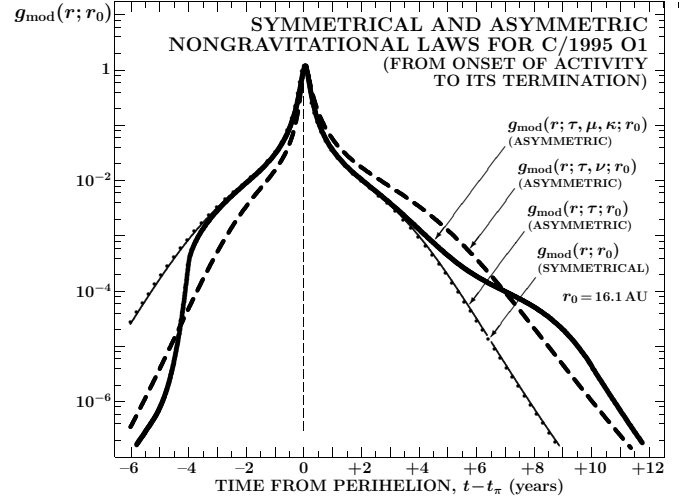


Figure 12. Comparison, from 6 yr preperihelion to 12 yr postperihelion, of the four nongravitational laws plotted on a different scale near perihelion in Figure 11. Note that only the exponential and power laws fit the major perihelion asymmetry, whereby the effects 6 yr before perihelion and 12 yr after perihelion are essentially equal. The offset times are limited to a maximum, τ_{max} , of 3 yr.

rate of water dominates and (ii) activity at large heliocentric distances is controlled by carbon monoxide. Although seldom specified, the first of the two conclusions refers to distances near 1 AU from the Sun, which explains why the two statements are not mutually contradictory. As a rule, incomplete data allow to reliably determine neither the total mass lost by outgassing per orbit, nor the relative contributions to the total provided by water, carbon monoxide, and other species. However, because of the sheer amount of data collected for comet C/1995 O1, its total outgassed mass can be derived rather accurately for water ice and carbon monoxide and at least estimated for carbon dioxide and a number of other volatiles.

Figures 9 and 10 suggest that the $g_{\text{mod}}(r; r_0)$ law, with an appropriate choice of the scaling distance r_0 , offers a satisfactory fit to the variations in the production rates of carbon monoxide (linked at large heliocentric distances to the comet’s light curve) and water. If for a particular species X the production rate at 1 AU from the Sun is $Q_0(X)$ (in molecules per unit time), the loss of mass by this species’ outgassing integrated over the orbit and measured from aphelion to next aphelion, is

$$\Delta \mathcal{M}(X) = Q_0(X) \frac{\mu_{\text{mol}}(X)}{A} \int_{(P)} g_{\text{mod}}(r; r_0) dt, \quad (13)$$

where $\mu_{\text{mol}}(X)$ is the species’ molar mass, A is the Avogadro number, P is the comet’s orbital period, and t is time. As described by Equation (1) with slight modifications, the law $g_{\text{mod}}(r; r_0)$ is a dimensionless function that is symmetrical with respect to perihelion and normalized to $r = 1$ AU. The scaling distance r_0 depends on the species’ latent heat of sublimation, $L_{\text{sub}}(X)$, as shown by Equation (3). The dimension of the integral expression in Equation (13) is time, defining $\mathfrak{S}(X) = \mathfrak{S}(L_{\text{sub}}(X))$:

$$\mathfrak{S}(X) = \int_{(P)} g_{\text{mod}}(r; r_0) dt = \frac{2}{k_{\text{grav}} \sqrt{p}} \int_0^\pi r^2 g_{\text{mod}}(r; r_0) dv, \quad (14)$$

where $p = q(1+e)$, q is the comet's perihelion distance, e its orbital eccentricity, $k_{\text{grav}} = 0.017202099 \text{ AU}^3 \text{ day}^{-1}$ the Gaussian gravitational constant, and v the true anomaly at time t . With r in AU, $\mathfrak{S}(\text{X})$ equates the production of the species X integrated over the orbit with the species' constant production rate, equal to that at 1 AU from the Sun integrated over a period of \mathfrak{S} days, which we call an equivalent time. If the production rate in Equation (13) is expressed in molecules per unit time, the mass loss of the species integrated over the orbit becomes

$$\Delta\mathcal{M}(\text{X}) = Q_0(\text{X}) \frac{\mu_{\text{mol}}(\text{X})}{A} \mathfrak{S}(\text{X}). \quad (15)$$

With a symmetrical law $g_{\text{mod}}(r; r_0)$ one cannot account for the peak production's offset from perihelion, but the asymmetry can be described approximately by choosing different values of Q_0 and r_0 before and after perihelion, allowing a minor discontinuity at perihelion. Denoting the respective production rates at 1 AU by $(Q_0)_{\text{pre}}$ and $(Q_0)_{\text{post}}$ and the respective equivalent times by $\mathfrak{S}_{\text{pre}}$ and $\mathfrak{S}_{\text{post}}$ with the scaling distances of $(r_0)_{\text{pre}}$ and $(r_0)_{\text{post}}$, the total loss of mass of the species X per orbit is

$$\begin{aligned} \Delta\mathcal{M} &= \Delta\mathcal{M}_{\text{pre}} + \Delta\mathcal{M}_{\text{post}} \\ &= \frac{\mu_{\text{mol}}}{2A} \left[(Q_0)_{\text{pre}} \mathfrak{S}_{\text{pre}} + (Q_0)_{\text{post}} \mathfrak{S}_{\text{post}} \right]. \end{aligned} \quad (16)$$

Addressing the perihelion asymmetry in some detail, we first fit the production rates of water, carbon monoxide, and carbon dioxide in Figures 9 and 10. One technique, applied to the production rates of water using the $g_{\text{mod}}(r; r_0)$ law, aims at determining both r_0 and Q_0 . The other technique, applied to the production rates of carbon monoxide, derives only Q_0 , using the scaling distances of 20 AU and 12 AU, already marked in the two figures. For the production rates of carbon dioxide, based on very limited data, we use two approaches: the $g_{\text{mod}}(r; r_0)$ law with $r_0 = 8.9$ AU, which satisfies L_{sub} in Table 16 and Equation (3), and the law intrinsic to CO_2 , whose parameters are in Table 16.

The results in Table 19 show that the sublimation of water ice — while effectively confined to distances of less than 5 AU from the Sun — still prevails after integrating the mass loss over the orbit. The abundance of carbon monoxide (the component outgassed from the nucleus) makes up 14–20% of water in terms of the production rate at 1 AU from the Sun, but 22–32% of water in terms of the mass-loss rate at 1 AU, and it reaches 32% of the total mass of water lost per orbit by the comet's nucleus. A similar trend is shown by carbon dioxide. The summary mass of CO and CO_2 lost per orbit by outgassing from the nucleus amounts to some $\frac{5}{9}$ the mass of lost water, so CO and CO_2 are hardly minor constituents of the comet's volatile reservoir.

Some asymmetry relative to perihelion is apparent from the numbers in Table 19, but not beyond errors. More water and carbon dioxide was released after perihelion than before perihelion, but nearly equal parts of carbon monoxide. However, the fit in Table 19 ignores the anomalously high rate measured after perihelion by the ISO. We already remarked in Section 9.2 on the inconsistencies in the measurements of the preperihelion CO production rates between 3 AU and perihelion, an effect that complicates the mass-loss determination.

Table 19
Loss of Mass of Water Ice, Carbon Monoxide, and Carbon Dioxide Integrated Over Orbit of Comet C/1995 O1

	Water Ice (X = H ₂ O)	Carbon Monoxide ^a (X = CO)	Carbon Dioxide ^b (X = CO ₂)
Before Perihelion			
Number of observations used	58	28	2
Scaling distance $(r_0)_{\text{pre}}$ (AU)	4.72 ± 0.03	12 (fixed ^c)	8.9 (fixed ^d)
Production rate $(Q_0)_{\text{pre}}$ at 1 AU from Sun (s^{-1})	$10^{30.85 \pm 0.09}$	$10^{30.16 \pm 0.10}$	$10^{29.74 \pm 0.20}$
Mass-loss rate $(\mathcal{M}_0)_{\text{pre}}$ at 1 AU from Sun (g s^{-1})	2.1×10^8	0.67×10^8	0.40×10^8
Integral $\frac{1}{2}\mathfrak{S}_{\text{pre}}$ (days)	82.47	98.09	94.22
Mass lost over preperihelion half of orbit, $\Delta\mathcal{M}_{\text{pre}}$ (g)	1.5×10^{15}	0.57×10^{15}	0.3×10^{15}
After Perihelion			
Number of observations used	30	33	2
Scaling distance $(r_0)_{\text{post}}$ (AU)	4.30 ± 0.04	20 (fixed ^c)	8.9 (fixed ^d)
Production rate $(Q_0)_{\text{post}}$ at 1 AU from Sun (s^{-1})	$10^{30.96 \pm 0.09}$	$10^{30.11 \pm 0.12}$	$10^{29.95 \pm 0.15}$
Mass-loss rate $(\mathcal{M}_0)_{\text{post}}$ at 1 AU from Sun (g s^{-1})	2.7×10^8	0.60×10^8	0.65×10^8
Integral $\frac{1}{2}\mathfrak{S}_{\text{post}}$ (days)	80.19	103.08	94.22
Mass lost over post-perihelion half of orbit, $\Delta\mathcal{M}_{\text{post}}$ (g)	1.9×10^{15}	0.53×10^{15}	0.5×10^{15}
Mass lost per orbit, $\Delta\mathcal{M}$ (g)	3.4×10^{15}	1.1×10^{15}	0.8×10^{15}

Notes.

^a Outgassing from the nucleus only; we have made concerted effort to filter out the contribution from the extended source (dust coma).

^b Using the $g_{\text{mod}}(r; r_0)$ law, with a scaling distance $(r_0)_{\text{pre}} = (r_0)_{\text{post}}$, derived from Equation (3) for $L_{\text{sub}} = 6400 \text{ cal mol}^{-1}$ (Table 16). An alternative determination that employs the carbon-dioxide sublimation law (Table 16) results in the same integrated values of mass lost over the orbit and its two halves.

^c As derived in Figures 9 (post-perihelion) and 10 (preperihelion).

^d Outgassing assumed symmetric relative to perihelion because of the absence of information to the contrary.

The level of activity measured by the integrated production of the three species is impressive, the total output per orbit amounting to $5.3 \times 10^{15} \text{ g}$ or the mass of a comet nearly 3 km in diameter at a bulk density of 0.4 g cm^{-3} . This mass does not include dust and a large number of additional volatiles.

The production-rate errors in Table 19 suggest that the results have an uncertainty of about $\pm 20\%$ for water, around $\pm 25\text{--}30\%$ for carbon monoxide, and around $\pm 40\%$ for the poorly observed carbon dioxide. The scaling distance r_0 for water ice is distinctly greater than 2.8 AU, an effect that is clearly apparent from Figure 10. The discrepancy can be explained as a corollary to the preferential sunward outgassing; the scaling distance of ~ 2.8 AU applies, as noted in the text near Equations (1) and (3), to the orbital data fitting isothermal model; it is known (e.g., Sekanina 1988a) that in an extreme case of outgassing from the subsolar area only, the scaling distance for water-ice sublimation becomes twice as large, 5.6 AU, and any intermediate value is possible depending on the degree of anisotropy. The scaling distance also depends weakly on the Bond albedo and emissivity of the nucleus' surface. For carbon monoxide the scaling distance may have to do with limited volumes of this ice's reservoirs on and below the surface, an issue that is be-

yond the scope of this paper, but was discussed at some length by Szabó et al. (2011, 2012). The uncertainty in the scaling distance does not fundamentally affect the results and it does not significantly increase the error.

We note that the earliest positive detection of water was achieved when the comet was 4.6 AU from the Sun, or $0.97r_0$, on its way to perihelion (Biver et al. 1999), while the last one when the comet was 4.4 AU, or $1.02r_0$, on its way out (Biver et al. 2002). It may not be completely a chance that the most distant detection of water takes place when the comet's heliocentric distance approximately equals the scaling distance, because at these distances the $g_{\text{mod}}(r; r_0)$ is very steep, always varying as $r^{-13.9}$, so that a very minor change in r implies a dramatic change in the production rate. If this rule should apply generally, we predict that the least volatile species that could be detected in a comet are those for which $r_0 = q$; in the orbit of C/1995 O1, an upper limit on the sublimation heat is nearly exactly $20\,000 \text{ cal mol}^{-1}$ for the isothermal model, but slightly more than $\sim 28\,000 \text{ cal mol}^{-1}$ for the model with an extreme outgassing anisotropy (subsolar outgassing).

Although the mass lost per orbit is the prime characteristic of each species' outgassing, it is the observed production rate near perihelion, or near 1 AU from the Sun, that is routinely tabulated by the observers. For species other than water, it is fairly customary to present their production rates in units of the water production rate. Since an output ratio of a species relative to water depends on whether it is given in terms of the production rate or the mass-loss rate of the mass loss per orbit, we present the relationships among these three measures that the isothermal model provides. Let $\mathfrak{R}_Q(\text{X})$ be the ratio of the production rate of a species X to the water production rate (sometimes also called a relative abundance) at 1 AU from the Sun,

$$\mathfrak{R}_Q(\text{X}) = \frac{Q_0(\text{X})}{Q_0(\text{H}_2\text{O})}; \quad (17)$$

let $\mathfrak{R}_\mu(\text{X})$ be the ratio of the respective molar masses,

$$\mathfrak{R}_\mu(\text{X}) = \frac{\mu_{\text{mol}}(\text{X})}{\mu_{\text{mol}}(\text{H}_2\text{O})}; \quad (18)$$

let $\mathfrak{R}_\mathfrak{S}(\text{X})$ be the nominal⁸ orbit-integrated production (i.e., equivalent time) ratio,

$$\mathfrak{R}_\mathfrak{S}(\text{X}) = \frac{\mathfrak{S}(\text{X})}{\mathfrak{S}(\text{H}_2\text{O})}; \quad (19)$$

and let $\mathfrak{R}(\text{X})$ be the nominal orbit-integrated mass-loss ratio,

$$\mathfrak{R}(\text{X}) = \mathfrak{R}_\mu(\text{X}) \mathfrak{R}_\mathfrak{S}(\text{X}); \quad (20)$$

we define $\mathfrak{R}_\mathcal{M}(\text{X})$, the mass loss of the species X per orbit in units of the mass loss of water ice per orbit,

$$\mathfrak{R}_\mathcal{M}(\text{X}) = \frac{\Delta\mathcal{M}(\text{X})}{\Delta\mathcal{M}(\text{H}_2\text{O})}, \quad (21)$$

as a product

$$\mathfrak{R}_\mathcal{M}(\text{X}) = \mathfrak{R}_Q(\text{X}) \mathfrak{R}(\text{X}) = \mathfrak{R}_Q(\text{X}) \mathfrak{R}_\mu(\text{X}) \mathfrak{R}_\mathfrak{S}(\text{X}). \quad (22)$$

⁸ Nominal here meaning for $\mathfrak{R}_Q = 1$.

The observers publish $\mathfrak{R}_Q(\text{X})$, and it is $\mathfrak{R}(\text{X})$ — and therefore $\mathfrak{R}_\mathfrak{S}(\text{X})$ — that we need to know in order to determine the mass loss of X per orbit relative to water. Even though the actual function is unknown, an example with carbon monoxide below illustrates that application of Equation (14) with the scaling distance r_0 tied to the sublimation heat L_{sub} by Equation (3) is robust enough to provide us with a reasonably informative estimate for the factor that allows us to convert, according to Equation (22), the reported production-rate ratio $\mathfrak{R}_Q(\text{X})$ into the physically more meaningful ratio of the mass loss per orbit, $\mathfrak{R}_\mathcal{M}(\text{X})$.

The dependence of the equivalent time \mathfrak{S} on the sublimation heat L_{sub} in the range of up to $30\,000 \text{ cal mol}^{-1}$ is for an isothermal model of the nucleus and a perihelion symmetry in outgassing displayed in Figure 13. The gradual drop in \mathfrak{S} on the left of the figure is understood: as L_{sub} increases, the sublimation is effectively limited to an ever shorter arc of the orbit around perihelion, so that $d\mathfrak{S}/dL_{\text{sub}} < 0$. However, somewhat surprisingly, the curve attains a minimum at $L_{\text{sub}} = 16\,300 \text{ cal mol}^{-1}$ and then continues to climb, reaching the equivalent time of water [$\mathfrak{S}(\text{H}_2\text{O}) \simeq 135$ days] at $L_{\text{sub}} \approx 20\,000 \text{ cal mol}^{-1}$, exceeding the equivalent time of hyper-volatile species, $\lim_{L_{\text{sub}} \rightarrow 0} \mathfrak{S} \simeq 231$ days, at $L_{\text{sub}} \gtrsim 25\,000 \text{ cal mol}^{-1}$, and converging to $\lim_{L_{\text{sub}} \rightarrow \infty} \mathfrak{S} \simeq 261$ days. This behavior can be explained by an increasing steepness of the sublimation curve at close proximity to perihelion: most mass of such volatiles is not lost until the comet gets within 1 AU of the Sun and their abundances \mathfrak{R}_Q diminish progressively with increasing L_{sub} .⁹ This trend is consistent with our independent conclusion above that outgassing of species with a sublimation heat exceeding $20\,000 \text{ cal mol}^{-1}$ should be increasingly rare in C/1995 O1 and that species with the sublimation heat near or greater than $\sim 28\,000 \text{ cal mol}^{-1}$ should not be detected at all. The shape of the curve $\mathfrak{S}(L_{\text{sub}})$ depends very strongly on the perihelion distance (Appendix B).

In an effort to assess a cumulative contribution to the orbit-integrated mass loss by various species, we list in Table 20 the parent molecules observed in C/1995 O1, as compiled by Bockelée-Morvan et al.'s (2004), and compare them with a set of selected entries from Acree & Chickos' (2016) compendium of organic and organometallic compounds, whose latent heat of sublimation (sublimation enthalpy) does not, in concert with the constraints above, exceed $30\,000 \text{ cal mol}^{-1}$.

The table is ordered by the latent heat of sublimation, L_{sub} , which is known to be only a weak function of temperature. For most entries the listed values of L_{sub} were compiled by Acree & Chickos (2016) in their compendium from an extensive set of sources. In the majority of cases the results from different sources for different temperature ranges agreed with each other quite well, often within a few percent or so. For some molecules, for which the sublimation heat was not listed by Acree & Chickos (2016), we were able to learn the information

⁹ Note that $r_0 < 1.37$ AU for $L_{\text{sub}} > 16\,300 \text{ cal mol}^{-1}$ and that $r_0 < 0.58$ AU for $L_{\text{sub}} > 25\,000 \text{ cal mol}^{-1}$; thus, even perihelion of C/1995 O1 is in a thermal regime dominated by reradiation, with only a minor fraction of the solar energy spent on sublimation of species with such a high sublimation heat. Of course, the $g_{\text{mod}}(r; r_0)$ law is then only an approximation to the genuine sublimation law, which is exponential.

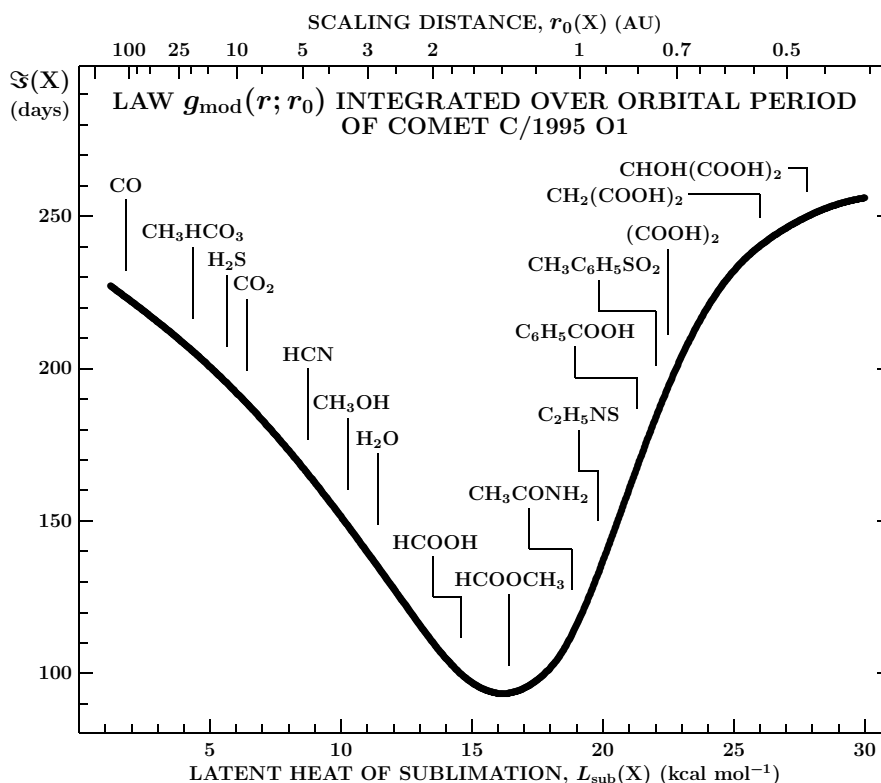


Figure 13. Law $g_{\text{mod}}(r; r_0)$, integrated over the orbit of C/1995 O1 as a function of the latent heat of sublimation L_{sub} that determines the scaling distance r_0 according to Equation (3), and expressed as an equivalent time \mathfrak{S} , defined by Equation (14). Contrary to expectation, the equivalent time \mathfrak{S} reaches a minimum near $L_{\text{sub}} = 16\,300 \text{ cal mol}^{-1}$. The locations in the graph of 16 selected volatile species are identified by their chemical formulas. All molecules to the left of the curve's minimum and inclusive have been identified in C/1995 O1, with the exception of methyl hydrogen carbonate, CH_3HCO_3 . None of the seven molecules to the right of the minimum has been detected.

from the chemistry webbook of the National Institute of Standards and Technology (NIST).¹⁰ For several tabulated species, mostly those observed in C/1995 O1, the sublimation heat apparently has not been determined; in the majority of these instances its value could be approximated by the sum of values of the heat of vaporization and the heat of fusion, if both known (though usually referring to different temperatures) and is then parenthesized. For only three tabulated molecules we were able to find only the heat of vaporization, which provides a lower limit to the heat of sublimation; the heat of fusion typically amounts to only a minor fraction of the heat of sublimation.

Highly relevant to the determination of the total mass loss by outgassing are columns 5–7 of Table 20, in which we list, respectively, the water-normalized ratios \mathfrak{R}_μ , $\mathfrak{R}_\mathfrak{S}$, and \mathfrak{R} , the last one being the factor that converts the production rate to the mass loss integrated over the orbit. For example, Bockelée-Morvan et al. (2004) state that the production rate of carbon monoxide from the nucleus was 12% of the water rate. Table 20 lists $\mathfrak{R} = 2.56$ for carbon monoxide, which suggests that its mass loss per orbit was 12% times $2.56 = 31\%$, in excellent agreement with the result in Table 19, which gives 32% of the water mass loss.

Also apparent from Table 20 is that most species detected in C/1995 O1 were more volatile than water, including carbon monoxide (the most volatile one) and car-

bon dioxide. However, three of the detected molecules were more refractory than water; the most refractory one, ethylene glycol,¹¹ has an estimated sublimation heat of $\sim 18\,000 \text{ cal mol}^{-1}$, somewhat below an upper limit on the sublimation heat for an isothermal model.

We note from Table 20 that the nominal mass-loss ratio \mathfrak{R} is always greater than unity.¹² Of the two factors that contribute to \mathfrak{R} , $\mathfrak{R}_\mathfrak{S}$ has a generally minor effect, varying between about 0.7 and 1.9. By contrast, \mathfrak{R}_μ ranges from 0.9 to nearly 17. The heaviest molecule detected in C/1995 O1 was carbon disulfide with $\mathfrak{R}_\mu = 4.22$, followed by sulfur dioxide ($\mathfrak{R}_\mu = 3.56$) and ethylene glycol ($\mathfrak{R}_\mu = 3.55$). Since the first two are more volatile than the last one, their values of \mathfrak{R} are proportionally higher. Table 20 lists eight species whose molar mass is more than six times as high as that of water ($\mathfrak{R}_\mu > 6$), of which three are more volatile than the two least volatile molecules detected in C/1995 O1. Relative to their contribution to the total production rate, such species are the most effective contributors to the comet's total mass lost by outgassing.

The fact that the mass loss per orbit of any of the listed molecules is, relative to water, greater than the production rate near 1 AU is consistent with what we concluded about carbon monoxide and carbon dioxide

¹¹ Its detection, not included in Bockelée-Morvan et al.'s (2004) compilation, was reported by Crovisier et al. (2004a).

¹² The three upper limits are meant to indicate that the probable values should be some 10–20% lower, still much greater than unity.

¹⁰ For access, see <http://webbook.nist.gov/chemistry/>.

Table 20
Heat of Sublimation and Mass Loss for Observed and Potential Volatile Species in Comet C/1995 O1

Outgassing Species, X	Formula	Latent Heat of Sublimation, $L_{\text{sub}}(X)$ (cal mol ⁻¹)	Molar Mass, $\mu_{\text{mol}}(X)$ (g mol ⁻¹)	Molar Mass Ratio, $\mathfrak{R}_{\mu}(X)$	Nominal Production Ratio, $\mathfrak{R}_{\Sigma}(X)$	Nominal Mass-Loss Ratio, $\mathfrak{R}(X)$	Bullet If Detected in Comet C/1995 O1	Notes ^a
Carbon monoxide	CO	1785	28.01	1.55	1.65	2.56	●	b
Methane	CH ₄	2300	16.04	0.89	1.63	1.45	●	
Ethylene	C ₂ H ₄	4200	28.05	1.56	1.53	2.39		
Methyl hydrogen carbonate	CH ₃ HCO ₃	4350	76.05	4.11	1.52	6.25		
Ketene (Ethenone)	CH ₂ CO	>4800	42.04	2.33	<1.50	<3.50		c,d
Ethane	C ₂ H ₆	5150	30.07	1.67	1.48	2.47	●	
Acetylene	C ₂ H ₂	5500	26.04	1.45	1.45	2.10	●	
Hydrogen sulfide	H ₂ S	5650	34.08	1.89	1.45	2.74	●	
Nitrous oxide	N ₂ O	5820	44.01	2.44	1.43	3.49		c
Carbonyl sulfide	OCS	(6000)	60.08	3.33	1.42	4.73	●	e
Dimethyl ether (Methoxymethane)	CH ₃ OCH ₃	(6300)	46.07	2.56	1.40	3.58		c,e
Carbon dioxide	CO ₂	6400	44.01	2.44	1.40	3.42	●	b
Acetaldehyde	CH ₃ CHO	(6800)	44.05	2.45	1.37	3.36	●	e
Methyl formate (Methyl methanoate)	HCOOCH ₃	>6800	60.05	3.33	<1.37	<4.56	●	d
Hydrogen cyanate (Isocyanic acid)	HNCO	>7300	43.03	2.39	<1.33	<3.18	●	d
Ammonia	NH ₃	7450	17.03	0.95	1.32	1.25	●	
Methyl isothiocyanide	C ₂ H ₃ NS	7530	73.12	4.06	1.32	5.36		
Formaldehyde	H ₂ CO	(7600)	30.03	1.67	1.31	2.19	●	e,f
Carbon disulfide	CS ₂	(7800)	76.13	4.22	1.30	5.49	●	e
Sulfur dioxide	SO ₂	(7900)	64.07	3.56	1.29	4.59	●	e
Cyanogen	(CN) ₂	8000	52.04	2.89	1.28	3.70		
Acetone	CH ₃ COCH ₃	8320	58.08	3.22	1.26	4.06		
Hydrogen cyanide (Cyanic acid)	HCN	8720	27.03	1.50	1.23	1.85	●	
Ethyl cyanide (Propionitrile)	CH ₃ CH ₂ CN	(9900)	55.08	3.06	1.13	3.46		c,e
Methyl cyanide (Acetonitrile)	CH ₃ CN	(10 000)	41.05	2.28	1.12	2.55	●	e
Cyanoacetylene	HC ₃ N	10 100	51.05	2.83	1.11	3.14	●	
Methanol	CH ₃ OH	10 600	32.04	1.78	1.07	1.90	●	
Trimethylammonium cyanide	(CH ₃) ₃ NHCN	10 800	86.14	4.78	1.05	5.02		
Trinitromethane	CH(NO ₂) ₃	11 000	151.04	8.38	1.04	8.72		
Tetranitromethane	C(NO ₂) ₄	11 300	196.04	10.88	1.01	10.99		
Water ice	H ₂ O	11 400	18.02	1.00	1.00	1.00	●	b
Pyrazine	C ₄ H ₄ N ₂	13 400	80.09	4.44	0.83	3.69		
Formic acid (Methanoic acid)	HCOOH	14 600	46.03	2.55	0.74	1.89	●	
Acetic acid (Ethanoic acid)	CH ₃ COOH	16 400	60.05	3.33	0.69	2.30		c
Hexanitroethane	(NO ₂) ₃ C ₂ (NO ₂) ₃	16 900	300.05	16.65	0.70	11.66		
Formamide (Methanamide)	NH ₂ CHO	17 200	45.04	2.50	0.71	1.78	●	
Methyl carbamate	CH ₃ OCONH ₂	17 700	75.07	4.17	0.73	3.04		
Cyanamide	NH ₂ CN	18 000	42.04	2.33	0.75	1.75		c
Ethylene glycol	(CH ₂ OH) ₂	(18 200)	62.07	3.44	0.77	2.65	●	e,g
Methylsulfonylmethane	(CH ₃) ₂ SO ₂	18 400	94.13	5.22	0.79	4.12		
Acetamide	CH ₃ CONH ₂	18 800	59.07	3.28	0.83	2.72		
Thioacetamide	C ₂ H ₅ NS	19 800	75.13	4.17	0.98	4.09		
Benzoic acid	C ₆ H ₅ COOH	21 300	122.12	6.78	1.24	8.41		
Methyl phenyl sulfone	CH ₃ C ₆ H ₅ SO ₂	22 000	156.20	8.67	1.36	11.79		
Oxalic acid	(COOH) ₂	22 300	90.03	5.00	1.41	7.05		
Dimethylglyoxime	(CH ₃) ₂ C ₂ (NOH) ₂	23 100	116.12	6.44	1.52	9.79		
Dithiooxamide (Rubeanic acid)	(CH ₂ NS) ₂	25 000	120.19	6.67	1.72	11.47		
Malonic acid	CH ₂ (COOH) ₂	26 000	104.06	5.77	1.78	10.27		
Tartonic acid	CHOH(COOH) ₂	27 800	120.06	6.66	1.85	12.32		
Thiosemicarbazide	NH ₂ NHCSNH ₂	30 000	91.14	5.06	1.90	9.61		

Notes.

^a Sublimation-heat and molar-mass data taken mostly from Acree & Chickos' (2016) updated compendium or from the National Institute of Standards and Technology (NIST) webbook. Detection in C/1995 O1 as reported by Bockelée-Morvan et al. (2004), unless stated otherwise.

^b Latent heat of sublimation taken from Table 16; averages of the data listed in Acree & Chickos' (2016) compendium are 1880 cal mol⁻¹ and 6250 cal mol⁻¹ for CO and CO₂, respectively.

^c Listed by Crovisier et al. (2004b) and/or by Bockelée-Morvan et al. (2004) among species searched for but not detected in C/1995 O1.

^d Latent heat of sublimation unavailable; latent heat of vaporization used to estimate its lower limit.

^e Latent heat of sublimation unavailable, but approximated by a sum of latent heats of fusion and vaporization at available temperatures.

^f Released by polyoxymethylene (POM) decomposition from dust (e.g., Cottin & Fray 2008); production curve too steep for release from nucleus.

^g Detection in C/1995 O1 reported by Crovisier et al. (2004a).

Table 21
Trace Parent Molecules Detected in C/1995 O1^a

Outgassing Species, X	Production Rate Ratio, ^b $\mathfrak{R}_Q(X)$	Nominal Mass-Loss Ratio, $\mathfrak{R}(X)$	Mass Loss Relative to H ₂ O, $\mathfrak{R}_M(X)$	Mass Loss Per Orbit, $\Delta\mathcal{M}(X)$ (10 ¹⁵ g)
Methane	0.015	1.45	0.022	0.074
Ethane	0.002 ^c	2.47	0.005	0.017
Acetylene	0.006	2.10	0.013	0.043
Hydrogen sulfide	0.015	2.74	0.041	0.140
Carbonyl sulfide	0.004	4.73	0.019	0.064
Acetaldehyde	0.00025	3.36	0.0008	0.003
Methyl formate	0.0008	<4.56	<0.003	<0.012
Hydrogen cyanate	0.0010	<3.18	<0.003	<0.011
Ammonia	0.007	1.25	0.009	0.030
Carbon disulfide	0.002	5.49	0.011	0.037
Sulfur dioxide	0.002	4.59	0.009	0.031
Hydrogen cyanide	0.0029 ^d	1.85	0.005	0.018
Methyl cyanide	0.0002	2.55	0.0005	0.0017
Cyanoacetylene	0.0002	3.14	0.0006	0.0021
Methanol	0.024	1.90	0.046	0.155
Formic acid	0.0009	1.89	0.0017	0.006
Formamide	0.00015	1.78	0.0003	0.0009
Ethylene glycol	0.0025	2.65	0.007	0.023
Total (rounded off)	0.064	0.19	0.65

Notes.

^a Not listed are formaldehyde (H₂CO), released from dust in the coma (Table 20), and two unstable species that are not candidates for parent molecules: thioformaldehyde (H₂CS) and radical NS.

^b As compiled and published by Bockelée-Morvan et al. (2004) and by Crovisier et al. (2004a, 2004b).

^c Average taken of the range 0.001 to 0.003.

^d Including the contribution from hydrogen isocyanide.

in connection with Table 19. If the production rates for the trace molecules, presented by Bockelée-Morvan et al. (2004), refer essentially to 1 AU from the Sun, the mass of each of the 18 parent species¹³ lost over the orbit of C/1995 O1 is listed in Table 21. By summing up the data, we show that while their total production rate equaled merely 6.4% of the water production rate, their total mass lost per orbit amounted to 19% of the water mass loss, thus averaging $\sim 1\%$ per trace species. Together with carbon monoxide and carbon dioxide (Table 19), this makes up 75% of the water mass loss.

Additional molecules that were searched for, but not detected, in C/1995 O1 (Crovisier et al. 2004b, Bockelée-Morvan et al. 2004) are listed in Table 22, which again shows that an upper limit on the production rate is much tighter than the limit on the orbit-integrated loss of mass by outgassing. The latter is 3 times higher than the former in Table 21 and 2.8 times higher in Table 22.

Since the parent molecules detected in C/1995 O1 (as well as in other comets) are primarily hydrocarbons, often oxygen, nitrogen, and/or sulfur-bearing, one wonders — given the enormous variety of compounds into which these elements can combine — how many more similar, fairly volatile species are there still waiting to be dis-

¹³ Excluding formaldehyde, probably released from dust grains in the comet's atmosphere (e.g., Cottin & Fray 2008), as well as thioformaldehyde and a radical NS (unstable compounds that are not candidates for a parent molecule), deuterated species, and ions.

covered in comets and, in particular, what is their total mass relative to the mass of the water-ice reservoir. This question prompted Crovisier et al. (2004b) to inspect the distribution of the relative abundances of more than 20 detected species, that is, their cumulative number, \mathcal{N} , as a function of their relative production rate, \mathfrak{R}_Q . Their plot shows the dataset to have a tendency to vary as a power law, $\mathcal{N} \propto \mathfrak{R}_Q^{-0.4}$, and suggests that the dataset is increasingly incomplete at $\mathfrak{R}_Q < 10^{-3}$. Crovisier et al. (2004b) pointed out that this effect appeared to tie in with the well-known existence of numerous unidentified features in diverse parts of cometary spectra.

As we are primarily interested in estimating a total mass lost by outgassing per orbit of C/1995 O1, we prepared in Figure 14 a plot of the distribution of the orbit-integrated mass loss, $\Delta\mathcal{M}$, of the species presented in Tables 19 and 21. The dependence of a cumulative number \mathcal{N} of the species on the ratio \mathfrak{R}_M expresses the mass loss per orbit in units of the total mass loss of water ice. Whereas \mathfrak{R}_M has up to now been a function of the species X, we now treat the cumulative distribution as a continuous function of \mathfrak{R}_M and note that the mass loss in an interval between \mathcal{N} and $\mathcal{N}+d\mathcal{N}$ is $\mathfrak{R}_M(\mathcal{N})d\mathcal{N}$. We assume the function \mathcal{N} to vary as a power of \mathfrak{R}_M (with $\mathcal{N}=1$ for $\mathfrak{R}_M=1$),

$$\mathcal{N} = \mathfrak{R}_M^{-y}, \quad (23)$$

so that $d\mathcal{N} = -y\mathfrak{R}_M^{-(y+1)}d\mathfrak{R}_M$, and for the total mass

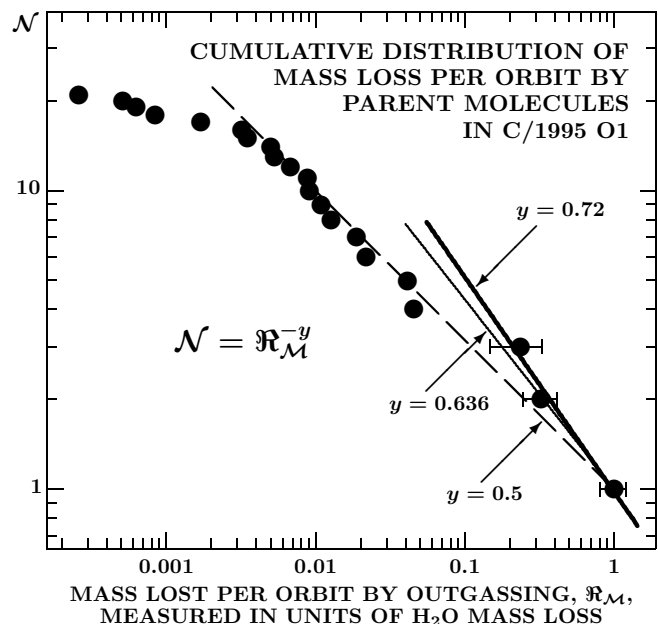


Figure 14. Cumulative distribution of the orbit-integrated mass loss by the outgassing parent molecules detected in C/1995 O1. The number of species, \mathcal{N} , is plotted against the mass lost by them over the orbit, \mathfrak{R}_M , measured in units of the mass lost by the sublimation of water ice, $(0.34 \pm 0.07) \times 10^{16}$ g. The total mass lost per orbit by all volatile species is $\mathfrak{R}_\infty = y(1-y)^{-1}$, where $-y$ is the slope of the cumulative distribution. In order that \mathfrak{R}_∞ be finite, it must be $y < 1$. The thick line, $y = 0.72$, is a fit through the three most abundant species (water, carbon monoxide, and carbon dioxide); the thin line, $y = 0.636$, is a lower limit to the power law, based on the number of parent species that are currently known to outgass from the comet's nucleus; and the dashed line, $y = 0.5$, is a constraint required by an extreme case, when water outgassing accounts for all the lost mass, $\mathfrak{R}_\infty = 1$.

Table 22
Upper Limits on Volatile Species Searched for Though Undetected in C/1995 O1^a

Outgassing Species, X	Formula	Production Rate Ratio, \mathfrak{R}_Q	Latent Heat of Sublimation, ^b $L_{\text{sub}}(X)$ (cal mol ⁻¹)	Molar Mass, $\mu_{\text{mol}}(X)$ (g mol ⁻¹)	Molar Mass Ratio, $\mathfrak{R}_\mu(X)$	Nominal Production Ratio, $\mathfrak{R}_\mathfrak{S}(X)$	Nominal Mass-Loss Ratio, $\mathfrak{R}(X)$	Mass Loss Relative to H ₂ O, \mathfrak{R}_M	Mass Loss Per Orbit, $\Delta\mathcal{M}(X)$ (10 ¹⁵ g)
Phosphine	PH ₃	<0.00016	4100	34.00	1.89	1.54	2.91	<0.00047	<0.0016
Ketene	CH ₂ CO	<0.00032	>4800	42.04	2.33	<1.50	<3.50	<0.0011	<0.0038
Propyne	CH ₃ CCH	<0.00045	>5500	40.06	2.22	<1.45	<3.22	<0.0014	<0.0049
Nitrous oxide	N ₂ O	<0.0023	5820	44.01	2.44	1.43	3.49	<0.0080	<0.027
Dimethyl ether	CH ₃ OCH ₃	<0.0045	(6300)	46.07	2.56	1.40	3.58	<0.0072	<0.024
Ethylene oxide	C ₂ H ₄ O	<0.0020	(7600)	44.05	2.45	1.31	3.21	<0.0064	<0.022
Methyl mercaptan	CH ₃ SH	<0.0005	(7900)	48.11	2.67	1.29	3.44	<0.0017	<0.0059
Ethyl cyanide	CH ₃ CH ₂ CN	<0.0001	(9900)	55.08	3.06	1.13	3.46	<0.00035	<0.0012
Ethanol	CH ₃ CH ₂ OH	<0.0010	(11 100)	46.07	2.56	1.03	2.64	<0.0026	<0.0090
Hydrogen peroxide	H ₂ O ₂	<0.0003	>11 600	34.01	1.89	<0.98	<1.85	<0.0006	<0.0019
Hydroxylamine	NH ₂ OH	<0.0025	15 300	33.03	1.83	0.71	1.30	<0.0032	<0.011
Acetic acid	CH ₃ COOH	<0.0006	16 400	60.05	3.33	0.69	2.30	<0.0014	<0.0047
Glycolaldehyde	CH ₂ OHCHO	<0.0004	>16 700	60.05	3.33	≥0.69	≥2.30	<0.0009	<0.003
Cyanamide	NH ₂ CN	<0.00004	18 000	42.04	2.33	0.75	1.75	<0.00007	<0.0002
Sodium chloride	NaCl	<0.000008	23 800 ^c	58.44	3.24	1.61	5.22	<0.00004	<0.00014
Glycine I	NH ₂ CH ₂ COOH	<0.0015	32 700	75.07	4.17	1.92	8.00	<0.012	<0.041
Methanimine	CH ₂ NH	<0.00032	29.04	1.61	~1(?)	~1.6(?)	<0.0005(?)	<0.0017(?)
Sodium hydroxide	NaOH	<0.000003	40.00	2.22	~1(?)	~2.2(?)	<0.00001(?)	<0.00002(?)
Fulminic acid	HCNO	<0.000016	43.02	2.39	~1(?)	~2.4(?)	<0.00004(?)	<0.00013(?)
Thioformaldehyde	H ₂ CS	<0.0004	46.09	2.56	~1(?)	~2.6(?)	<0.0010(?)	<0.0035(?)
Cyanodiacetylene	HC ₅ N	<0.00003	75.07	4.17	~1(?)	~4.2(?)	<0.00013(?)	<0.0004(?)
Total (rounded off)	<0.0175	<0.049	<0.167

Notes.

^a The 3 σ upper limits as published by Crovisier et al. (2004b) and by Mocketé-Morvan et al. (2004). Sublimation-heat and molar-mass data taken mostly from Acree & Chickos' (2016) updated compendium or from the National Institute of Standards and Technology (NIST) webbook.

^b When unavailable, L_{sub} was approximated by a sum of latent heats of fusion and vaporization (parenthesized values); when the fusion heat was unavailable, a lower limit to L_{sub} was equated with vaporization heat; when the vaporization heat was unavailable (last five entries), we approximated the ratio $\mathfrak{R}_\mathfrak{S}$ by unity (values with a question mark).

^c The value determined from the Antoine equation.

loss per orbit experienced by all outgassing species, \mathfrak{R}_∞ , we get

$$\mathfrak{R}_\infty = \int_1^\infty \mathfrak{R}_M d\mathcal{N} = -y \int_1^0 \mathfrak{R}_M^{-y} d\mathfrak{R}_M = \frac{y}{1-y}, \quad (24)$$

where $0.5 < y < 1$. The limits on y are dictated by requiring that \mathfrak{R}_∞ be finite, positive, and greater than unity. The infinite upper limit in the first integral implies merely a very large set under consideration that includes species with the abundances many orders of magnitude lower than the abundance of water, so that $\mathcal{N} \rightarrow \infty$ when $\mathfrak{R}_M \rightarrow 0$, in compliance with Equation (23).

A tighter condition for y follows from our above finding that the mass lost per orbit by all known outgassing species, including water, was 175% of the mass loss of water, which implies $y = 0.636$ for the lower limit to y , as depicted in Figure 14. Since most data points in the figure congregate along $y \simeq 0.5$, their distribution is inconsistent with the required law and suggests that the set is substantially incomplete. A fit through the three most abundant species — water, carbon monoxide, and carbon dioxide — predicts that $y = 0.72 \pm 0.12$. Combining the constraints, a probable range for the relative loss of mass by outgassing per orbit of C/1995 O1 amounts to $2 \lesssim \mathfrak{R}_\infty \lesssim 5$, so that water ice may account for as little as ~20% of the orbit-integrated outgassed mass. If the

cumulative distribution of sublimating species does follow a power law, their number with mass loss per orbit greater than 10% of the water mass loss is predicted to be between four and seven (compared to three known); those with \mathfrak{R}_M greater than 1%, between 21 and 46 (compared to 9 known, an incompleteness of more than 50%); those with \mathfrak{R}_M greater than 0.1%, between 100 and ~320 (compared to 17 known, an incompleteness of 83–95% or a factor of about 6 to 19); and those with \mathfrak{R}_M greater than 0.01%, between ~460 and ~2150 (compared to 21 known, an incompleteness by a factor of 22 to 100). For this last \mathfrak{R}_M limit, the number of species to outgas from the nucleus equals ~760, if $y = 0.72$.

These findings suggest that in terms of the total loss of mass from C/1995 O1 by outgassing, water ice contributes at best about 50% and may contribute as little as 20%, although this last estimate is only a crude limit. A broad variety of compounds, mostly organic, account for the rest; many of them may have a molecular mass substantially greater ($\mathfrak{R}_\mu \gg 1$), and their equivalent sublimation time longer ($\mathfrak{R}_\mathfrak{S} > 1$), than water, so that summarily they could contribute to the comet's total mass loss per orbit by outgassing much more than implied by their production-rate ratio \mathfrak{R}_Q . In addition, one cannot rule out that C/1995 O1 carried many hundreds of parent molecules with a mass-loss ratio $\mathfrak{R}_M > 10^{-3}$ and perhaps more than a thousand with $\mathfrak{R}_M > 10^{-4}$.

We next compare this predicted variety of species in C/1995 O1 with the number of diverse molecular formulas generated as a sum of all possible combinations of specific elements and subject to prescribed assumptions. Disregarding for a moment the chemical issues and excluding the homonuclear molecules, the number of mathematically possible compounds is a function of (i) a number N of the elements, $\mathcal{E}^{(i)}$ ($i=1, 2, \dots, N$), that make up the molecules and (ii) maximum numbers K_i of atoms, $\mathcal{E}_{k_i}^{(i)}$ ($k_i=0, 1, \dots, K_i$), that each of the elements contributes to the molecules. A general chemical formula of such compounds is

$$\mathcal{E}_{k_1}^{(1)} \mathcal{E}_{k_2}^{(2)} \dots \mathcal{E}_{k_N}^{(N)}; \quad (i=1, 2, \dots, N; k_i=0, 1, \dots, K_i), \quad (25)$$

where $k_i=0$ means that an i -th element does not contribute to the particular molecule. However, the exclusion of the homonuclear molecules requires that there always be at least two elements ($N>1$), i and $j \neq i$, in any molecule for which $k_i > 0$ and $k_j > 0$. The complete set of compounds is symbolically denoted as

$$\left[\mathcal{E}_{K_1}^{(1)} \mathcal{E}_{K_2}^{(2)} \dots \mathcal{E}_{K_N}^{(N)} \right] \quad (26)$$

and the number \mathcal{N} of mathematically possible molecular compounds is

$$\mathcal{N} = \prod_{i=1}^N (K_i + 1) - \left(1 + \sum_{i=1}^N K_i \right). \quad (27)$$

The molecules consisting of $N-1, N-2, \dots, 2$ elements that make up subsets of the set (26) are included in \mathcal{N} .¹⁴ Note that for $K_1=K_2=\dots=K_N=K$ Equation (27) is simplified to $\mathcal{N}=(K+1)^N-(1+KN)$. We next illustrate this exercise, including the chemical properties of the resulting compounds, on an example of a molecular set consisting of three elements, each of which contributes up to two atoms per molecule, $[\text{C}_2\text{H}_2\text{O}_2]$ ($N=3; K_C=K_H=K_O=2$), in Table 23; we show that, of the total number of compounds, $\mathcal{N}=(2+1)^3-(1+2 \times 3)=20$, fully 16 (80%) have been detected outside the Solar System, whereas 8 (40%) have been observed in C/1995 O1, five (25%) of them being parent molecules and the rest dissociation products. Two molecules seen in interstellar or circumstellar space have not been detected in the comet in spite of attempts to do so. Among the four compounds not observed in either environment is glyoxal;¹⁵ two of the three remaining ones — ethylenedione and ethynediolide (together with its isomer glyoxalide) — are derivatives of glyoxal (Dixon et al. 2016). The spectrum of solid glyoxal was found to have fundamental bands between $3.5 \mu\text{m}$ and $18.2 \mu\text{m}$ (Durig & Hannum 1971). The last undetected molecule is the hydrocarboxyl functional group COOH, of fleeting existence as a separate compound; it is contained in all carboxylic acids, one of which (formic acid) is listed in Table 23, while another (glyoxylic acid) is related to glyoxal; the oxalic acid has the formula of the group's dimer (Table 20).

¹⁴ If homonuclear molecules should be included among the mathematically possible compounds, then $N=1$ is allowed and Equation (27) changes to $\mathcal{N}=\prod_{i=1}^N (K_i+1)-(N+1)$.

¹⁵ From our standpoint, glyoxal is the most interesting among three $\text{C}_2\text{H}_2\text{O}_2$ isomers; the other two are acetylenediol HOCCOH and acetolactone H_2COCO .

Table 23

Molecular Species Made Up of Carbon, Hydrogen, and Oxygen With Up to Two Atoms of Each Element^a ($N=3, K=2$)

Atoms Per Element C H O			Molecule's Name	Formula	Molecule Detected ^b		
					Out-side ^c Solar System	in C/1995 O1 Any Parent Status	Only
Set $[\text{C}_2\text{H}_2\text{O}_2]$							
1	1	1	Formyl radical	HCO	●		
1	1	2	Hydrocarboxyl group	COOH			
1	2	1	Formaldehyde	H_2CO	●	●	
1	2	2	Formic acid	HCOOH	●	●	●
2	1	1	Ketonyl	HCCO	●		
2	1	2	Ethynediolide ^d	HOCCO			
2	2	1	Ketene	CH_2CO	●	○	○
2	2	2	Glyoxal	OCHCHO			
Subset $[\text{C}_2\text{H}_2]$							
1	1	0	Methylidyne radical	CH	●	●	
1	2	0	Methylene radical	CH_2	●		
2	1	0	Ethynyl radical	C_2H	●		
2	2	0	Acetylene	C_2H_2	●	●	●
Subset $[\text{C}_2\text{O}_2]$							
1	0	1	Carbon monoxide	CO	●	●	●
1	0	2	Carbon dioxide	CO_2	●	●	●
2	0	1	Dicarbon monoxide	C_2O	●		
2	0	2	Ethylenedione ^d	OCO			
Subset $[\text{H}_2\text{O}_2]$							
0	1	1	Hydroxyl radical	OH	●	●	
0	1	2	Hydroperoxyl	HO_2	●		
0	2	1	Water	H_2O	●	●	●
0	2	2	Hydrogen peroxide	HOOH	●	○	○

Notes.

^a Homonuclear molecules excluded.

^b Open circle in comet columns means the molecule was searched for but undetected.

^c In interstellar and/or circumstellar space; for original discovery reports, see https://en.wikipedia.org/wiki/List_of_interstellar_and_circumstellar_molecules.

^d Derivative of glyoxal; glyoxalide OHCCO, an isomer of ethynediolide, is yet another derivative (Dixon et al. 2016).

A total number of molecules detected in the interstellar medium up to now is about 200 — nearly 10 times the number of parent molecules observed in C/1995 O1 — with a peak molar mass well over 100 g mol^{-1} , either as gas or as ice. Some are radicals that could not exist in a cometary nucleus without being bound chemically to other, more stable ices. A majority of interstellar molecules are made up of up to five elements: carbon, hydrogen, oxygen, nitrogen, and sulfur. The number of hydrogen and carbon atoms seldom exceeds six each per molecule; oxygen rarely contributes more than two to three atoms per molecule, while the other elements mostly not more than one atom per molecule (see footnote c to Table 23). Under these conditions, a mathematically complete set, $[\text{C}_6\text{H}_6\text{O}_{2-3}\text{NS}]$, consists of $\mathcal{N} \approx 570\text{--}770$ diverse molecules. On the one hand, some of these formulas might not correspond to any chemical at all, others may not have the necessary thermophysical properties. On the other hand, this range of numbers

does not account for isomers (and polymers), whose tally should increase rapidly with both N and K_i . In fact, isomers exist even among the compounds presented in Table 23. In addition to the isomers of glyoxal, referred to above, there is hydroxymethylene (HCOH), an isomer of formaldehyde; ethynol (HC₂OH), an isomer of ketene; and dioxirane (H₂CO₂), an isomer of the formic acid.

If one expects a degree of analogy between the presence of complex molecules in the interstellar medium and in comets, and detection incompleteness by a factor of three to four in the interstellar medium on the assumption that a great majority of compounds complies with a symbolical formula [C₆H₆O₂₋₃NS] in Equation (26), then a degree of detection incompleteness of parent molecules in a comet like C/1995 O1 is estimated at a factor of ~ 20 – 30 or even more. It is worth remarking that the estimate for interstellar molecules is in line with our nominal estimate of ~ 760 volatile species in C/1995 O1 whose mass loss is greater than 0.01% of the water mass loss, based on the data in Figure 14. In any case, the present inventory of parent molecules in C/1995 O1 appears to be extremely incomplete, by a factor much greater than 10, and the mass loss of water is quite probably less than 50% of the total outgassed mass lost per orbit. The conclusion on the existence of hundreds of very complex molecules that contribute to the process of outgassing from comets is also broadly consistent with very recent results from the Rosetta Mission, which suggest that carbon in dust particles from comet 67P/Churyumov-Gerasimenko is bound in organic matter of high molecular weight (Fray et al. 2016) and which support the presence of polyoxymethylene (POM) and other polymers in the dust grains as a plausible source of organic matter in gaseous phase, such as formaldehyde (Wright et al. 2015). A potential presence of polycyclic aromatic hydrocarbons (PAHs), such as phenanthrene, anthracene, etc., as discussed by Bockelée-Morvan et al. (2004) and others, would only strengthen this general conclusion.

Finally, as a caveat to our findings, we remark that the values of the nominal orbit-integrated production ratio, \mathfrak{R}_{\odot} (as listed in Table 20), are, in general, a function of the temperature distribution over the nucleus' surface. If the isothermal model that we apply does not provide a satisfactory approximation to the true sublimation law, the constant in Equation (3) for the scaling distance r_0 changes. The scaling distances of the preperihelion and post-perihelion sublimation curves of water ice listed in Table 19 as derived from the observed production-rate data, would be fitted decidedly better by choosing for the constant a value of $24\,200 \text{ AU}^{\frac{1}{2}}$ rather than $19\,100 \text{ AU}^{\frac{1}{2}}$. This correction would reduce \mathfrak{R}_{\odot} (and therefore \mathfrak{R}) by some 10% to 15%, but would not fundamentally change our above conclusion about the systematic trend in \mathfrak{R} relative to water. However, the unexpectedly high production rates of water at heliocentric distances larger than 3 AU might be attributed to sublimation from icy dust grains, with no effect on the constant in Equation (3).

9.5. Production of Dust and Its Mass Loading of the Gas Flow

Further insight into the issue of the mass lost over the orbit by outgassing is provided by investigating the mass-loss rates of dust and by examining the terminal velocities of dust particles. Since it is well known that, owing

to a fairly flat particle-size distribution, the large-sized dust (submillimeter and larger grains) provides a dominant contribution to the total particulate mass lost, we focus on the investigations of C/1995 O1 based on imaging observations at submillimeter and larger wavelengths.

Jewitt & Matthews (1999) observed the comet at $850 \mu\text{m}$ on 16 dates in 1997 between February 9 (1.27 AU pre-perihelion) and October 24 (3.17 AU post-perihelion), deriving a dust mass-loss rate of $(1.6 \pm 0.5) \times 10^9 \text{ g s}^{-1}$ at 1 AU before perihelion and $(1.8 \pm 0.4) \times 10^9 \text{ g s}^{-1}$ at 1 AU after perihelion, and an orbit-integrated mass loss of $3 \times 10^{16} \text{ g}$, equivalent to the mass of a comet more than 5 km in diameter, at an assumed density of 0.4 g cm^{-3} . They employed a blackbody approximation and a model of an optically thin, spherically symmetrical, steady-state coma, by-passing the particle-size distribution function by adopting a dust opacity of $0.55 \text{ cm}^2 \text{ g}^{-1}$ at $850 \mu\text{m}$. They equated the mass production rate with a ratio of the particles' mass to their residence time in the beam. However, the residence time depends not only on the ejection speed of the particles (and therefore on their size), but also on the direction of their motion relative to the observer. In particular, particles moving in directions close to the line of sight have a residence time much longer than particles moving perpendicular to the line of sight, a scenario considered by Jewitt & Matthews (1999). Sekanina & Kracht (2014) developed a technique that properly accounts for the effect of residence time in a spherically symmetrical, steady-state coma environment, also employing a more realistic approximation for the particle velocity. This technique relates a total mass production rate of dust at time t ,

$$\dot{\mathcal{M}}_d(t) \equiv \dot{\mathcal{M}}_d(s_0, s_\infty) = \dot{N}_d(t) \int_{s_0}^{s_\infty} \frac{4}{3} \pi \rho_d s^3 f_d(s) ds, \quad (28)$$

and a geometric cross-sectional area of all dust particles (of assumed sphericity) ejected from the nucleus that at time t reside in a beam whose radius at the comet is r_b ,

$$X_{d,r_b} \equiv X_{d,r_b}(s_0, s_\infty) = \int_{s_0}^{s_\infty} \pi s^2 f_d(s) ds \int_{-\infty}^t \dot{N}_d(t) \Phi(s, t; r_b) dt, \quad (29)$$

where $f_d(s) ds$ is a normalized distribution function of particle radii s whose lower and upper limits are, respectively, s_0 and s_∞ , ρ_d is a particle bulk density, $\dot{N}_d(t)$ is the number of particles released at t per unit time, and $0 \leq \Phi(s, t; r_b) \leq 1$ is a function extracting the beam grains.

The cross-sectional area of the dust in the beam is measured either from the scattered light (in the visible spectrum) or, as done by Jewitt & Matthews (1999), from the thermal emission. In the former case, it is the particles' scattering properties (such as an albedo and phase function) that complicate the problem, in the latter case it is the particles' emissivity $\varepsilon_d \leq 1$.

In the case of far infrared or submillimeter observations at wavelength λ , the information provided by the measured thermal flux density \mathcal{F}_λ in the beam is

$$\mathcal{F}_\lambda \sim \int_{s_0}^{s_\infty} \varepsilon_d(s) \pi s^2 f_d(s) ds \int_{-\infty}^t \dot{N}_d(t) \Phi(s, t; r_b) dt, \quad (30)$$

but since a variation with particle size of the emissivity at λ is unknown, the flux density is interpreted in terms of a blackbody's cross-sectional area, that is, it is assumed

that $\varepsilon_d(s)=1$ for any s between s_0 and s_∞ . And since particles whose radii s satisfy a condition

$$x = \frac{2\pi s}{\lambda} \ll 1 \quad (31)$$

do not radiate efficiently and $\lim_{s \rightarrow 0} \varepsilon_d(s)=0$, the true geometric cross-sectional area of the particles in the beam should in fact be much greater than offered by the flux-density measurement. To account for the effect of emissivity, we note that there must exist particle sizes $s_{\min} > s_0$ and $s_{\max} \leq s_\infty$ such that

$$\int_{s_0}^{s_\infty} \varepsilon_d(s) \pi s^2 \phi_d(s) ds = \int_{s_{\min}}^{s_{\max}} \pi s^2 \phi_d(s) ds = X_d(s_{\min}, s_{\max}), \quad (32)$$

where $\phi_d(s)$ equals $f_d(s) \int_{-\infty}^t \dots dt$ from Equation (30) and X_d is the measured blackbody cross-sectional area. This formalism approximates the unknown variations in $\varepsilon_d(s)$ by introducing discontinuities at s_{\min} and s_{\max} , with $\varepsilon_d(s) = 0$ at $s_0 \leq s < s_{\min}$ and $s_{\max} \leq s \leq s_\infty$, but with $\varepsilon_d(s) = 1$ at $s_{\min} \leq s \leq s_{\max}$. In the case examined here one can safely adopt $s_{\max} = s_\infty$. If the variations in the emissivity can, for example, plausibly be approximated by $\varepsilon_d \sim x$ for $x < x_0$ and by $\varepsilon_d \simeq 1$ for $x \geq x_0$, their total effect is accounted for by taking $2\pi s_{\min}/\lambda \simeq \frac{1}{2}x_0$, that is, $s_{\min} \simeq \lambda x_0/4\pi$. As x_0 is near unity, for submillimeter wavelengths this condition implies that $s_{\min} \gg s_0$, which greatly affects the results, as seen below.

Based on the work by Sekanina & Kracht (2014), the relationship between the total mass production rate of dust and the cross-sectional area $X_d(s_{\min}, s_{\max})$ is then

$$\dot{M}_d = \frac{8\rho_d}{3\pi r_b} X_d(s_{\min}, s_{\max}) \frac{\int_{s_0}^{s_\infty} s^3 f_d(s) ds}{\int_{s_{\min}}^{s_{\max}} \frac{1}{v_d(s)} s^2 f_d(s) ds}, \quad (33)$$

where $v_d(s)$ is a size-dependent ejection velocity of the dust particles that generally is a function of heliocentric distance. We adopt a power law for the size distribution,

$$f_d(s) ds = C \left(\frac{s_0}{s}\right)^\alpha, \quad \int_{s_0}^{s_\infty} f_d(s) ds = 1, \quad (34)$$

where α is the distribution's index or power and C is a normalization constant; and make use of an expression previously employed for the ejection velocity (Sekanina & Kracht 2014),

$$v_d(s) = \frac{v_0}{1 + \chi\sqrt{s}} \quad (35)$$

with v_0 and χ being the parameters, v_0 potentially varying with heliocentric distance. The total mass production rate is then as follows

$$\begin{aligned} \dot{M}_d &= \frac{8v_0\rho_d s_\infty}{3\pi r_b} \frac{(3-\alpha)(\frac{7}{2}-\alpha)}{4-\alpha} \left(\frac{s_\infty}{s_{\max}}\right)^{3-\alpha} \\ &\times (1 - \epsilon_\infty^{4-\alpha}) X_d(s_{\min}, s_{\max}) \\ &\times \left[\left(\frac{7}{2}-\alpha\right)(1 - \epsilon^{3-\alpha}) + (3-\alpha)(1 - \epsilon^{\frac{7}{2}-\alpha}) \chi\sqrt{s_{\max}} \right]^{-1}, \end{aligned} \quad (36)$$

where $\epsilon_\infty = s_0/s_\infty$, $\epsilon = s_{\min}/s_{\max}$, and $\alpha \neq 3, \frac{7}{2}$, and 4; otherwise the powers of s_∞ , s_{\max} , ϵ_∞ , and/or ϵ should be replaced with the respective logarithms.

Before we apply Equation (36) to Jewitt & Matthews' (1999) set of the cross-sectional data, we carefully select the model parameters. We first focus on the constants that define the size distribution function, to which the results are most sensitive. The index α was for C/1995 O1 determined numerous times and in different ways; a useful compilation, published by Lasue et al. (2009), shows that $3.0 \leq \alpha \leq 3.7$. The entries most relevant to the important submillimeter and larger particles were provided by the investigations based, at least in part, on the ISO observations, whose spectral reach extended to nearly 200 μm . Min et al. (2005) derived $\alpha = 3.48$ from the ISO observations made in September 1996, about six months before perihelion, while Harker et al. (2002) deduced from the observations covering nine months that $\alpha = 3.4$ in 1996 when the comet was nearly 3 AU from the Sun on its way to perihelion, but $\alpha = 3.7$ when the comet was within three months of perihelion. These numbers are in good agreement with an earlier result by Grün et al. (2001), who derived $\alpha = 3.5$.¹⁶ We adopt $\alpha = 3.55$ as an optimum mean value; we estimate its error at ± 0.15 .

A lower boundary to the particle size distribution, s_0 , has a negligible effect on the mass production rate; we employ $s_0 = 0.01\mu\text{m}$, since Min et al. (2005) showed that incorporating grains of amorphous olivine and pyroxene of this minute size improves a fit to the comet's observed spectral energy distribution.

An upper boundary to the size distribution, s_∞ , influences the total mass production rate much more significantly than the lower boundary. We assume that the largest particles must reach an escape velocity from the nucleus at the time they decouple from the gas flow, which according to Probst (1969) is at a distance of ~ 20 nucleus' radii. The size of the nucleus is among the subjects of Part II of this study; here we only mention that Szabó et al.'s (2012) results suggest that at the relevant distance the escape velocity amounts to $v_{\text{esc}} \simeq 4 \text{ m s}^{-1}$. From Equation (35) the particle radius at the upper boundary of the size distribution function is then equal to

$$s_\infty = \left(\frac{v_0}{v_{\text{esc}}} - 1\right)^2 \chi^{-2}, \quad (37)$$

so that this task is reduced to finding the particle velocity parameters v_0 and χ .

Jewitt & Matthews (1999) calculated that the velocity of particles 1 mm in radius ejected from C/1995 O1 was 80 m s^{-1} at 1 AU from the Sun (although they eventually used a value three times *lower*), assuming that the diameter of the nucleus equaled 40 km. With its dimensions nearly twice as large (Szabó et al.'s 2012), the ejection velocity of the millimeter-sized particles was more likely to amount to at least 110 m s^{-1} . In fact, Vasundhara & Chakraborty's (1999) direct fit to dust-coma features in the comet's images taken between 1997 February 18 and May 2 imply for these particles ejection velocities that are still higher, 123–145 m s^{-1} .

¹⁶ Both Grün et al. (2001) and Harker et al. (2002) used a size distribution law that was introduced by Sekanina & Farrell (1982) and subsequently employed extensively by Hanner (e.g., Hanner 1983, 1984). The Sekanina-Farrell law differs from a power law for submicron- and micron-sized grains, but in terms of α both laws are practically identical for submillimeter-sized and larger particles.

Table 24

Total Mass Production Rates of Dust, $\dot{\mathcal{M}}_d$, for C/1995O1 From Submillimeter Observations by Jewitt & Matthews (1999)

Time of Observation 1997 (UT)	Distance to Sun (AU)	Blackbody Cross-Section (10^{14}cm^2) ^a	Dust Rate $\dot{\mathcal{M}}_d$ (10^8g s^{-1})			
			Nominal	$s_{\min} = s_0$	J&M	
Feb. 9.05	1.271	2.6	15.8	0.63	10	
	16.98	1.186	3.1	21.2	0.84	13
Mar. 9.92	0.997	2.7	24.7	0.98	16	
	23.00	0.932	2.6	25.8	1.02	16
Apr. 6.92	30.83	0.915	2.6	25.5	1.01	17
	0.920	2.9	27.1	1.07	18	
May 2.23	26.82	1.023	3.8	27.8	1.10	18
	1.062	3.4	23.3	0.92	15	
June 14.92	6.21	1.103	3.3	21.3	0.84	14
	12.22	1.161	4.3	25.7	1.02	16
July 6.92	1.558	2.8	11.5	0.46	7	
	1.836	3.1	10.7	0.43	7	
Sept. 9.92	2.644	3.5	8.9	0.35	6	
	13.92	2.692	2.5	6.3	0.25	4
Oct. 13.71	3.044	0.88	2.0	0.08	1.3	
	24.68	3.170	0.81	1.8	0.07	1.2

Note.

^a Relative errors from $\pm 8\%$ to $\pm 33\%$.

At the other end of the dust-particle size spectrum, the ejection velocities of submicron-sized grains that made up the leading boundaries of recurring expanding halos were determined by Braunstein et al. (1999) from images taken over a period of 61 days and approximately centered on perihelion. Corrected for the projection effects, the ejection velocities averaged $670 \pm 70 \text{ m s}^{-1}$, ranging from 603 m s^{-1} to 775 m s^{-1} , with no systematic trends between 0.91 AU and 1.10 AU from the Sun. Vasundhara & Chakraborty (1999) derived the ejection velocities of up to 650 m s^{-1} for submicron-sized particles near 1 AU, with a rate of decrease with heliocentric distance r only slightly steeper than $r^{-\frac{1}{2}}$ (to be adopted here). To reconcile these high ejection velocities of microscopic grains with the velocities of $130\text{--}140 \text{ m s}^{-1}$ for millimeter-sized particles, the parameters in Equation (35) should equal, after rounding off, $v_0 = 700 \text{ m s}^{-1}$ at 1 AU from the Sun and $\chi = 13 \text{ cm}^{-\frac{1}{2}}$.

With these values and an escape velocity of $\sim 4 \text{ m s}^{-1}$ inserted into Equation (37), the upper boundary of the particle size distribution is at $s_\infty = 180 \text{ cm}$. Referring to our previous arguments, we adopt this same number for s_{\max} , while with a rather conservative value of $x_0 \approx 1.2$ (x_0 is expected to be near unity), we find $s_{\min} = 80 \mu\text{m}$.

The remaining physical parameter in Equation (36) — a particle bulk density — is rather uncertain, because available information is indirect, based on research of comets other than C/1995 O1. Exposure of Stardust’s sample collector to impacts of dust grains ejected from 81P/Wild 2 points to a very broad range of bulk densities, from compact particles with $\rho_d \sim 3 \text{ g cm}^{-3}$ to highly porous aggregates for which ρ_d is as low as $\sim 0.3 \text{ g cm}^{-3}$ (e.g., Hörz et al. 2006). A recent investigation of the dust detected by the *Grain Impact Analyzer and Dust Accumulator* (GIADA) on board the Rosetta spacecraft led to a conclusion that for 67P/Churyumov-Gerasimenko a mean dust-particle bulk density equals $0.80^{+0.84}_{-0.07} \text{ g cm}^{-3}$ (Fulle et al. 2016). We henceforth adopt $\rho_d = 0.8 \text{ g cm}^{-3}$.

With the known angular beam radius of $7''.65$, the linear radius becomes $r_b = 5550\Delta \text{ km}$, where Δ is the comet’s geocentric distance in AU. This completes the prerequisites for deriving the total mass production rates of dust, which are in Table 24 listed in a column marked “Nominal” and compared with the numbers by Jewitt & Matthews (1999), in the “J&M” column, and with the rates derived in a case of the neglected emissivity effect (in a column marked “ $s_{\min} = s_0$ ”).

Table 24 suggests an unexpectedly good correspondence between our nominal mass production rates and the rates determined by Jewitt & Matthews (1999); our solution offers rates that, on the average, are only 1.55 times higher than are theirs. We are convinced that this agreement is fortuitous, in part because the enormous differences between both approaches are demonstrated by the employed ejection velocity: our value of 137 m s^{-1} for grains 1 mm in radius, is a factor of 5.5 times higher than the value used by Jewitt & Matthews. According to their Equation (6), our nominal rates should have been higher by the same factor. In addition, the maximum radius of the particles escaping from the nucleus in their model was $\sim 3 \text{ cm}$, while our estimate is 60 times larger, a factor that also increases the production rate as seen from our Equation (36). This means that some of the other quantities that impact the resulting rates must have been strongly underestimated by Jewitt & Matthews (1999), one of them being the residence times of grains moving in directions other than perpendicular to the line of sight, as pointed out by us earlier.

Comparison of the columns 4 and 5 in Table 24 illustrates that ignoring the effect of low emissivity for particles smaller than about 0.1 the wavelength yields unacceptable results. In this case, assigning improperly a unit emissivity to grains as small as 10^{-5} the wavelength implies the dust production rates that are too low by a factor of about 25.

As for the uncertainties involved in our nominal mass production rates in Table 24, we note that they are most sensitive to the size distribution index α . The error of ± 0.15 brings about a scatter from 0.57 the nominal rate for $\alpha = 3.7$ to 1.65 the nominal rate for $\alpha = 3.4$. The uncertainties in the other parameters are of lesser impact. A change by a factor of two in a particle size at the upper boundary of the distribution, s_∞ , results in a range from 0.77 to 1.31 the nominal rate. The same change in a particle size at the distribution’s lower boundary, s_0 , has an entirely negligible effect on the production rates, but a change in the lower limit of the size of the particles that contribute to the measured thermal flux density, s_{\min} , does affect the rates moderately; a change by a factor of two causes the rates to vary from 0.87 to 1.15 the nominal rate. The column $s_{\min} = s_0$ in Table 24 shows a change in the rates after the nominal value of s_{\min} was reduced by a factor of 8000. Equation (36) implies that changes in the particle density and ejection velocity project linearly as changes in the production rate (disregarding a minor effect from the parameter χ).

The next tasks were to test whether the mass production variations of dust with time could be fitted by the same g_{mod} -type law as the gas production variations; to estimate a total loss of dust mass from C/1995 O1, derived by integrating this production rate $\dot{\mathcal{M}}_d$ over the orbit from aphelion to next aphelion; and to compare

Table 25
Loss of Dust Mass and Dust-to-Water Mass-Loss Ratio
for Comet C/1995 O1

Parameter	Value	
Particle size distribution index, α	3.55	
Size distribution boundaries:		
Particle radius at lower end, s_0 (μm)	0.01	
Particle radius at upper end, s_∞ (m)	1.80	
Particles contributing to measured thermal signal:		
Minimum particle radius, s_{\min} (μm)	80	
Maximum particle radius, s_{\max} (m)	1.80	
Particle ejection velocity:		
Parameter v_0 at 1 AU (km s^{-1})	0.70	
Parameter χ ($\mu\text{m}^{-\frac{1}{2}}$)	0.13	
Power γ of heliocentric-distance variation, $r^{-\gamma}$	0.50	
Bulk density of particles, ρ_d (g cm^{-3})	0.80	
	Before Perihelion	After Perihelion
Number of observations used	7 ^a	9 ^b
Distances from Sun (AU)	4.58–0.92	0.92–3.17
Scaling distance $(r_0)_d$ (AU)	6.28 ± 0.11	5.31 ± 0.12
Dust-mass production rate at 1 AU from Sun (10^8 g s^{-1})	24.0 ± 3.5	29.5 ± 4.9
Integral $\frac{1}{2}\mathfrak{S}_{\text{pre}}$ or $\frac{1}{2}\mathfrak{S}_{\text{post}}$ (days)	88.5	85.1
Dust mass lost per half orbit (g)	1.8×10^{16}	2.2×10^{16}
Dust loading of water flow at 1 AU from Sun, $\Psi_{\text{H}_2\text{O}}^{(0)}$	11.3	10.9
Dust loading of water flow per half orbit	12.0	11.6
	Aphelion to Next Aphelion	
Dust mass lost per orbit (g)	4.0×10^{16}	
Dust loading of water flow per orbit, $\Psi_{\text{H}_2\text{O}}^*$	11.8	

Notes.

^a Based on 5 nominal dust mass production rates from Table 24 combined with 2 adjusted data points by Grün et al. (2001); orbital arc covered by Jewitt & Matthews' (1999) observations alone too short to determine scaling distance.

^b Based on nominal dust mass production rates from Table 24 except for anomalously high ones from September 9 and 13 (outburst?), which had to be eliminated; fit used to adjust Grün et al.'s rates.

it to the mass loss of water presented in Table 19. We began by ascertaining that the more extensive set of the post-perihelion nominal data points from Table 24 is satisfied by a law $g_{\text{mod}}[r; (r_0)_{d,\text{post}}]$ and by determining the tabulated scaling distance $(r_0)_{d,\text{post}}$. We then turned to the preperihelion data in Table 24, which cover a shorter range of heliocentric distances. We noticed that, fortunately, Grün et al. (2001) reported the dust production rates at three larger heliocentric distances in 1996 and 1997, derived from the ISO observations. The chronologically last of these data points, from 1997 December 30, when the comet was 3.90 AU from the Sun, was used by us to adjust Grün et al.'s scale of dust production to agree with ours. It turned out that when their production rate at 3.9 AU was multiplied by a factor of 1.3, it fitted the value predicted for this time by the post-perihelion modified law. We then adjusted Grün et al.'s (2001) preperihelion data points, referring to 1996 April 27 (the comet at 4.58 AU from the Sun) and to 1996 October 7 (2.82 AU from the Sun) by the same factor, and linked them with the five preperihelion nominal production rates from Table 24; we obtained a rather satisfactory fit by apply-

ing another modified law, $g_{\text{mod}}[r; (r_0)_{d,\text{pre}}]$.¹⁷ Together with a summary of the adopted parameters, the dust-production results are listed in Table 25, separately for either orbital branch as well as for the whole orbit.

We found that the orbit-integrated mass loss of dust by C/1995 O1 equaled 4×10^{16} g, close to — but slightly higher than — the total by Jewitt & Matthews (1999). The dust production appears to be only marginally, and within 1σ errors, higher after perihelion than before perihelion. Figure 15 illustrates that the data points are fitted by the two g_{mod} -type laws quite satisfactorily. However, we would not expect the laws to be applicable to heliocentric distances larger than approximately 4.5 AU. The production rate of carbon monoxide catches up with the water production rate at 3.6–3.7 AU, thus gradually taking control over the process of dust release, including non-sublimating water-ice grains, at larger distances from the Sun.

The mass ratio of the production of dust to the production of water is called in Table 25 and hereafter a *mass loading of the water flow by dust* or shortly a *dust loading of the water flow*. We distinguish a *normalized dust loading*, $\Psi_{\text{H}_2\text{O}}^{(0)}$, given as

$$\Psi_{\text{H}_2\text{O}}^{(0)} = \frac{\text{mass production rate of dust at 1 AU from Sun}}{\text{mass production rate of water at 1 AU from Sun}}, \quad (38)$$

whose values are different before and after perihelion; and a dust loading integrated over the orbit, or simply a *dust loading per orbit* or *integrated dust loading*, $\Psi_{\text{H}_2\text{O}}^*$, defined as

$$\Psi_{\text{H}_2\text{O}}^* = \frac{\text{total mass of dust lost by ejection per orbit}}{\text{total mass of sublimated water ice per orbit}}, \quad (39)$$

which consists of the preperihelion and post-perihelion contributions to the total. When data are limited to a heliocentric distance r different from 1 AU, one may only be able to determine a *nominal dust loading*, $\Psi_{\text{H}_2\text{O}}(r)$, at that particular distance, which — assuming the validity of a g_{mod} -type law for both water and dust — is related to the normalized dust loading by

$$\Psi_{\text{H}_2\text{O}}(r) = \Psi_{\text{H}_2\text{O}}^{(0)} \left[\frac{(r_0)_d^n + 1}{(r_0)_{\text{H}_2\text{O}}^n + 1} \frac{(r_0)_{\text{H}_2\text{O}}^n + r^n}{(r_0)_d^n + r^n} \right]^k, \quad (40)$$

where n and k are the exponents of the modified law, as defined below Equation (1), while $(r_0)_d$ and $(r_0)_{\text{H}_2\text{O}}$ are, respectively, the scaling distances for the dust (from Table 25) and water (from Table 19), which both apply to either the preperihelion or post-perihelion branch of the orbit, as do the values of the nominal and normalized dust loading of the water flow.

¹⁷ Additional observations of the comet in a spectral range (near or beyond 1 mm) that should warrant a proper account of the contributions from massive grains were reported by Senay et al. (1997) at three wavelengths between 1.1 mm and 2.1 mm in late February 1997 and by de Pater et al. (1998) at wavelengths 2.6–3.5 mm and 7.0–13.3 mm during March and April 1997. We do not use these observations in our computations because they cover the same period of time as the nominal data points in Table 24, but note that Senay et al. derived a fairly low production rate of $3.2 \times 10^8 \text{ g s}^{-1}$ five weeks before perihelion, while de Pater et al. deduced a production rate on the order of 10^9 g s^{-1} within four weeks of perihelion, in conformity with the data we employ.

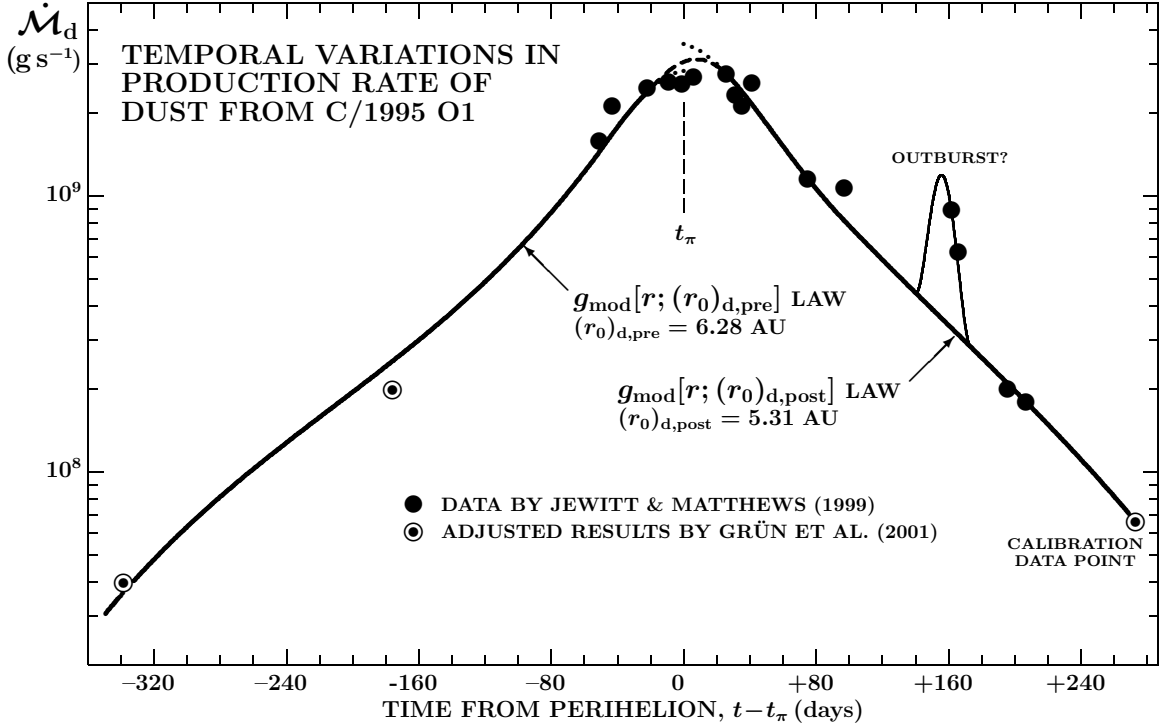


Figure 15. Curve of the dust production rate of C/1995 O1 as a function of time. It was derived using the technique described in the text, applied to the dust cross-sectional data at a submillimeter wavelength (Jewitt & Matthews 1999), which were linked to the adjusted ISO-based production rates by Grün et al. (2001), and fitted by a modified law, $g_{\text{mod}}[r; (r_0)_d]$, separately before and after perihelion (thick curve). Of the 11 Jewitt-Matthews post-perihelion data points, 9 were successfully matched by a g_{mod} law, the two discarded ones possibly suggesting the presence of a minor outburst some 160 days after perihelion. The data point by Grün et al. (2001) at 3.90 AU from the Sun (+273 days from perihelion) was employed to calibrate their other observations; it required a multiplication factor of 1.3 to fit the g_{mod} curve. The preperihelion data by Grün et al. at 4.58 AU and 2.82 AU from the Sun were then adjusted by this factor, linked to the other five preperihelion data points, and all subsequently fitted by a g_{mod} law, as depicted in the figure. At perihelion the two laws are disconnected, the post-perihelion production rate being nominally 23% higher than the preperihelion rate, as illustrated by the dots. This discrepancy is bridged by an empirical dashed curve, peaking shortly after perihelion.

A logarithmic differentiation of Equation (40),

$$\frac{d \ln \Psi_{\text{H}_2\text{O}}(r)}{d \ln r} = \frac{nk r^n [(r_0)_d^n - (r_0)_{\text{H}_2\text{O}}^n]}{[(r_0)_d^n + r^n] [(r_0)_{\text{H}_2\text{O}}^n + r^n]}, \quad (41)$$

implies that it is the difference between the scaling distances of the g_{mod} laws for the production of dust and water, respectively, that exclusively determines whether the dust loading increases or decreases with heliocentric distance: when the scaling distance for the dust production is greater, as is the case for C/1995 O1 both before and after perihelion, the dust loading increases with increasing distance from the Sun. However, $\Psi_{\text{H}_2\text{O}}$ does not diverge, as $\lim_{r \rightarrow \infty} d\Psi_{\text{H}_2\text{O}}/dr = 0$. The limit, equaling

$$\lim_{r \rightarrow \infty} \Psi_{\text{H}_2\text{O}}(r) = \Psi_{\text{H}_2\text{O}}^{(0)} \left[\frac{(r_0)_d^n + 1}{(r_0)_{\text{H}_2\text{O}}^n + 1} \right]^k \simeq \Psi_{\text{H}_2\text{O}}^{(0)} \left[\frac{(r_0)_d}{(r_0)_{\text{H}_2\text{O}}} \right]^{nk}, \quad (42)$$

is to be employed in practice with caution because of the aforementioned transformation of the dust ejection process from a water dominated mode to a carbon-monoxide dominated mode near 4 AU from the Sun.

Table 25 suggests that our results for both the normalized and integrated dust loading of the water flow range between about 11 and 12 and that they are at most only marginally higher prior to perihelion. The parameters

from Tables 19 and 25 allow one to predict the mass loading by dust of the water flow, $\Psi_{\text{H}_2\text{O}}(r)$, as well as that of the combined flow of water and carbon monoxide, $\Psi_{\text{H}_2\text{O}+\text{CO}}(r)$, and of water, carbon monoxide, and carbon dioxide, $\Psi_{\text{H}_2\text{O}+\text{CO}+\text{CO}_2}(r)$, for a broad variety of heliocentric distances r . The results of these computations, in Table 26, show that the dust loading increases systematically, both before and after perihelion, only for the flow of water. Once we consider a more realistic case, a combined flow of water with other species, the dust loading peaks and then may drop at larger heliocentric distances. This behavior is a corollary of Equation (41) written for a flow or more than one species, because the scaling distance of dust is smaller than the scaling distances of carbon monoxide and carbon dioxide both before and after perihelion. We note that in the case of a combined flow of water, carbon monoxide, and carbon dioxide, which in Table 26 approximates the true conditions in the comet's atmosphere most closely, the dust loading never exceeds 11 before perihelion and 10 after perihelion. The table also allows one to derive a dust loading of a flow of carbon monoxide, Ψ_{CO} , and of carbon dioxide, Ψ_{CO_2} :

$$\begin{aligned} \Psi_{\text{CO}}(r) &= \left[\Psi_{\text{H}_2\text{O}+\text{CO}}^{-1}(r) - \Psi_{\text{H}_2\text{O}}^{-1}(r) \right]^{-1} \\ \Psi_{\text{CO}_2}(r) &= \left[\Psi_{\text{H}_2\text{O}+\text{CO}+\text{CO}_2}^{-1}(r) - \Psi_{\text{H}_2\text{O}+\text{CO}}^{-1}(r) \right]^{-1}. \end{aligned} \quad (43)$$

Table 26

Nominal Mass Loading by Dust of Gas Flows in C/1995 O1

Distance from Sun, r (AU)	Dust Loading of Gas Flow Pre- and Post-Perihelion					
	$\Psi_{\text{H}_2\text{O}}(r)$		$\Psi_{\text{H}_2\text{O}+\text{CO}}(r)$		$\Psi_{\text{H}_2\text{O}+\text{CO}+\text{CO}_2}(r)$	
	pre	post	pre	post	pre	post
1.0	11.3	10.9	8.6	8.9	7.6	7.5
1.5	11.4	11.0	8.7	9.0	7.6	7.6
2.0	11.8	11.5	8.9	9.3	7.7	7.8
2.5	13.0	13.0	9.4	9.5	8.1	8.2
3.0	15.8	16.8	10.6	11.8	8.9	9.0
3.5	22.4	25.8	12.6	13.8	10.1	9.4
4.0	38.0	46.3	14.5	13.3	10.7	7.8
4.5	75.5	90.1	13.9	8.7	9.5	4.7

Before comparing the numbers in Table 26 with the results reported elsewhere, a caveat first. Whereas care is usually taken, as it should, to clearly distinguish between a dust loading of the *water* flow, $\Psi_{\text{H}_2\text{O}}$, on the one hand and a dust loading of the *gas* flow (that is, of the total flow of a number of volatile species), Ψ_{gas} ($\Psi_{\text{gas}} < \Psi_{\text{H}_2\text{O}}$), on the other hand, the two quantities are not always differentiated (e.g., A’Hearn et al. 1995; Schleicher et al. 1997), apparently with a tacit, but — as seen from Table 26 — rather questionable, premise that water dominates the sublimation process.

A high mass loading by dust in C/1995 O1 was commented on by numerous researchers. With one exception, the reported values of the dust loading based on the observations at submillimeter and millimeter wavelengths are in good to excellent agreement with the numbers in Table 26. The exception is an observation at wavelengths between 1.1 mm and 2.1 mm in late February 1997, five weeks before perihelion, by Senay et al. (1997), who reported for $\Psi_{\text{H}_2\text{O}}$ a fairly low value of 3.5. On the other hand, Jewitt & Matthews (1999), whose data we employ extensively, estimated a lower limit to $\Psi_{\text{H}_2\text{O}+\text{CO}}$ at 5 close to perihelion; having accounted for the contribution from carbon monoxide as a fifth of the contribution from water, they effectively estimated a lower limit to $\Psi_{\text{H}_2\text{O}}$ at 6. For greater heliocentric distances, the dust loading was reported by Grün et al. (2001) to equal 9 at 4.58 AU before perihelion, 6 at 2.82 AU before perihelion, and 10 at 3.90 AU after perihelion. For the gas production they employed the combined rate of water and carbon monoxide. At 4.58 AU before perihelion we find from Table 19 a gas production rate of $3.0 \times 10^6 \text{ g s}^{-1}$ (15% H_2O , 85% CO), so that $\Psi_{\text{H}_2\text{O}+\text{CO}} \simeq 10$; at 2.82 AU before perihelion, $2.4 \times 10^7 \text{ g s}^{-1}$ (70% H_2O , 30% CO), so that $\Psi_{\text{H}_2\text{O}+\text{CO}} \simeq 6$; and at 3.90 AU after perihelion, $4.9 \times 10^6 \text{ g s}^{-1}$ (33% H_2O , 67% CO), so that $\Psi_{\text{H}_2\text{O}+\text{CO}} \simeq 10$, in excellent agreement with Grün et al. (2001). Since we adjusted their dust production rates by a factor of 1.3 in Figure 15, the dust loading of the $\text{H}_2\text{O}+\text{CO}$ flow with these numbers becomes 13, 8, and 13, respectively, still in good agreement, given that the uncertainty in Grün et al.’s dust production rates was estimated by the authors at a factor of two in the least.

Three investigations employed a dynamical approach, and in this case it was a dust loading of the total gas flow, Ψ_{gas} , that was determined. Fitting the dust morphological features in the head of C/1995 O1, Vasundhara &

Chakraborty (1999) determined a lower limit of 4.8 ± 1.4 to the dust loading from observations on three days between six weeks before perihelion and one month after perihelion. Applying a modified Probst-Finon method of analysis to the comet’s dust tail, Fulle et al. (1998) concluded that at heliocentric distances greater than ~ 4.4 AU preperihelion, during the CO-driven activity, the dust loading Ψ_{CO} must have been at least 5; they deduced a dust production rate of $8 \times 10^6 \text{ g s}^{-1}$ some 320 days before perihelion, about a factor of 5 below the curve in Figure 15. Table 19 suggests that the CO production rate was in fact near $2.7 \times 10^6 \text{ g s}^{-1}$, leading to a dust loading of only 3 with Fulle et al.’s (1998) dust production rate. From Table 26 we find $\Psi_{\text{CO}} \simeq 17$ at a distance of 4.5 AU. Fulle et al.’s dust rate estimate of $5 \times 10^5 \text{ g s}^{-1}$ in 1993, at a heliocentric distance of 13 AU implies $\Psi_{\text{CO}} \sim 100$. This value is probably much too high and only formally consistent with Sekanina’s (1996) conclusion that the dust loading of the CO flow must have been greater than 15 over a range of heliocentric distances centered on 6.7 AU, derived from low expansion rates of a sequence of spiral features observed in the comet’s head during the months immediately following discovery. These constraints suggest that the dust production rate varied, on the average, more steeply than r^{-5} between 13 AU and 6.7 AU and as approximately r^{-2} between 6.7 AU and 4.6 AU before perihelion.

Lisse et al. (1999) determined a dust production rate of $\sim 1.4 \times 10^8 \text{ g s}^{-1}$ and a dust loading of the gas flow of ~ 5 from a 5–13 μm spectral energy distribution on 1996 October 31, when the comet was 2.54 AU from the Sun. With this dust rate we find a loading of 5.9 for water and 4.3 for water plus carbon monoxide. From Table 25, we compute a dust production rate about 2.2 times higher. Similarly, their estimate of $1 \times 10^{16} \text{ g}$ for an orbit-integrated loss of dust is a factor of 3–4 lower than Jewitt & Matthews’ (1999) and ours.

Finally, several investigations determining the mass loading by dust were based on photometry or spectrophotometry of scattered sunlight at optical wavelengths; with no exception, the mass of dust ejecta (and thus the loading) was in these studies underestimated usually by a wide margin. It is well known that millimeter-sized particles dominate the mass distribution, while micron-sized particles the cross-sectional distribution of cometary dust ejecta.¹⁸ Optical observations always sample primarily the smaller grains and fail to adequately account for the larger ones, as remarked by Jewitt & Matthews (1999). This effect manifests itself in the dust production rates reported by Weaver et al. (1997, 1999b) for heliocentric distances exceeding 2.4 AU both before and after perihelion, derived via a proxy parameter Afp (A’Hearn et al. 1995) from their HST and IUE observations.¹⁹ The dust production rates are much too low by about one order of magnitude, even though the computed dust loading of the water flow exceeds unity for all entries in Table I of Weaver et al. (1999b).

¹⁸ This effect is nicely illustrated by McDonnell et al.’s (1991) Figure 13 for the dust ejecta from 1P/Halley detected during the Giotto encounter.

¹⁹ The values of Afp , derived from the spectra of the International Ultraviolet Explorer (IUE), were based of course on scattered sunlight at UV rather than optical wavelengths; one of two Echelle spectrographs worked in a spectral range of up to 3300 Å at most.

Schleicher et al. (1997) reported the dust production data between 25 July 1995 and 15 February 1997 only in terms of $Af\rho$, which they did not convert to the dust production rates. They did, however, point out that the gas production (including OH) was in C/1995 O1 about 20 times higher than in 1P/Halley, while the dust production was more than 100-fold greater at comparable heliocentric distances. Since the best estimate of the dust production rate of 1P is $5 \times 10^7 \text{ g s}^{-1}$ (McDonnell et al. 1991) at the encounter time of the Giotto spacecraft (0.90 AU from the Sun post-perihelion), one should expect a rate of at least $4 \times 10^9 \text{ g s}^{-1}$ for C/1995 O1 at 1 AU from the Sun after perihelion, which is by more than 2σ higher than predicted by the model in Table 25 — still a fair agreement, especially considering that this comparison involves a premise of comparable perihelion asymmetry for the two objects. However, when one employs a conversion factor between $Af\rho$ and the dust production rate recommended by A'Hearn et al. (1995), one obtains $\sim 0.9\text{--}1.0 \times 10^9 \text{ g s}^{-1}$ at 1 AU before perihelion, a factor of ~ 2.5 lower than from Table 25. The source of this discrepancy is again the fact that $Af\rho$ systematically underrates the dust production; the data that Schleicher et al. (1999) referred to for 1P are represented by $Af\rho = 10^{3.9} \text{ cm}$ at 1 AU preperihelion (A'Hearn et al. 1995) and therefore by a dust rate of only $8 \times 10^6 \text{ g s}^{-1}$. On the one hand, this rate indeed is more than 100 times lower than the rate for C/1995 O1, but on the other hand it is also more than 6 times lower than McDonnell et al.'s (1991) post-perihelion rate for 1P normalized to 1 AU from the Sun. The lesson appears to be that comparison of two comets in terms of $Af\rho$ provides a correct dust production rate for the comet of interest, if a correct dust production rate is available for the other comet.

Monitoring the dust distribution between 4.6 AU and 2.9 AU before perihelion in a red passband, Rauer et al. (1997) derived production rates much too low by a factor of 2 to 4 relative to the curve in Figure 15; their values of the dust loading of the flow consisting of water and carbon monoxide, 2.3 through 6.0, then become 9 through 13, in good agreement with the numbers in Table 26.

A more extensive investigation by Weiler et al. (2003), covering a range of heliocentric distances from 4.6 AU to 2.9 AU preperihelion (using in part the observations examined by Rauer et al. 1997) and from 2.8 AU to 12.8 AU post-perihelion, also began by determining $Af\rho$, which was converted to a dust production rate on certain assumptions concerning the dimensions and activity of the nucleus and regarding the size distribution, terminal velocity, bulk density, geometric albedo, and phase function of dust particles. The fit was relatively insensitive to variations in some of the tested parameters and parameteric functions with an exception of the active fraction of the surface: 19% of a nucleus 30 km in radius provided the best match; this indicated an active area of about 2150 km^2 . Unfortunately, Weiler et al.'s resulting dust production rates within 4.6 AU of the Sun were up to almost a factor of 10 lower than the rates by Grün et al. (2001) or those implied by the curve in Figure 15. At 7 AU post-perihelion, Weiler et al.'s dust rate was close to $1 \times 10^6 \text{ g s}^{-1}$, again at least one order of magnitude lower than needed to satisfy Sekanina's (1996) dust-loading condition at ~ 6.7 AU preperihelion. And at 12.8 AU post-perihelion, their dust rate of $\sim 2 \times 10^5 \text{ g s}^{-1}$

was a factor of 2–3 lower than Fulle et al.'s (1998) dust rate at 13 AU preperihelion. Weiler et al.'s major result of a nearly constant dust loading of $\Psi_{\text{H}_2\text{O}+\text{CO}} \simeq 1.1 \pm 0.3$, was lower than the dust loading derived in other studies, a problem admitted by the authors. But a discrepancy of even one order of magnitude in the dust loading could not account for Weiler et al.'s conclusion that merely $1.1 \times 10^{11} \text{ g}$ of dust was lost by the comet over its orbit about the Sun, an amount of mass that was by more than five orders of magnitude (sic!) lower than our, Jewitt & Matthews' (1999), and Lisse et al.'s (1999) estimates.

To summarize, we are convinced that only investigations based on thermal flux observations at wavelengths greater than about $100 \mu\text{m}$ and/or on carefully executed dynamical analysis of the dust ejecta provide reliable information on the total losses of dust from C/1995 O1. These results suggest that the comet's production of dust exceeded a rate of 10^9 g s^{-1} near perihelion and that the total loss of dust per orbit was on the order of 10^{16} g . The dust loading of the gas flow was more than a factor of 10 for water (even in the proximity of perihelion) and close to 10 for water plus carbon monoxide. Such a high dust loading is bound to affect downward the dust-particle velocities, an issue that is addressed next.

9.6. Effects of Dust Loading on Terminal Velocities of Microscopic Grains, and Expansion of Dust Halos

A mass loading by dust of the gas flow has a significant effect on the drag acceleration that the gas imparts to the dust particles during their liftoff from the nucleus. The terminal velocity $v_d(s)$ that a particle of radius s attains at the time its motion decouples from the gas flow is a complicated function of the interaction (Probstein 1969), but the relationship between v_d and Ψ_{gas} is simplified and can be written in closed form for a particle of trivial dimensions; for its terminal velocity, $(v_d)_{\text{lim}}$, Probstein provides an expression:

$$(v_d)_{\text{lim}} = \lim_{s \rightarrow 0} v_d(s) = \left(\frac{2T_{\text{gas}}}{1 + \Psi_{\text{gas}}} \right)^{\frac{1}{2}} \left\{ (c_p)_{\text{gas}} \times \left[1 + \frac{1}{2}(\gamma_{\text{gas}} - 1) \mathbf{M}_{\text{gas}}^2 \right] + c_{\text{dust}} \Psi_{\text{gas}} \right\}^{\frac{1}{2}} \quad (44)$$

where T_{gas} , \mathbf{M}_{gas} , $(c_p)_{\text{gas}}$, and γ_{gas} are, respectively, the temperature, the initial Mach number, the specific heat capacity at constant pressure, and the heat capacity ratio (Poisson constant) for the gas that drives the dust away from the nucleus, and c_{dust} is the specific heat capacity of the dust particle. We note that $(v_d)_{\text{lim}}$ is identical with the parameter v_0 from Equation (35); by its substitution into Equation (44), we obtain for a dust loading of the water flow

$$\Psi_{\text{H}_2\text{O}} = \frac{2(c_p)_{\text{H}_2\text{O}} T_{\text{H}_2\text{O}} \left[1 + \frac{1}{2}(\gamma_{\text{H}_2\text{O}} - 1) \mathbf{M}_{\text{H}_2\text{O}}^2 \right] - v_0^2}{v_0^2 - 2c_{\text{dust}} T_{\text{H}_2\text{O}}}. \quad (45)$$

Since $\gamma_{\text{H}_2\text{O}} = 1.33$ and $\mathbf{M}_{\text{H}_2\text{O}} < 1$ for $\Psi_{\text{H}_2\text{O}} > 0$, the second term in the square brackets is much smaller than unity. This equation is solved by computing a first-guess value of $\Psi_{\text{H}_2\text{O}}$ with this term ignored; by finding an initial Mach number from an approximate formula,

$$\mathbf{M}_{\text{H}_2\text{O}} = 1 - \frac{\Psi_{\text{H}_2\text{O}}^{\frac{3}{5}}}{0.65 + \Psi_{\text{H}_2\text{O}}^{\frac{3}{5}}}; \quad (46)$$

and by iterating Equations (45) and (46) until they converge; Equation (46) provides a reasonable approximation to $\mathbf{M}_{\text{H}_2\text{O}}$ for all values of $\Psi_{\text{H}_2\text{O}}$.

Our objective is now to apply Equation (45) to appropriate observations in order to test whether the very high dust loading of the water flow that resulted from comparison of the production rates of water and dust is independently confirmed in this fashion. The best approximation to a particle of trivial dimensions, which — according to Equation (44) — is accelerated to the highest terminal velocity, is obviously provided by the smallest ejected grains. We already remarked that Min et al. (2005) advocated the presence of grains as small as $0.01 \mu\text{m}$ in radius in order to fit the comet's spectral energy distribution. An overabundance in C/1995 O1 of unusually small submicron-sized dust grains — equal to or smaller than $0.1 \mu\text{m}$ in radius, especially near perihelion — was reported by numerous researchers (e.g., Williams et al. 1997, Harker et al. 1999, Lisse et al. 1999, Hayward et al. 2000). These grains, with the highest terminal velocities near 700 m s^{-1} , populating the leading boundaries of a succession of expanding dust halos, were observed extensively over a period of about two months around perihelion, as already noted in Section 9.5. Besides their velocities, application of Equation (45) requires the knowledge of the mineralogical composition of the submicron-sized grains, because the heat capacity c_{dust} is strongly temperature dependent.

The composition of microscopic dust from C/1995 O1 was examined many times with use of a variety of techniques (e.g., Hanner et al. 1999, Wooden et al. 1999, 2000, Hayward et al. 2000, Grün et al. 2001, Harker et al. 2002, Moreno et al. 2003, Min et al. 2005). Below we compare the results of two very different investigations, one by Harker et al. (2002)²⁰ and the other by Hayward et al. (2000); both dealt with the grain populations over the critical time near perihelion. Harker et al. considered five categories of dust: amorphous carbon, amorphous and crystalline olivine, and amorphous and crystalline pyroxene (orthopyroxene). Their synthetic spectral energy distribution over a range from $1 \mu\text{m}$ to $50 \mu\text{m}$, designed to model the comet at 0.93 AU from the Sun (10 days after perihelion), was fairly consistent with the contributions, by mass, of fully 64% of crystalline olivine with a radiative equilibrium temperature of 220 K ; 9% of crystalline orthopyroxene with a temperature of 320 K ; 12% of amorphous pyroxene (closest to $\text{Mg}_{0.5}\text{Fe}_{0.5}\text{SiO}_3$) with 435 K (for grains $0.1 \mu\text{m}$ in radius); and even smaller contributions from amorphous olivine and carbon.

Hayward et al. (2000) combined their investigation of the thermophysical properties of the microscopic dust in C/1995 O1 with analysis of particle dynamics and the morphology of the dust halos. They concluded that the thermal emission of the halos arose from submicron-sized particles subjected to radiation pressure accelerations smaller than the Sun's gravitational acceleration, which explains a fairly uniform spacing of the halos, controlled by a constant ejection velocity of the dust that populated their leading boundaries. These relatively low accelerations are consistent with silicate, but not carbonaceous, material. Whereas carbon grains accounted largely for

the continuum near $8 \mu\text{m}$ and almost exclusively for the $3\text{--}5 \mu\text{m}$ continuum, silicates dominated the $10 \mu\text{m}$ region of the thermal spectrum. Unlike Harker et al. (2002), Hayward et al. concluded that amorphous pyroxene was the most abundant silicate (at least 40% by mass) and that the pyroxenes contributed almost two-thirds of the silicate grain population. Hayward et al. also pointed out that even though cometary silicates tend to be magnesium rich (whose temperatures are typically below the blackbody temperature), a strong contamination by absorbing material raises their temperature above the blackbody temperature regardless of their intrinsic composition. Hayward et al. determined that the continuum color temperature was elevated in the halos of C/1995 O1; measured from the spectra taken over a period of 1997 March 24–28 it averaged 395 K at 0.92 AU from the Sun, implying a superheat of 1.36.

Even though carbon grains with temperatures in excess of 500 K were present in C/1995 O1, we dismiss their role in populating the leading boundaries of the expanding halos because they were subjected to much higher radiation pressure accelerations (greatly exceeding the Sun's gravitational acceleration) than were silicate grains, thus falling increasingly behind in the course of the halos' expansion. We compute the specific heat capacity c_{dust} for two effective dust-particle temperatures; after normalization to 1 AU from the Sun these are 210 K [corresponding to the dominant particles in Harker et al.'s (2002) model] and 380 K [consistent with Hayward et al.'s (2000) model]. Although radiative equilibrium temperatures do not necessarily vary as $r^{-\frac{1}{2}}$, we will use this power law as an admissible approximation in a narrow range of heliocentric distances near 1 AU .

The variations in the specific heat capacity of solids with the temperature T are known to follow the Debye law at very low T and to converge to a constant at very high T . For our application of Equation (45) it will suffice to approximate $c_{\text{dust}}(T)$ by

$$c_{\text{dust}}(T) = \frac{\xi_0 T^3}{1 + \xi_1 T + \xi_2 T^2 + \xi_3 T^3}, \quad (47)$$

which is readily seen to satisfy either of the two conditions, as $c_{\text{dust}} \simeq \xi_0 T^3$ when $T \rightarrow 0$ and $c_{\text{dust}} \rightarrow \xi_0/\xi_3$ when $T \rightarrow \infty$. The constants ξ_0, \dots, ξ_3 are determined by fitting appropriate data. Combining the Debye law for low temperatures with the Dulong-Petit law for high temperatures, we obtain from Equation (47) an estimate for the Debye temperature, T_D ,

$$T_D = 2\pi \sqrt[3]{\frac{3\pi}{10} \xi_3}. \quad (48)$$

In practice, we employed the heat capacities that were computed by Yomogida & Matsui (1983) for a number of meteorites — as comet-dust analogs — in a temperature range from 100 K to 500 K (at a 50 K step) from their mineral compositions and specific-heat data compiled by Touloukian (1970a, 1970b). The numbers are known to be rather compatible with the more recent results by Consolmagno et al. (2013). To streamline the cubic fit, the averaged expressions of T^3/c_{dust} for the nine standard temperatures between 100 K and 500 K were linked with a synthetic data point at $T = 20 \text{ K}$ that was varied until a condition was satisfied that required, in

²⁰ Harker et al.'s (2002) results were amended in an important erratum that was published two years later; see the reference.

accordance with a Debye-temperature normalized heat-capacity curve, that at T_D the heat capacity reach about 95% of its limiting value, which in the notation of Equation (47) equals ξ_0/ξ_3 . This constraint was equivalent to assigning $c_{\text{dust}}(T) = 0.0085 \text{ J g}^{-1}\text{K}^{-1}$ at $T = 20 \text{ K}$, which resulted in the following formula for a representative heat capacity of the meteorites:

$$c_{\text{dust}}(T) = \frac{2.60 T^3}{1 + 7.03 T + 0.28 T^2 + 2.52 T^3}, \quad (49)$$

where T is expressed in units of 100 K and $c_{\text{dust}}(T)$ comes out in $\text{J g}^{-1}\text{K}^{-1}$. For the Debye temperature this relation offers $T_D = 838 \text{ K}$ and $c_{\text{dust}}(T_D) = 0.98 \text{ J g}^{-1}\text{K}^{-1}$, while $(c_{\text{dust}})_{\text{lim}} = \lim_{T \rightarrow \infty} c_{\text{dust}}(T) = 1.03 \text{ J g}^{-1}\text{K}^{-1}$, so that, indeed, $c_{\text{dust}}(T_D)/(c_{\text{dust}})_{\text{lim}} = 0.95$. For olivine and pyroxene the Dulong-Petit law indicates that $(c_{\text{dust}})_{\text{lim}}$ equals, respectively, 1.01 and $1.07 \text{ J g}^{-1}\text{K}^{-1}$, in good agreement with the result from Equation (49), thus suggesting that in terms of the specific heat capacity the meteorites are acceptable analogs for the dust in C/1995 O1. For the critical temperatures between 210 K and 380 K at 1 AU from the Sun, c_{dust} varies from 0.60 to $0.84 \text{ J g}^{-1}\text{K}^{-1}$, in a range that we employ below in the applications of Equation (45).

The two quantities for water vapor in Equation (45) that still need to be addressed are its temperature, $T_{\text{H}_2\text{O}}$, and specific heat capacity at constant pressure, $(c_p)_{\text{H}_2\text{O}}$. The temperature of water vapor is lower than the temperature of water ice on the nucleus, T_{ice} , from which it sublimates. The relationship between the two is a function of the initial Mach number, $\mathbf{M}_{\text{H}_2\text{O}}$, and the heat capacity ratio, $\gamma_{\text{H}_2\text{O}}$; the gas dynamics approach provides the following expression (e.g., Cercignani 1981):

$$\begin{aligned} T_{\text{H}_2\text{O}} &= T_{\text{ice}} \left[1 + (\pi + 1)\Omega^2 - 2\pi^{\frac{1}{2}}\Omega(1 + \Omega^2)^{\frac{1}{2}} \right] \\ &= T_{\text{ice}} \left[(1 + \Omega^2)^{\frac{1}{2}} - \pi^{\frac{1}{2}}\Omega \right]^2 \\ &\simeq T_{\text{ice}} \left(1 - 2\pi^{\frac{1}{2}}\Omega \right) \quad \text{for } \Omega \ll 1, \end{aligned} \quad (50)$$

where

$$\Omega = \mathbf{M}_{\text{H}_2\text{O}} \frac{\gamma_{\text{H}_2\text{O}} - 1}{\gamma_{\text{H}_2\text{O}} + 1} \left(\frac{\gamma_{\text{H}_2\text{O}}}{8} \right)^{\frac{1}{2}} = 0.058 \mathbf{M}_{\text{H}_2\text{O}}. \quad (51)$$

Since in the presence of dust $\mathbf{M}_{\text{H}_2\text{O}} < 1$, Ω is much smaller than unity, making the approximation in the last line of Equation (50) reasonably accurate.

The temperature of water ice was, as a function of heliocentric distance, determined by solving the energy balance on the comet's nucleus, using the isothermal model (Section 4). Within a few tenths of AU of a unit heliocentric distance, it can be approximated with high accuracy (to better than $\pm 0.1 \text{ K}$) by an interpolation formula

$$T_{\text{ice}} = 194.7 - 16.2(r - 1) + 5.64(r - 1)^2, \quad (52)$$

where r is in AU. At heliocentric distances 0.9 AU to 1.1 AU the temperature of ice varies only by 3.2 K; even the extreme temperature at the subsolar point is merely $\sim 10 \text{ K}$ higher.

The specific heat capacity of water vapor at constant pressure, $(c_p)_{\text{H}_2\text{O}}$, is nearly independent of temperature between at least 50 K and 250 K; to two decimal places,

Table 27

Upper Limit to Mass Loading by Dust of Water Vapor Flow in C/1995 O1 from Halo Expansion Rates

Date 1997 (UT)	Distance from Sun, r (AU)	Halo Expansion Velocity, v_{exp} (km s^{-1})	Upper Limit to Dust Loading of Water Vapor Flow ^a , $\Psi_{\text{H}_2\text{O}}$	
			$T = 210 r^{-\frac{1}{2}}$	$T = 380 r^{-\frac{1}{2}}$
Feb. 27	1.10	0.718	0.57	0.83
Mar. 12	0.98	0.660	1.3	2.3
13	0.97	0.623	2.0	5.2
23	0.93	0.686	1.0	1.6
24	0.93	0.775	0.25	0.33
28	0.92	0.691	0.91	1.5
Apr. 2	0.91	0.660	1.3	2.5
8	0.92	0.628	2.0	5.0
15	0.95	0.610	2.4	8.3
19	0.97	0.664	1.2	2.2
21	0.98	0.610	2.3	7.7
22	0.99	0.743	0.43	0.59
27	1.02	0.603	2.5	9.1
Average	0.97	0.667	1.2	2.1
Va&Ch ^b	0.93	0.667	1.2	2.2

Notes.

^a The first of the two columns refers to the dominant population of crystalline olivine grains in Harker et al.'s (2002) model, the second column to the dominant population of amorphous pyroxene grains in Hayward et al.'s (2000) model.

^b Based on a value of v_0 determined by Vasundhara & Chakraborty (1999) from analysis of an April 10 image, thus providing true loading rate (not an upper limit); estimated error of v_0 is $\pm 0.044 \text{ km s}^{-1}$.

it is approximated by $1.85 \text{ J g}^{-1}\text{K}^{-1}$ in this entire range (Freedman & Haar 1954, Wagner & Pruss 2002, Murphy & Koop 2005).

We are now ready to calculate the mass loading by dust of the water flow near perihelion to check whether the high loading rates, exceeding 10, established from comparison of the production rates in Table 26, are corroborated. As mentioned in Section 9.5, Braunstein et al. (1999) systematically investigated the expansion rate of the concentric dust halos of C/1995 O1 on 13 days between 25 February 1977 (33 days before perihelion) and 27 April 1997 (26 days after perihelion). Derived from the spacing of the leading boundaries of successive halos and an accurately determined rotation period, the expansion velocity was an average of the terminal velocities of the smallest ejected grains, whose radii were estimated at $0.1 \mu\text{m}$ at the most. As such, this halo expansion velocity, v_{exp} , should be by at least several tens of meters per second lower than the limiting velocity v_0 . Nonetheless, substitution of the halo expansion velocity v_{exp} for the limiting velocity v_0 in Equation (45) still is a very good approximation that should provide us with a fairly tight *upper* limit on the mass loading by dust of the water vapor flow near perihelion of C/1995 O1.²¹

Surprisingly, Table 27 demonstrates that when applied to Braunstein et al.'s (1999) halo expansion velocities, Probstein's (1969) model provides us with the dust load-

²¹ The effect of projection onto the plane of the sky could have slightly been overcompensated by Braunstein et al. (1999) in some cases in which the halos emanated from sources that were rather far from the subsolar latitude; still, the deprojected velocities are a much better measure of v_0 than the uncorrected velocities.

ing rates $\Psi_{\text{H}_2\text{O}}$ that are, on the average, at least one order of magnitude lower than are the expected numbers (Table 26). A dust loading of ~ 11 would require at 1 AU from the Sun that the expansion velocities be lower than 0.53 km s^{-1} for the dust temperature of 210 K and lower than 0.60 km s^{-1} for 380 K. This effect could not possibly be caused by systematic errors in Braunstein et al.'s (1999) expansion-velocity measurements, because a similar result was independently obtained by Vasundhara & Chakraborty's (1999), who investigated the dynamics of the dust features. Unfortunately, the April 10 image was the only image that Vasundhara & Chakraborty analyzed from the period of time between late February and late April of 1997, when the straightforwardly interpretable concentric halos were observed (Braunstein et al. 1999). The result by Vasundhara & Chakraborty is listed in Table 27 for comparison; in this case the projection issue was mute, because one of their parameters was directly related to the tabulated value of v_0 . Of interest is the statement by these authors that a *lower* limit on the dust loading of the *gas* flow was equal to 3.4 ± 1.0 . Given that water was only part of the gas mix, this result contradicts a dust loading of the water flow of $<1.2\text{--}2.2$, but not of ~ 11 . Indeed, a nominal *lower* limit on the sublimation rate that Vasundhara & Chakraborty (1999) offer for the April 10 image is $2.6 \times 10^{-5} \text{ g cm}^{-2} \text{ s}^{-1}$, while an *average* sublimation rate of water ice at the same heliocentric distance is, according to the isothermal model, $1.1 \times 10^{-5} \text{ g cm}^{-2} \text{ s}^{-1}$, or 0.4 the nominal lower limit. Unfortunately, the derived sublimation rate is burdened by a very high error, so that this sublimation-rate (but not the dust-loading) argument is rather weak. The net result of this discussion is that the **sublimation of water ice alone could not explain the high expansion velocities** of the prominent dust halos and that **outgassing by other parent molecules should have contributed to the effect**. This conclusion is reminiscent of, and supports, the conclusion we made in Section 9.4 that water ice did not account for more than $\frac{5}{9}$ the total mass outgassed from C/1995 O1 and may have — in an extreme case — accounted for as little as $\frac{1}{5}$.

We are now in a position to infer, in general terms, possible properties of the **missing parent molecules**; we search for a type of volatiles, each of which is, on the one hand, very highly loaded with dust, $\Psi_{\text{gas}} \rightarrow \infty$, yet, on the other hand, can — near 1 AU from the Sun — accelerate submicron-sized silicate grains to terminal velocities of nearly 0.7 km s^{-1} . Returning to Equation (44), we find a limit for infinitely high dust loading,

$$\lim_{\Psi_{\text{gas}} \rightarrow \infty} (v_d)_{\text{lim}} = v_0 = (2 c_{\text{dust}} T_{\text{gas}})^{\frac{1}{2}}. \quad (53)$$

This is a condition for the *temperature of a heavily loaded gas* as a function of the velocity and specific heat capacity of the smallest (silicate) grains in the expanding halos, which implicitly involves the dust-particle temperature. However, the gas temperature is essentially identical with the temperature of the sublimating solid (i.e., a nonwater ice), $T_{\text{gas}} \rightarrow T_{\text{solid}}$ because for a very high mass loading by dust the initial Mach number of the gas flow approaches zero ($\mathbf{M}_{\text{gas}} \rightarrow 0$) and $\Omega \rightarrow 0$ from Equations (51) and (50), so that

$$T_{\text{solid}} = \frac{v_0^2}{2 c_{\text{dust}}}. \quad (54)$$

Next we find a solution to Equation (54) for a heliocentric distance of Hayward et al.'s (2000) thermal infrared spectra, $r = 0.92 \text{ AU}$. From Equation (49) it follows that the specific heat capacity $c_{\text{dust}} = 0.62 \text{ J g}^{-1} \text{ K}^{-1}$ for the crystalline olivine grains that Harker et al. (2002) advocated ($T = 220 \text{ K}$), but $c_{\text{dust}} = 0.85 \text{ J g}^{-1} \text{ K}^{-1}$ for the amorphous pyroxene grains preferred by Hayward et al. ($T = 395 \text{ K}$). With $v_0 = 0.667 \text{ km s}^{-1}$ Equation (54) gives:

$$T_{\text{solid}} = 359 \text{ K (Harker) or } 262 \text{ K (Hayward)}. \quad (55)$$

The relatively cool grains of Harker et al. can be ruled out, because no ice can have a temperature of $\sim 360 \text{ K}$ on the surface of a comet at a heliocentric distance of 0.92 AU, at which the blackbody temperature is 290 K. However, the hot grains suggested by Hayward et al. do fit the proposed hypothesis, which thus implies that **low-volatility ices that sublimate just below the blackbody temperature could upon release accelerate hot grains to terminal velocities near 0.70 km s^{-1}** . This conclusion is not meant to contest the participation of water in the process of dust ejection, but to emphasize that the low-volatility ices (owing to their higher temperature upon sublimation) are critical for imparting the grains their high velocities, otherwise unattainable. Still hotter grains, up to 440 K (e.g., Hanner et al. 1999), imply even lower T_{solid} , down to 253 K. And since Ψ_{gas} , though high, is finite, these values of T_{solid} tend to be upper limits.

In an effort to further learn about these low-volatility ices, in Figure 16 we present a plot of sublimation temperatures, T_{sub} , at a heliocentric distance of 0.92 AU for

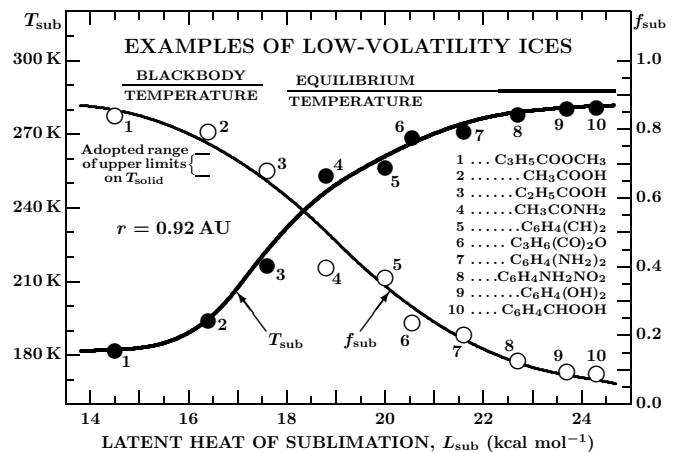


Figure 16. Sublimation temperature, T_{sub} (solid circles), and a fraction of the impinging solar radiation that is spent on sublimation, f_{sub} (open circles), for ten organic low-volatility ices at a heliocentric distance of 0.92 AU. In the order of increasing heat of sublimation, L_{sub} , they are: methyl methacrylate (1), acetic acid (2), propanoic acid (3), acetamide (4), pyrocatechol (5), glutaric anhydride (6), m-phenylenediamine (7), nitranilin or 3-nitroaniline (8), hydroquinone (9), and parahydroxybenzaldehyde (10). The blackbody temperature at this distance from the Sun is 290 K, while the equilibrium temperature of a nonsublimating body with a Bond albedo of 4% and a unit emissivity is 287 K, a limit that no ice at that albedo and emissivity can exceed. Seven of the species have T_{sub} near or exceeding the critical temperature T_{solid} . The correlation between the sublimation heat and sublimation temperature is high, with scatter not exceeding a few K at most. In the displayed range of the heat of sublimation (14,000–25,000 cal mol⁻¹), the fraction of the solar energy that is spent on the sublimation (as opposed on the thermal reradiation) spans about one order of magnitude. A range of upper limits on the ice temperature T_{solid} that supports a dust-grain velocity of 0.667 km s^{-1} is also depicted.

Table 28

Sublimation Rate of and Drag on Dust Grains by Low-Volatility Ices Near Perihelion of C/1995 O1 (Two Grain Temperatures Assumed)

Low-Volatility Organic Molecule	Formula	Molar Mass (g mol ⁻¹)	Latent Heat of Sublimation (cal mol ⁻¹)	Sublimation Rate Per Unit Area (Water = 1)		Grains Accelerated to Velocity v_0 (km s ⁻¹) Near Perihelion	
				by number	by mass	$T_{\text{gr}} = 395$ K	$T_{\text{gr}} = 440$ K
Acetamide	CH ₃ CONH ₂	59.07	18 800	0.309	1.01	0.656	0.667
Pyrocatechol	C ₆ H ₄ (CH) ₂	110.11	20 000	0.268	1.49	0.660	0.671
Glutaric anhydride	C ₃ H ₆ (CO) ₂ O	114.10	20 550	0.167	1.06	0.676	0.687
m-Phenylenediamine	C ₆ H ₄ (NH ₂) ₂	108.14	21 600	0.141	0.84	0.679	0.690
Nitranilin (3-Nitroaniline)	C ₆ H ₄ NH ₂ NO ₂	138.12	22 700	0.081	0.62	0.687	0.699
Hydroquinone	C ₆ H ₄ (OH) ₂	110.11	23 700	0.058	0.36	0.690	0.702
Parahydroxybenzaldehyde	C ₆ H ₄ CHOH	122.12	24 300	0.053	0.36	0.691	0.703

ten organic molecules whose sublimation heat, L_{sub} , exceeds 14,000 cal mol⁻¹, which is about 20% higher than the sublimation heat of water ice. The molecules were selected out of a very limited pool of organic compounds for which — in addition to L_{sub} — the saturated pressure was available as a function of temperature from the NIST webbook (see footnote 10) in terms of the three constants of the Antoine equation, even though sometimes not, unfortunately, covering the needed temperature range, thus requiring an extrapolation. Figure 16 shows a high degree of correlation between the two quantities. Of particular interest are the critical values of T_{sub} and the corresponding values of L_{sub} that are close to and higher than T_{solid} . For our suggested range of $253 \text{ K} \leq T_{\text{solid}} \leq 262 \text{ K}$ one finds that $T_{\text{sub}} = T_{\text{solid}}$ for the ices with a sublimation heat between about 19 000 and 20 000 cal mol⁻¹. All ices with a higher sublimation heat accelerate minuscule dust particles to terminal velocities that are higher than 0.667 km s⁻¹, while the ices with only a moderately lower sublimation heat still should support velocities of about this magnitude.

Not all species in the range of Figure 16 should necessarily fit the curve of $T_{\text{sub}}(L_{\text{sub}})$ as closely as do the ten molecules plotted, and the relationship should not be extrapolated to $L_{\text{sub}} < 14 000$ cal mol⁻¹; indeed, water ice has on the given assumptions (isothermal model and the adopted albedo and emissivity) at 0.92 AU a temperature of 196 K and would leave an offset of more than 15 K from the curve. In fact, the sublimation temperature of water is a bit higher than those of the two most volatile molecules plotted in Figure 16.

At the other end of the sublimation-heat range, the curve can confidently be extrapolated (with an error of a few K), because of the blackbody temperature limit. A stronger constraint is provided by the equilibrium temperature of a nonsublimating body, if the albedo is higher than the emissivity drop from unity. For 0.92 AU from the Sun, the equilibrium temperature of our isothermal object is 287 K. The temperature of the least volatile ice among the ten is only 6 K below this limit.

Also plotted in Figure 16 are the variations with L_{sub} in the fraction of the incident solar radiation that is being spent on the ice's sublimation, f_{sub} . When $f_{\text{sub}} \rightarrow 0$, the solar energy is spent in its entirety of reradiation (heat transport beneath the nucleus' surface being neglected), the surface temperature of the ice varies as an inverse square root of heliocentric distance, and the sublimation rate varies exponentially. When $f_{\text{sub}} \rightarrow 1$, the

Sun's radiation is spent entirely on sublimation, the surface temperature is nearly constant, and the sublimation rate varies as an inverse square of heliocentric distance. The first three most volatile species in Figure 16 use at 0.92 AU a greater fraction of the energy on sublimation, whereas the opposite is the case with the seven least volatile molecules. The fraction f_{sub} spans about one order of magnitude between the most and the least volatile ices in the figure and the sublimation and reradiation break even for a sublimation heat of $\sim 18 800$ cal mol⁻¹, when $f_{\text{sub}} = \frac{1}{2}$.

Sublimation temperatures close to or above the critical temperature T_{solid} that are necessary to accelerate the hot submicron-sized silicate grains to terminal velocities near 0.7 km s⁻¹ are reached by only seven among the molecules plotted in Figure 16, one of them marginally. These are merely examples among a sheer number of existing organic compounds, for most of which needed data are unavailable. Listed in Table 28, these seven molecules illustrate what types of species, whose existence was implied in Section 9.4, are believed to have amply contributed to the activity of C/1995 O1. They are, first of all, **low-volatility ices, with a minimum sublimation heat near 19 000 cal mol⁻¹**; in addition, they are mostly **very heavy molecules**, several times heavier than water, with the molar mass typically exceeding 100; as a corollary, **their sublimation rates per unit surface area are, by mass, comparable to that of water ice**, even though they are much lower in terms of number of molecules because of their lower volatility. Given the large number of more simple organic compounds already detected in C/1995 O1, **their enormous overall number and variety make their summary major contribution to activity compelling**, whereas a **sublimation heat from 19 000 to 25 000 cal mol⁻¹** for many of them makes, near 1 AU from the Sun, this population of organic compounds to be both **sufficiently volatile to outgas vigorously** and to **sublimate at temperatures high enough to accelerate hot submicron-sized grains of dust to high terminal velocities** to explain observational evidence that is inconsistent with water ice-based activity. While many may never be detected individually, we propose that, in their sum, these ices are the **molecular compounds that were responsible for the incompleteness of the integrated mass-loss distribution** in Section 9.4 (Figure 14).

Large organic molecules whose sublimation heat exceeds $\sim 25 000$ cal mol⁻¹ sublimate too insignificantly at heliocentric distances near 1 AU, with their role becom-

ing progressively marginalized. We do not attend to this category of material, although it becomes increasingly important for comets with perihelion distances $\ll 1$ AU.

Even though none of the seven molecules in Table 28 has been detected in C/1995 O1 (or any other comet), one molecule — ethylene glycol, with a sublimation heat estimated at ~ 18200 cal mol $^{-1}$, near the lower boundary of the category of organic ices that is proposed to drive hot microscopic dust into the atmosphere — is known (Crovisier et al. 2004a), as already pointed out.

10. RAMIFICATIONS, AND FUTURE WORK

The proposed population of heavy organic molecules of low volatility has implications for the dynamical behavior of the nucleus of C/1995 O1. Although individually the abundances of these compounds represent only a minor fraction of the water abundance, their sheer number and a variety of their composition may make them to summarily contribute a mass of gas that is comparable to — if not greater than — the mass of water vapor. Accordingly, the heavy organic low-volatility ices could upon their release add substantially to the total momentum that the nucleus is exposed to while revolving about the Sun and thus augment the nongravitational effect that is measured as part of the orbit determination.

Part II of this investigation will focus on the issues related to the nucleus of C/1995 O1. Because of an enormous size of the nucleus (see Szabó et al. 2011, 2012 for updates), the sublimation-driven nongravitational effects were expected to be trivial and their eventual incorporation into the equations of motion was accompanied by much reluctance (e.g., Marsden 1999). Nonetheless, their introduction turned out to be essential to improving the orbital solution; although our preferred Weight System II (Table 10) offers a total nongravitational acceleration of $A = \sqrt{A_1^2 + A_2^2 + A_3^2} = (0.707 \pm 0.039) \times 10^{-8}$ AU day $^{-2}$ at 1 AU from the Sun, only $\sim \frac{2}{3}$ the acceleration derived by Marsden (1999) and $\frac{1}{2}$ that determined by Szutowicz et al. (2002) and by Królikowska (2004) from much shorter orbital arcs, the effect on the orbital velocity integrated over one revolution about the Sun still reaches as much as 2.46 ± 0.14 m s $^{-1}$. In fact, Sosa & Fernández (2011) pointed out that while they employed the nongravitational effects to successfully predict masses and dimensions for a number of long-period comets, the application to C/1995 O1 failed utterly, an exception they admitted was a puzzle: the predicted diameter of the nucleus was a factor of seven much too small and the fraction of the surface that was active came out to be more than seven times the predicted surface area! Given that the nongravitational acceleration is unquestionably genuine and well determined, the *qualitative* explanation offered by Sosa & Fernández is the comet's *extreme hyperactivity* and, parenthetically, a smaller nucleus. If so, its enormous cross-sectional area of 4300 km 2 (Szabó et al. 2011, 2012) is still unexplained. The nature of the orbital motion of C/1995 O1 thus remains an enigma to this day.

With all available evidence to be scrutinized in Part II, there appears to be no escape from a conclusion that the nucleus was an unresolved and rather compact cluster of fragments (some possibly still in contact) with dimensions of up to at least 10 km, the detected nongravitational acceleration being that imparted to the most massive object. Even though the nongravitational accelera-

tions on the active fragments that were less massive were accordingly higher, they triggered perturbations relative to the central mass that remained undetected.

11. CONCLUSIONS

The prime conclusions from this first part of a comprehensive investigation of C/1995 O1 are as follows:

(1) With thousands of astrometric observations covering an orbital arc of 17.6 yr, C/1995 O1 offered us an opportunity to derive a set of orbital elements of exceptionally high quality. As a result of an extensive examination of the data and in-depth dynamical analysis, we present two nominal nongravitational sets of orbital elements, which are distinguished from each other by different systems of weighting the critical observations at both ends of the orbital arc. The superior solution, based on Weight System II (the single pre-discovery position of weight 20, the last three positions of weight 15 each), fits 1950 observations from 1993–2010 with an rms of $\pm 0''.64$; 1631 observations with a residual exceeding $1''.5$ in either coordinate were eliminated in the process of orbit improvement.

(2) Our orbit-determination method fully accommodates Marsden's (1999) proposal that the comet underwent a preperihelion close encounter with Jupiter in the previous return to the Sun, in the 23rd century BCE, and that it was then captured from an Oort-Cloud-type orbit. Although we establish unequivocally that the encounter and capture occurred in -2251 , three Jovian revolutions earlier than originally determined by Marsden (1999), we find his proposal entirely plausible, legitimate, and very compelling. The perijove distance equaled 10.73 Jupiter's equatorial radii ($= 767100$ km $= 0.005128$ AU).

(3) The nongravitational parameters of the solution based on Weight System II imply that an orbit-integrated sublimation-driven effect on the comet's orbital velocity amounted to 2.46 m s $^{-1}$, with the radial component positive and dominant, the normal component negative and equal to about $\frac{3}{4}$ the radial component, and the transverse component two orders of magnitude smaller and poorly determined. The scaling distance of the modified nongravitational law applied equals 15.4 AU, ~ 5.5 times the scaling distance for water ice.

(4) We computed the ephemeris for the comet's return to perihelion in -2250 and found it to have been a fairly favorable apparition for the northern-hemisphere observer, with a peak apparent brightness estimated at -2 . We painstakingly searched for a historical record that might refer to C/1995 O1, but the time-frame uncertainties in the 23rd century BCE prevented us from making any definite identification.

(5) The orbital motion of C/1995 O1 was extrapolated forward in time, with a prediction for the next return to perihelion in the year 4393 and afterwards in 5451. It is noted not only that the actual orbital period is getting shorter with time, from 4246 yr between the years -2250 and 1997, to 2396 yr between the years 1997 and 4393, and to 1058 yr between the years 4393 and 5451; but that the comet's orbital evolution is and will for some time be driven by orbital-cascade resonance with Jupiter, from 1:358 to 1:202 and then to approximately 1:89. We studied this dynamical process recently in connection with a pair of long-period comets and singled it out as momentous for a rapid inward drifting of aphelia of comets in nearly-parabolic orbits (Sekanina & Kracht 2016).

(6) Voluminous data on the production rates of water and other parent molecules sublimating from the nucleus of C/1995 O1 over a wide range of heliocentric distances as well as data on the brightness (as a proxy) at very large distances from the Sun allowed us to show that the variations in activity were expressible by the same type of law as the nongravitational acceleration in the comet's orbital motion, but with different values of the scaling distance that is a function of the latent heat of sublimation.

(7) The comet's activity was asymmetric relative to perihelion, especially at very large heliocentric distances. The carbon-monoxide-driven activity is described by a scaling distance of 12 AU before perihelion, but 20 AU after perihelion. The scaling distance of the orbital solution with Weight System II is almost exactly halfway between the two. The ways of incorporating the perihelion asymmetry into the nongravitational law are addressed.

(8) Employing appropriate scaling distances that fit the gas-abundance observations, the total mass lost per orbit of C/1995 O1 was determined for three parent molecules, equaling 3.4×10^{15} g for water, 1.1×10^{15} g for carbon monoxide, and 0.8×10^{15} g for carbon dioxide. In their sum, they are equivalent to the mass of a sphere 1.7 km in diameter at a density of 0.4 g cm^{-3} , with water accounting for less than $\frac{2}{3}$ of the total mass.

(9) Outgassing by a number of additional, mostly organic, parent molecules identified in C/1995 O1 (as compiled by Bockelée-Morvan et al. 2004) was examined in the same fashion. For each of 18 trace compounds, the mass lost per orbit was computed from the nongravitational law with a scaling distance determined from the latent heat of sublimation, and their sum found to add another $\sim 0.7 \times 10^{15}$ g to the total production of gas; the trace molecules searched for but not detected were not counted. Because of their high molar mass, the organic molecules contribute disproportionately more masswise, compared to their abundances. Their mass brings the total mass lost per orbit by outgassing to 6×10^{15} g in the least and the share of water to not more than 57%.

(10) On account of a sheer number and variety of compounds into which the elements C, H, O, N, S (possibly others) could combine, and because of a large tally of as yet unidentified bands in the spectrum, particularly in the near-infrared, submillimeter, and microwave regions, one can expect the presence in the nucleus of numerous additional, mostly organic, ices currently unknown. We first examined the number of observed species as a function of their orbit-integrated mass loss relative to water. The data for C/1995 O1 (by far the most extensive for any comet) suggested that the cumulative number of species followed a power law of the normalized mass loss per orbit with a slope near -0.7 and that, indeed, this sample appeared to be substantially incomplete, by a factor of up to five for the molecules whose total mass loss per orbit was $\geq 1\%$ of the mass loss of water ice, by a factor of up to 19 for the molecules whose total mass loss was $\geq 0.1\%$ of that of water ice, and by a factor of as much as 100 for the molecules whose total mass loss was $\geq 0.01\%$ of that of water ice. One could expect that in C/1995 O1 the number of parent molecules of the last category may be as high as several hundred. For comparison, the number of molecular compounds detected in interstellar and/or circumstellar space is about 200.

(11) The described exercise also allows one to estimate the comet's total mass loss per orbit by outgassing by summing up the contributions from all species. Because of fairly large uncertainties involved, it is possible to provide only probable limits, which are about 2 to 5 times the mass loss of water per orbit, with the upper limit representing merely an educated guess.

(12) To check a maximum possible number of compounds produced under certain constraints, we developed a simple mathematical model for generating molecular formulas by combining specific elements with an arbitrary but limited number of atoms per element. We ascertained that a mathematically complete set of compounds consisting of up to six atoms of carbon and hydrogen, up to two to three atoms of oxygen, and up to one atom of nitrogen and sulfur — mimicking the limits for most compounds detected in the interstellar and/or circumstellar medium — numbered 570–770 molecules (not counting isomers but including formulas that refer to no genuine chemicals), on the same order of magnitude as the number of parent molecules derived from the outgassing mass-loss distribution of species.

(13) Examining the production rates of dust, based on submillimeter and microwave observations, we found that they too can be fitted by the same type of law as the nongravitational acceleration in the comet's orbital motion. Establishing that the comet's production of dust integrated over the orbit about the Sun amounted to some 4.0×10^{16} g (in fair agreement with the estimate by Jewitt & Matthews 1999) and comparing it with the orbit-integrated production of parent molecules, we concluded that the mass loading by dust of the water flow (the dust-to-water mass-loss ratio) integrated over the orbit about the Sun reached 11.8, while the dust loading of the combined flow of water, carbon monoxide, and carbon dioxide equaled 7.5. The dust loading of the total gas flow from C/1995 O1 may have been as low as 3.

(14) Another piece of evidence for the existence of a large number of parent molecular compounds in the nucleus of C/1995 O1 is provided by the terminal velocities of submicron-sized silicate grains that populated the comet's expanding halos, observed for about two months near perihelion. The halos expanded with velocities close to 0.7 km s^{-1} , which — as implied by a hydrodynamic model — is too high to be accounted for by a drag acceleration exerted by sublimating water molecules, given the extremely high mass loading of the water flow by the dust. Probst's (1969) theory was used to compute an upper limit on the expected mass loading by dust from the observed halo-expansion velocities that was typically one order of magnitude lower than the dust loading derived directly from the production data. This contradiction provides strong evidence that the terminal velocities of submicron-sized silicate particles were supported not only by the expanding flow of water vapor but by additional sublimating matter as well.

(15) Further application of the hydrodynamic model suggests that a likely critical driver of the hot microscopic silicate dust in the halos of C/1995 O1 was a mixture of heavy organic molecules of relatively low volatility (with a range of sublimation heat of $\sim 19\,000\text{--}25\,000 \text{ cal mol}^{-1}$) with sublimation temperatures just below the blackbody temperature at heliocentric distances near 1 AU.

(16) These heavy organic molecules of low volatility appear to be identical with the missing compounds that we found to be responsible for a major incompleteness of the observed distribution of sublimating ices sorted by the relative orbit-integrated mass loss. In Part II we will argue that the presence of these as yet undetected species should also slightly alleviate the problem of the sizable nongravitational effects detected in the orbital motion of C/1995 O1, although the primary source of the disproportion of the momentum transferred to the nucleus by the mass lost by outgassing appears to be the nature of the nucleus as a compact cluster of massive fragments in near-contact with one another, a bold hypothesis — to be addressed in Part II — that, given the strong evidence, is extremely difficult to avoid.

This project, whose orbital part was inspired by the insightful paper written by the late B. G. Marsden in 1998, was initiated by the first author (ZS) years ago in collaboration with P. W. Chodas, whose contribution is hereby acknowledged and greatly appreciated. The orbital results presented in this paper were achieved thanks primarily to the second author (RK). This research was carried out in part at the Jet Propulsion Laboratory, California Institute of Technology, under contract with the National Aeronautics and Space Administration.

APPENDIX A MOST RECENT EFFORTS TO OBSERVE COMET C/1995 O1

The 2012 attempt by D. Herald to observe this comet (Section 2) was not the only effort of this kind, following the 2010 astrometric observations made with the 220-cm f/8.0 Ritchey-Chrétien telescope at the European Southern Observatory (ESO) (Sárneczky et al. 2011; Szabó et al. 2011). The comet was in fact observed with the 820-cm Antu unit of the ESO's Very Large Telescope (VLT) as a stellar object of an average V magnitude of 24.20 and R magnitude 23.72 on 2011 Oct 5, 23, and 25 (Szabó et al. 2012), but no astrometry is available. Further information is provided in a blog by N. Howes, G. Sostero, and E. Guido,²² who employed remotely the 200-cm f/10.0 Siding Spring-Faulkes South telescope to search for the comet on five occasions between 2012 Sept 25 and Oct 9; it was detected on none of 45 to 75-minute images with a limiting magnitude from 21.5 to 23.5. All these efforts point consistently to a conclusion that the object of magnitude 21.8, exposed by Herald with his 40-cm reflector on 2012 Aug 7, could not be the comet, in agreement with the observer's own final statement.

APPENDIX B SHAPE OF THE CURVE $\mathfrak{S}(X)$ AS FUNCTION OF A COMET'S PERIHELION DISTANCE

While, in general, the $g_{\text{mod}}(r; r_0)$ function is integrated numerically, approximate values of $\mathfrak{S}(X)$ can be found in closed form in the hypotheticalal cases of an infinitely volatile species, when $L_{\text{sub}} \rightarrow 0$ ($r_0 \rightarrow \infty$), and an infinitely refractory species, when $L_{\text{sub}} \rightarrow \infty$ ($r_0 \rightarrow 0$). Expressing the normalization coefficient ψ in terms of r_0 and the

exponents m , n , and k ,

$$g_{\text{mod}}(r; r_0) = r^{-(m+nk)} \left(\frac{r_0^{-n} + 1}{r_0^{-n} + r^{-n}} \right)^k = r^{-m} \left(\frac{r_0^n + 1}{r_0^n + r^n} \right)^k, \quad (56)$$

we find

$$\begin{aligned} \lim_{r_0 \rightarrow \infty} g_{\text{mod}}(r; r_0) &= r^{-m} && \text{for } L_{\text{sub}} \rightarrow 0, \\ \lim_{r_0 \rightarrow 0} g_{\text{mod}}(r; r_0) &= r^{-(m+nk)} && \text{for } L_{\text{sub}} \rightarrow \infty. \end{aligned} \quad (57)$$

Thus, the integral $\mathfrak{S}(L_{\text{sub}})$ from Equation (14) may in either case be written as

$$\begin{aligned} \mathfrak{S} &= \frac{2}{k\sqrt{p}} \int_0^\pi \left(\frac{1+e \cos v}{p} \right)^\zeta dv \\ &= \frac{2^{\zeta+2}}{k} p^{-(\zeta+\frac{1}{2})} \int_0^{\frac{1}{2}\pi} \cos^{2\zeta} u [1 - \Delta e (1 - \frac{1}{2} \sec^2 u)]^\zeta du, \end{aligned} \quad (58)$$

where $u = \frac{1}{2}v$, $\Delta e = 1 - e$ and $\zeta = m - 2$ for $L_{\text{sub}} \rightarrow 0$ and $\zeta = m + nk - 2$ for $L_{\text{sub}} \rightarrow \infty$. For C/1995 O1 as a nearly parabolic comet, $\Delta e \rightarrow 0$ and the term with Δe has the nature of a minor correction to the $\cos^{2\zeta} u$ term. Let us replace the variable u with an appropriate constant value of $\langle u \rangle$, so that $\sec^2 \langle u \rangle = \eta$ and the integration is readily executable. We obtain

$$\begin{aligned} \mathfrak{S} &= \frac{\sqrt{\pi}}{k} 2^{\zeta+1} p^{-(\zeta+\frac{1}{2})} \frac{\Gamma(\zeta+\frac{1}{2})}{\Gamma(\zeta+1)} \left[1 - \zeta (1 - \frac{1}{2}\eta) \Delta e \right. \\ &\quad \left. + \frac{1}{2} \zeta (\zeta - 1) (1 - \frac{1}{2}\eta)^2 (\Delta e)^2 - \dots \right], \end{aligned} \quad (59)$$

where Γ is the Gamma function.

Let us now insert the exponents m , n , and k for ζ and calculate the ratio of the two limiting equivalent times; we obtain

$$\begin{aligned} \frac{\mathfrak{S}_\infty}{\mathfrak{S}_0} &= \frac{\lim_{L_{\text{sub}} \rightarrow \infty} \mathfrak{S}(L_{\text{sub}})}{\lim_{L_{\text{sub}} \rightarrow 0} \mathfrak{S}(L_{\text{sub}})} \\ &= \left(\frac{2}{p} \right)^{nk} \frac{\Gamma(m+nk-\frac{3}{2})}{\Gamma(m+nk-1)} \frac{\Gamma(m-1)}{\Gamma(m-\frac{3}{2})} \\ &\quad \times \left\{ 1 - \left[\frac{1}{2}(m-2)(\eta_0 - \eta_\infty) \right. \right. \\ &\quad \left. \left. + nk(1 - \frac{1}{2}\eta_\infty) \right] \Delta e + \dots \right\}, \end{aligned} \quad (60)$$

where η_0 is the value of η for $L_{\text{sub}} \rightarrow 0$ and η_∞ its value for $L_{\text{sub}} \rightarrow \infty$. By numerical integration we determine that $\mathfrak{S}_0 = 231.07$ days, requiring $\eta_0 = 19.36$ and therefore $\langle u_0 \rangle = 76^\circ.9$. On the other hand, $\mathfrak{S}_\infty = 260.98$ days, so that $\eta_\infty = 1.02$ and $\langle u_\infty \rangle = 8^\circ.0$.

Equation (60) shows that the ratio $\mathfrak{S}_\infty/\mathfrak{S}_0$ is a very steep function of the orbit parameter $p = q(1+e)$, varying as $p^{-23.5}$. For parabolic orbits the Δe correction term disappears and $p = 2q$, so that $\mathfrak{S}_\infty/\mathfrak{S}_0 = 0.138 q^{-23.5}$. This formula implies that $\mathfrak{S}_\infty = \mathfrak{S}_0$ for a parabolic orbit with $q = 0.919$ AU, only very slightly larger than the perihelion distance of C/1995 O1. On the other hand, $\mathfrak{S}_\infty = 10 \mathfrak{S}_0$ for $q = 0.833$ AU and $\mathfrak{S}_\infty = 100 \mathfrak{S}_0$ for $q = 0.756$ AU. Thus the shorter the perihelion distance is, the more dominant becomes the orbit-integrated mass loss of more refractory species in comparison with more volatile species, much more so than their reported production-rate ratio \mathfrak{R}_Q indicates.

²² <http://remanzacco.blogspot.it/2012/10/deep-south.html>.

REFERENCES

- Acree, W., & Chickos, J. S. 2016, *J. Phys. Chem. Ref. Data*, 45, 033101
- A'Hearn, M. F., Millis, R. L., Schleicher, D. G., et al. 1995, *Icarus*, 118, 223
- Azreg-Aïnou, M. 2005, *Monatshefte für Chemie*, 136, 2017; also, 2014, eprint arXiv:1403.4403
- Baldet, F. 1950, *Annuaire pour l'an 1950*, Bureau des Longitudes, B.1
- Baldet, F., & de Obaldia, G. 1952, *Catalogue Général des Orbites de Comètes de l'an -466 à 1952*. (Paris: Centre National de la Recherche Scientifique)
- Biver, N., Bockelée-Morvan, D., Colom, P., et al. 1997, *Science*, 275, 1915
- Biver, N., Bockelée-Morvan, D., Colom, P., et al. 1999, *Earth Moon Plan.*, 78, 5
- Biver, N., Bockelée-Morvan, D., Crovisier, J., et al. 2002, *Earth Moon Plan.*, 90, 5
- Bockelée-Morvan, D., & Rickman, H. 1999, *Earth Moon Plan.*, 79, 55
- Bockelée-Morvan, D., Crovisier, J., Mumma, M. J., & Weaver, H. A. 2004, in *Comets II*, ed. M. C. Festou, H. U. Keller, & H. A. Weaver (Tucson, AZ: University of Arizona), 391
- Braunstein, M., Womack, M., Deglman, F., et al. 1999, *Earth Moon Plan.*, 78, 219
- Breasted, J. H. 1906, *Ancient Records of Egypt (Second Series)*. (Chicago: University of Chicago Press)
- Brueckner, G. E., Howard, R. A., Koomen, M. J., et al. 1995, *Solar Phys.*, 162, 357
- Capria, M. T., Coradini, A., & De Sanctis, M. C. 1997, in *Interactions Between Planets and Small Bodies*, XXIII IAU General Assembly, Joint Disc. 6, 39
- Capria, M. T., Coradini, A., & De Sanctis, M. C. 2002, *Earth Moon Plan.*, 90, 217
- Cercignani, C. 1981, *Progr. Astronaut. Aeronaut.*, 74, 305
- Colom, P., Gérard, E., Crovisier, J., et al. 1999, *Earth Moon Plan.*, 78, 37
- Combi, M. R., Reinard, A. A., Bertaux, J., et al. 2000, *Icarus*, 144, 191
- Consolmagno, G. J., Schaefer, M. W., Schaefer, B. E., et al. 2013, *Plan. Space Sci.*, 87, 146
- Cottin, H., & Fray, N. 2008, *Space Sci. Rev.*, 138, 179
- Crovisier, J. 1999, *Earth Moon Plan.*, 79, 125
- Crovisier, J., Brooke, T. Y., Hanner, M. S., et al. 1996, *A&A*, 315, L385
- Crovisier, J., Leech, K., Bockelée-Morvan, D., et al. 1997, *Science*, 275, 1904
- Crovisier, J., Leech, K., Bockelée-Morvan, D., et al. 1999, in *The Universe As Seen by ISO, ESA-SP 427*, ed. P. Cox & M. F. Kessler (Noordwijk, Netherlands: ESTEC), 137
- Crovisier, J., Bockelée-Morvan, D., Biver, N., et al. 2004a, *A&A*, 418, L35
- Crovisier, J., Bockelée-Morvan, D., Colom, P., et al. 2004b, *A&A*, 418, 1141
- Dello Russo, N., Mumma, M. J., DiSanti, M. A., et al. 2000, *Icarus*, 143, 324
- de Pater, I., Forster, J., Wright, M., et al. 1998, *AJ*, 116, 987
- Despois, D. 1999, *Earth Moon Plan.*, 79, 103
- DiSanti, A., Mumma, M. J., Dello Russo, N., et al. 1999, *Nature*, 399, 662
- Dixon, A. R., Xue, T., & Sanov, A. 2016, *J. Chem. Phys.*, 144, 234305
- Durig, J. R., & Hannum, S. E. 1971, *J. Cryst. Mol. Str.*, 1, 131
- Enzian, A., Cabot, H., & Klinger, J. 1998, *Plan. Space Sci.*, 46, 851
- Fray, N., Bardyn, A., Cottin, H., et al. 2016, *Nature*, 538, 72
- Friedman, A. S., & Haar, L. 1954, *J. Chem. Phys.*, 22, 2051
- Froeschlé, C., & Rickman, H. 1986, *A&A*, 170, 145
- Fulle, M., Cremonese, G., & Böhm, C. 1998, *AJ*, 116, 1470
- Fulle, M., Della Corte, V., Rotundi, A., et al. 2016, *MNRAS*, 462, S132
- Galle, J. G. 1894, *Cometenbahnen*. (Leipzig: Engelmann Verlag)
- George, D. 1995, *IAU Circ.* 6205
- Green, D. W. E. (ed.) 1995, *Int. Comet Q.*, 17, 193
- Green, D. W. E. (ed.) 1996, *Int. Comet Q.*, 18, 24, 58, 130
- Green, D. W. E. (ed.) 1997, *Int. Comet Q.*, 19, 126, 185, 255
- Green, D. W. E. (ed.) 1998, *Int. Comet Q.*, 20, 20, 185
- Green, D. W. E. (ed.) 1999, *Int. Comet Q.*, 21, 122
- Grün, E., Hanner, M. S., Peschke, S. B., et al. 2001, *A&A*, 377, 1098
- Gunnarsson, M., Bockelée-Morvan, D., Winnberg, A., et al. 2003, *A&A*, 402, 383
- Hale, A., & Bopp, T. 1995, *IAU Circ.*, 6187
- Hanner, M. S. 1983, in *Cometary Exploration*, ed. T. I. Gombosi (Budapest: Hungarian Acad. Sci.), vol. 2, 1
- Hanner, M. S. 1984, *Adv. Space Res.*, 4(9), 189
- Hanner, M. S., Gehrz, R. D., Harker, D. E., et al. 1999, *Earth Moon Plan.*, 79, 247
- Harker, D. E., Woodward, C. E., McMurtry, C. W., et al. 1999, *Earth Moon Plan.*, 78, 259
- Harker, D. E., Wooden, D. H., Woodward, C. E., & Lisse, C. M. 2002, *ApJ*, 580, 579 (Erratum: 2004, *ApJ*, 615, 1081)
- Harris, W. M., Scherb, F., Mierkiewicz, E., et al. 2002, *ApJ*, 578, 996
- Hasegawa, I. 1980, *Vistas Astron.*, 24, 59
- Hayward, T. L., Hanner, M. S., & Sekanina, Z. 2000, *ApJ*, 538, 428
- Ho, P. Y. 1962, *Vistas Astron.*, 5, 127
- Hörz, F., Bastien, R., Borg, J., et al. 2006, *Science*, 314, 1716
- Howard, R. A., Moses, J. D., Vourlidis, A., et al. 2008, *SSRv*, 136, 67
- Jewitt, D., & Matthews, H. 1999, *AJ*, 117, 1056
- Jewitt, D., Senay, M., & Matthews, H. 1996, *Science*, 271, 1110
- Kidger, M. R. 1999, *Earth Moon Plan.*, 78, 169
- Kramer, E. A., Fernández, Y. R., Lisse C. M., et al. 2014, *Icarus*, 236, 136
- Królikowska, M. 2004, *A&A*, 427, 1117
- Kronk, G. W. 1999, *Cometography*, Vol. 1: Ancient-1799. (Cambridge, UK: Cambridge University Press)
- Landgraf, W. 1986, *A&A*, 163, 246
- Lasue, J., Levasseur-Regourd, A. C., Hadamcik, E., & Alcouffe, G. 2009, *Icarus*, 199, 129
- Liller, W. 2001, *Int. Comet Q.*, 23, 93
- Lisse, C. M., Fernández, Y. R., A'Hearn, M. F., et al. 1999, *Earth Moon Plan.*, 78, 251
- Liu, C., Liu, X., & Ma, L. 2003, *J. Astron. Hist. Herit.*, 6, 53
- Marcus, J. N. 2007, *Int. Comet Q.*, 29, 39
- Marsden, B. G. 1969, *AJ*, 74, 720
- Marsden, B. G. 1970, *AJ*, 75, 75
- Marsden, B. G. 1995, *IAU Circ.*, 6194
- Marsden, B. G. 1999, *Earth Moon Plan.*, 79, 3
- Marsden, B. G. 2007, *Minor Plan. Circ.*, 61436
- Marsden, B. G., & Williams, G. V. 2008, *Catalogue of Cometary Orbits 2008*, p. 108 (17th ed.; Cambridge, MA: Smithsonian Astrophysical Observatory, 195pp)
- Marsden, B. G., Sekanina, Z., & Yeomans, D. K. 1973, *AJ*, 78, 211
- Marsden, B. G., Sekanina, Z., & Everhart, E. 1978, *AJ*, 83, 64
- McDonnell, J. A. M., Lamy, P. L., & Pankiewicz, G. S. 1991, in *Comets in the Post-Halley Era*, ed. R. L. Newburn, Jr., M. Neugebauer, & J. Rahe (Dordrecht, Netherlands: Kluwer), 1043
- McNaught, R. H. 1995, *IAU Circ.*, 6198
- Min, M., Hovenier, J. W., de Koter, A., et al. 2005, *Icarus*, 179, 158
- Moreno, F., Muñoz, O., Vilaplana, R., & Molina, A. 2003, *ApJ*, 595, 522
- Murphy, D. M., & Koop, T. 2005, *QJRMSS*, 131, 1539
- Pang, K. D., & Yau, K. K. 1996, in *Dynamics, Ephemerides, and Astrometry of the Solar System*, IAU Symp. 172, ed. S. Ferraz-Mello, B. Morando, & J.-E. Arlot (Dordrecht, Netherlands: Kluwer), 113
- Pingré, A. G. 1783, *Cométographie; ou, Traité historique et théorique des comètes*. (Paris: L'Imprimerie Royale)
- Porter, J. G. 1961, *Mem. Brit. Astron. Assoc.*, 39, No. 3
- Prialnik, D. 1997, *ApJ*, 478, L107
- Probstein, R. F. 1969, in *Problems of Hydrodynamics and Continuum Mechanics*, ed. F. Bisshopp & L. I. Sedov (Philadelphia: Soc. Ind. Appl. Math.), 568
- Rauer, H., Arpigny, C., Boehnhardt, H., et al. 1997, *Science*, 275, 1909
- Rickman, H., & Froeschlé, C. 1983, in *Cometary Exploration*, ed. T. I. Gombosi (Budapest: Hungarian Acad. Sci.), vol. 3, 109
- Rickman, H., & Froeschlé, C. 1986, *A&A*, 170, 161
- Sárneczky, K., Szabo, G., & Kiss, L. 2011, *Minor Plan. Circ.*, 74775
- Schleicher, D. G., Lederer, S. M., Millis, R. L., & Farnham, T. L. 1997, *Science*, 275, 1913
- Sekanina, Z. 1988a, *AJ*, 95, 911
- Sekanina, Z. 1988b, *AJ*, 96, 1455
- Sekanina, Z. 1996, *A&A*, 314, 957
- Sekanina, Z., & Farrell, J. A. 1982, *AJ*, 87, 1836
- Sekanina, Z., & Kracht, R. 2014, eprint arXiv:1404.5968
- Sekanina, Z., & Kracht, R. 2015, *ApJ*, 801, 135
- Sekanina, Z., & Kracht, R. 2016, eprint arXiv:1607.3440
- Senay, M., Rownd, B., Lovell, A., et al. 1997, *BAAS*, 29, 1034
- Shaw, I. (ed.) 2000, *The Oxford History of Ancient Egypt*. (Oxford: Oxford University Press)
- Sitariski, G. 1990, *Acta Astron.*, 40, 405

- Sitarski, G. 1994a, *Acta Astron.*, 44, 91
Sitarski, G. 1994b, *Acta Astron.*, 44, 417
Sosa, A., & Fernández, J. A. 2011, *MNRAS*, 416, 767
Stern, S. A., Colwell, W. B., Festou, M. C., et al. 1999, *AJ*, 118, 1120
Stratton, F. J. M. 1928, in *Handbuch der Astrophysik* (vol. 6), ed. G. Eberhard, A. Kohlschütter, & H. Ludendorff (Berlin: Springer), 251
Szabó, Gy. M., Kiss, L. L., & Sárneczky, K. 2008, *ApJ*, 677, 121
Szabó, Gy. M., Sárneczky, K., & Kiss, L. L. 2011, *A&A*, 531, A11
Szabó, Gy. M., Kiss, L. L., Pál, A., et al. 2012, *ApJ*, 761, 8
Szutowicz, S., Królikowska, M., & Sitarski, G. 2002, *Earth Moon Plan.*, 90, 119
Touloukian, Y. S. (ed.) 1970a, *Thermophysical Properties of Matter*. Vol. 4: Specific Heat – Metallic Elements and Alloys. *Thermophys. Prop. Res. Center Data Series*, Purdue Univ. (New York: Plenum Press)
Touloukian, Y. S. (ed.) 1970b, *Thermophysical Properties of Matter*. Vol. 5: Specific Heat – Nonmetallic Solids. *Thermophys. Prop. Res. Center Data Series*, Purdue Univ. (New York: Plenum Press)
Vasundhara, R., & Chakraborty, P. 1999, *Icarus*, 140, 221
Vsekhsvyatsky, S. K. 1958, *Fizicheskie kharakteristiki komet*. (Moscow: Gosud. izd-vo fiz.-mat. lit.); translated: 1964, *Physical Characteristics of Comets*, NASA TT-F-80 (Jerusalem: Israel Program for Scientific Translations)
Wagner, W., & Pruss, A. 2002, *J. Phys. Chem. Ref. Data*, 31, 387
Weaver, H. A., Feldman, P. D., A'Hearn, M. F., et al. 1997, *Science*, 275, 1900
Weaver, H. A., Brooke, T. Y., Chin, G., et al. 1999a, *Earth Moon Plan.*, 78, 71
Weaver, H. A., Feldman, P. D., A'Hearn, M. F., et al. 1999b, *Icarus*, 141, 1
Weiler, M., Rauer, H., Knollenberg, J., et al. 2003, *A&A*, 403, 313
Williams, D. M., Mason, C. G., Gehrz, R. D., et al. 1997, *ApJ*, 489, 91
Williams, G. V. 2011, *Minor Plan. Circ.*, 75007
Williams, J. 1871, *Observations of Comets from B.C. 611 to A.D. 1640*, Extracted from the Chinese Annals. (London: Strange-ways & Walden)
Womack, M., Festou, M. C., & Stern, S. A. 1997, *AJ*, 114, 2789
Wooden, D. H., Harker, D. E., Woodward, C. E., et al. 1999, *ApJ*, 517, 1034
Wooden, D. H., Butner, H. M., Harker, D. E., & Woodward, C. E. 2000, *Icarus*, 143, 126
Wright, I. P., Sheridan, S., Barber, S. J., et al. 2015, *Science*, 349, aab0673
Wu, Q., Zhao, Z., Liu, L., et al. 2016, *Science*, 353, 579
Wylie, L. M. 1958, *The Vapor Pressure of Solid Argon, Carbon Monoxide, Methane, Nitrogen, and Oxygen from Their Triple Points to the Boiling Point of Hydrogen*. Thesis. (Atlanta, GA: Georgia Institute of Technology)
Yeomans, D. K. 1984, in *Cometary Astrometry*, ed. D. K. Yeomans, R. M. West, R. S. Harrington, & B. G. Marsden (Pasadena: Jet Propulsion Laboratory), 167
Yeomans, D. K., & Chodas, P. W. 1989, *AJ*, 98, 1083
Yomogida, K., & Matsui, T. 1983, *J. Geophys. Res.*, 88, 9513